PRODUCTION AND CHARACTERIZATION OF HIERARCHICALLY
POROUS TRANSPARENT GLASSES

A THESIS SUBMITTED TO
THE GRADUATE SCHOOL OF NATURAL AND APPLIED SCIENCES
OF
MIDDLE EAST TECHNICAL UNIVERSITY

BY

EMRE BURAK ERTUŞ

IN PARTIAL FULFILLMENT OF THE REQUIREMENTS
FOR
THE DEGREE OF DOCTOR OF PHILOSOPHY
IN
METALLURGICAL AND MATERIALS ENGINEERING

JANUARY 2020

Approval of the thesis:

PRODUCTION AND CHARACTERIZATION OF HIERARCHICALLY POROUS TRANSPARENT GLASSES

submitted by **EMRE BURAK ERTUŞ** in partial fulfillment of the requirements for the degree of **Doctor of Philosophy** in **Metallurgical and Materials Engineering, Middle East Technical University** by,

Prof. Dr. Halil Kalıpçılar
Dean, Graduate School of **Natural and Applied Sciences**   _____

Prof. Dr. Cemil Hakan Gür
Head of the Department, **Met. and Mat. Eng.**   _____

Prof. Dr. Abdullah Öztürk
Supervisor, **Met. and Mat. Eng., METU**   _____

Assoc. Prof. Dr. Çekdar Vakıf Ahmetoğlu
Co-Supervisor, **Materials Science and Eng.**
İzmir Institute of Technology   _____

Examining Committee Members:

Prof. Dr. Caner Durucan
Met. and Mat. Eng., METU   _____

Prof. Dr. Abdullah Öztürk
Met. and Mat. Eng., METU   _____

Prof. Dr. Hüsnü Emrah Ünalan
Met. and Mat. Eng., METU   _____

Prof. Dr. Jongee Park
Met. and Mat. Eng., Atılım Univ.   _____

Assoc. Prof. Dr. Volkan Kalem
Met. and Mat. Eng., Konya Technical Univ.   _____

Date: 30.01.2020

I hereby declare that all information in this document has been obtained and presented in accordance with academic rules and ethical conduct. I also declare that, as required by these rules and conduct, I have fully cited and referenced all material and results that are not original to this work.

Name, Last name: Emre Burak Ertuş

Signature:

ABSTRACT

PRODUCTION AND CHARACTERIZATION OF HIERARCHICALLY POROUS TRANSPARENT GLASSES

Ertuş, Emre Burak
Doctor of Philosophy, Metallurgical and Materials Engineering
Supervisor: Prof. Dr. Abdullah Öztürk
Co-Supervisor: Assoc. Prof. Dr. Çekdar Vakıf Ahmetoğlu

January 2020, 104 pages

A sodium borosilicate glass (SBG) with nominal composition of $55.7SiO_2$-$33.6B_2O_3$-$9.2Na_2O$-$1.5Al_2O_3$ (wt %) was produced by the conventional melt-quenching method. The as cast SBG was heat treated at various temperatures to induce phase separation. The phase separated glass was then acid (HCl) leached using three different HCl molarities to dissolve alkali-borate phase hence, to obtain a porous glass (PG). In order to control the pore structure and to find out a correlation between the pore architecture and the resulting properties, PG was subsequently alkali (NaOH) leached or heat treated at 800 °C for 1 h. The effects of the applied heat treatment temperature and acid concentration of leach solution on pore architecture were investigated. Results revealed that the heat treatment temperature influences the width of liquation channels whereas, the primary pores associated with silica precipitates were more affected by the molarity of the acid leaching solution. The total pore volume of PG increased by alkali leaching but decreased by additional heat treatment.

The microhardness and tribological properties of parent SBG and PGs were evaluated. The microhardness was lower but, wear rate was higher than that of the parent SBG for all PGs.

TiO$_2$ crystals were grown within the pores of PG and the results were evaluated in terms of the appropriateness of this system for wastewater treatment. Methylene Blue (MB) degradation tests revealed that the TiO$_2$ embedded PG (TiPG) has photocatalytic activity under UV illumination and could be utilized as a promising material in wastewater treatment.

Keywords: Porous Glass, Phase Separation, Wear, Titanium Dioxide, Photocatalytic

ÖZ

HİERARŞİK GÖZENEKLİ SAYDAM CAMLARIN ÜRETİMİ VE KARAKTERİZASYONU

Ertuş, Emre Burak
Doktora, Metalurji ve Malzeme Mühendisliği
Tez Yöneticisi: Prof. Dr. Abdullah Öztürk
Ortak Tez Yöneticisi: Doç. Dr. Çekdar Vakıf Ahmetoğlu

Ocak 2020, 104 sayfa

Ağırlıkça yüzde olarak $55.7SiO_2$-$33.6B_2O_3$-$9.2Na_2O$-$1.5Al_2O_3$ nominal bileşimine sahip bir sodyum borosilikat cam (SBG) geleneksel ergitme-döküm yöntemiyle üretilmiştir. Faz ayrışmasını sağlamak amacıyla SBG farklı sıcaklıklarda ısıl işleme tabi tutulmuştur. Faz-ayrıştırılmış cam, gözenekli cam (PG) elde etmek amacıyla üç farklı molaritedeki asit (HCl) çözeltinde liç edilerek alkali-borat fazın çözünmesi sağlanmıştır. Gözenek yapısını kontrol etmek ve gözenek mimarisi ile ortaya çıkan özellikler arasında bir ilişki bulmak amacıyla PG'ye daha sonra alkali (NaOH) liç veya 800 C$^\circ$'de 1 saat ısıl işlem uygulanmıştır. Isıl işlem sıcaklığının ve liç çözeltisinin asidik konsantrasyonun gözenek mimarisi üzerindeki etkileri incelenmiştir. Isıl işlem sıcaklığının esas olarak sıvılaşım kanallarının genişliğini etkilediği, fakat silika çökeltileri ile ilişkili birincil gözeneklerin liç çözeltisinin asidik konsantrasyonundan daha fazla etkilendiği belirlenmiştir. Gözenekli camın toplam gözenek hacmi alkali liç ile artmış, bunun yanında ilave ısıl işlemle azalmıştır.

Üretilen SBG ve PG'lerin mikro sertliği ve tribolojik özellikleri incelenmiştir. Tüm gözenekli camlar için mikro sertlik değerlerinin daha düşük olduğu, ayrıca aşınma oranlarının SBG'den daha yüksek olduğu görülmüştür.

TiO$_2$ kristalleri PG'nin gözenekleri içerisinde büyütülmüştür. Sonuçlar bu sistemin atık su arıtımı için uygunluğu açısından değerlendirilmiştir. Metilen Mavisi (MB) bozunum testleri TiO$_2$ emdirilmiş PG'nin (TiPG) UV ışık altında fotokatalitik aktivite gösterdiğini ve atık su arıtımında umut verici bir malzeme olarak kullanılabileceğini ortaya koymuştur.

Anahtar Kelimeler: Gözenekli Cam, Faz Ayrışması, Aşınma, Titanyum Dioksit, Fotokatalitik

To my family

ACKNOWLEDGMENTS

TABLE OF CONTENTS

LIST OF TABLES

TABLES

LIST OF FIGURES

FIGURES

xvii

LIST OF ABBREVIATIONS

ABBREVIATIONS

PG: Porous glass

TiPG: TiO_2 embedded porous glass

SBG: Sodium borosilicate glass

CPG: Controlled pore glass

SSA: Specific surface area

PSD: Pore size distribution

V_P: Total pore volume

Tg: Glass transition temperature

W: Wear rate

μ: Friction coefficient

H_V: Vickers hardness

DTA: Differential thermal analysis

TGA: Thermogravimetric analysis

XRD: X-ray diffraction

JCPDS: Joint committe on powder diffraction standards

SEM: Scanning electron microscopy

EDS: Energy dispersive X-ray spectroscopy

FTIR: Fourier transformed infrared spectroscopy

UV-Vis: Ultraviolet-visible

Eg: Band gap energy

MB: Methylene blue

RE: Removal efficiency

PP: Photocatalytic performance

CHAPTER 1

INTRODUCTION

"*Porous materials are like music: the gaps are as important as the filled-in bits*" as Lu and Zhao [1] pronounce in their book. Nowadays, with the rapidly developing technology and science, the importance of porous structures is increasing and their usage in industrial areas including biotechnology, chemistry, electronics, environmental purification, and mechanical engineering becomes more than ever. Among porous materials, porous glasses (PGs) have a distinctive importance with its unique engineering properties as compared to other materials such as ceramics, metals, polymers, and composites.

Depending on the pore size, PG may exhibit optical transparency, decent mechanical stability and high chemical resistance to most organic solvents and acids (except HF) [2]. Also the surface chemistry and pore size distribution can be adjusted depending on process variables [3,4]. Because of the desirable properties PGs could be used in special industrial applications such as separation membrane [5], microfiltration [6], catalyst support [7], optical chemo-sensors [8], and drug delivery systems [9] with a wide variety of geometric forms such as beads, fibers, membranes, and monoliths [10,11].

PG can be prepared by several different routes such as sacrificial templating [12], partial sintering [13], high temperature bonding [14], blowing agents [15], sol-gel [16], etc. Compared to other techniques, creating a porosity by phase separation and acid leaching is commonly practiced way because it is rather easy to control the pore topology and it suits better for low cost, mass production.

The production of PG by phase separation was first reported in the 1920s. The first step in the development of this technology as stated by Turner and Winks [17] relies on the separation of boron-containing glasses into two phases with different chemical

1

stability. This achievement gained a commercial importance when Hood and Nordberg, the pioneers of PG technology, discovered Vycor process that is still widely practiced to produce glasses with high silica content exhibiting properties like quartz glass does [18]. In Vycor process, an alkali borosilicate glass is exposed to spinodal decomposition (i.e. phase separation) followed by selective leaching of alkali-borate phase by aqueous acidic solutions [10,18]. The resultant amorphous porous material with high silica (SiO_x) content (~96 wt %) could further be sintered to obtain highly dense glass products [10]. In order to produce permeable glass components with high surface area, phase separated glasses can be leached out to produce PG. If the resultant component is interested to be porous, its pore size can be controlled in a broad range from 0.3 to 1000 nm with a surface area reaching ~340 m^2/g [19] by altering the processing conditions such as initial batch composition, heat treatment temperature and time, and details in the following leaching procedures [11].

Sodium borosilicate glasses (SBGs) are the most commonly studied glass family that can be phase separated to silicate and borate rich (alkali-borate) phases by applying a regulated heat treatment. These phases actually form three-dimensionally entangled, continuous, split networks in the same glass matrix [20]. During the phase separation, certain amount of silicate phase dissolves in the alkali-borate phase. However, still what is so called liquation channels are formed when alkali-borate rich phase is leached out by aqueous acidic solutions, generating interconnected open-pore structure in the remaining silicate matrix [10]. The silicate domains/regions of the dissolved alkali-borate phase may remain in the leaching solution as colloidal silica, coagulating to form silica clusters that cannot be dissolved in the acidic solution [19,21,22]. The silica clusters remaining inside the channels can be removed by basic (alkaline) solutions which may further enlarge the channel diameter as well [23]. If the final structure is successively heat treated (e.g. at 900 °C for 70 h) [2] viscous flow sintering leads consolidation. This procedure can also be used to design the final pore architecture [24–26].

In spite of good peculiarities, studies reporting the mechanical and structural properties of PG are very limited [27–29] in fact there is no systematic study reported in the open literature on the tribological behavior of PG. An understanding on the mechanical and tribological behavior of PGs as well as on the factors affecting the production of PGs could extend its utilization in industrial applications involving adverse conditions since the production steps and parameters of PGs directly affect the chemistry and morphology of the resultant product and its properties. The mechanism(s) taking place during the production of PG by the phase separation followed by acid leaching is still ambiguous. Further research is needed to understand the structural development and to improve the properties of PGs.

1.1   Objectives

The objectives of the present work were;

- to produce the PGs with various pore architectures.
- to investigate the effects of several production variables including heat treatment temperature, molarity of the acid leaching solution, alkali treatment and heat treatment after acid leaching on the pore size distribution, pore volume and specific surface area.
- to examine the hardness and tribological properties of the PGs produced.
- to evaluate the suitability of the PGs produced for wastewater treatment.

CHAPTER 2

LITERATURE REVIEW

2.1 Overview of the Pores and Porosity

IUPAC (The International Union of Pure and Applied Chemistry) define a porous solid as a solid material having channels, cavities or interstices deeper than its width [30]. Porosity is the ratio of the pore volume to the total apparent volume of the particle or powder. The first point of classifying porous solids is whether the pores are closed or open. Pores which are entirely isolated from their neighbors, as shown in region (a) in **Figure 2.1**, or sometimes connected with the neighboring pores but eventually causing no permeability to whole system, are described as closed pores. Open pores are connected to the external surface of the body with continuous channels like in **Figure 2.1** (c). The pores which are open only at one end like in **Figure 2.1** (b) defined as blind pores and the ones open at two ends and connected with other pores described as through or interconnected pores like in **Figure 2.1** (d).
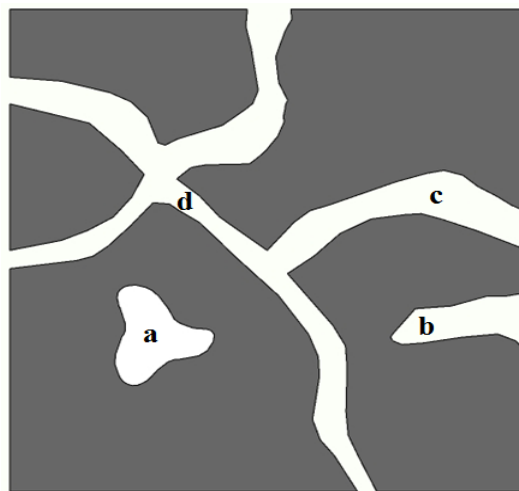
Figure 2.1. Schematic representation of the cross section of a porous solid [30].

Pore size, also sometimes defined as pore diameter or width, is the distance between two opposite walls of the pore such as diameter of cylindrical pores or width of slit-shaped pores. In 1972, IUPAC classified pore sizes in three main groups; micropore: width smaller than 2 nm, mesopore: width between 2 and 50 nm, and macropore: width greater than 50 nm [30].

Since the early 2000s, scientists have become more interested in hierarchically structured porous materials. The term "hierarchically porous" can be defined as a porous material containing pores on more than one length scales i.e., ranging from micro, meso, and macropores [31]. Hierarchically porous structure increases the potential application areas of porous solids and optimizes porous materials for some specific cases [32]. For example, smaller pores provide high specific surface area (SSA) and improve the host–guest interactions so that they can be utilized for catalysis and sensor applications. On the other hand, the presence of macropores favors mechanical stability and the diffusion of large molecules. Hierarchically porous materials categorized as either bimodal (micro-macro, micro-meso, meso-macro) or trimodal (macro-meso-micro) [31,32].

Hierarchically porous materials could be synthesized by various methods but, simply two main routes are considered; (i) the inclusion of macro-templates into the reaction media, together with small-scale templates and (ii) the modification of the method parameters [31,32].

2.2   Porous Materials

All materials such as polymers, metals, ceramics and glasses, can be produced with pores. The common application areas of porous solids are; gas separation membranes, catalytic membranes, thermal insulators, electronic substrates, fuel cell electrodes, battery separators, gas storing materials, filters and selective adsorbents [4,33]. Each application of porous materials requires different desired properties such as high SSA, specific pore size distribution, high pore volume, mechanical

strength, chemical stability and thermal shock resistance, etc. The relevance between the material type, pore size and the application area of the porous solids are outlined in **Figure 2.2** [33].
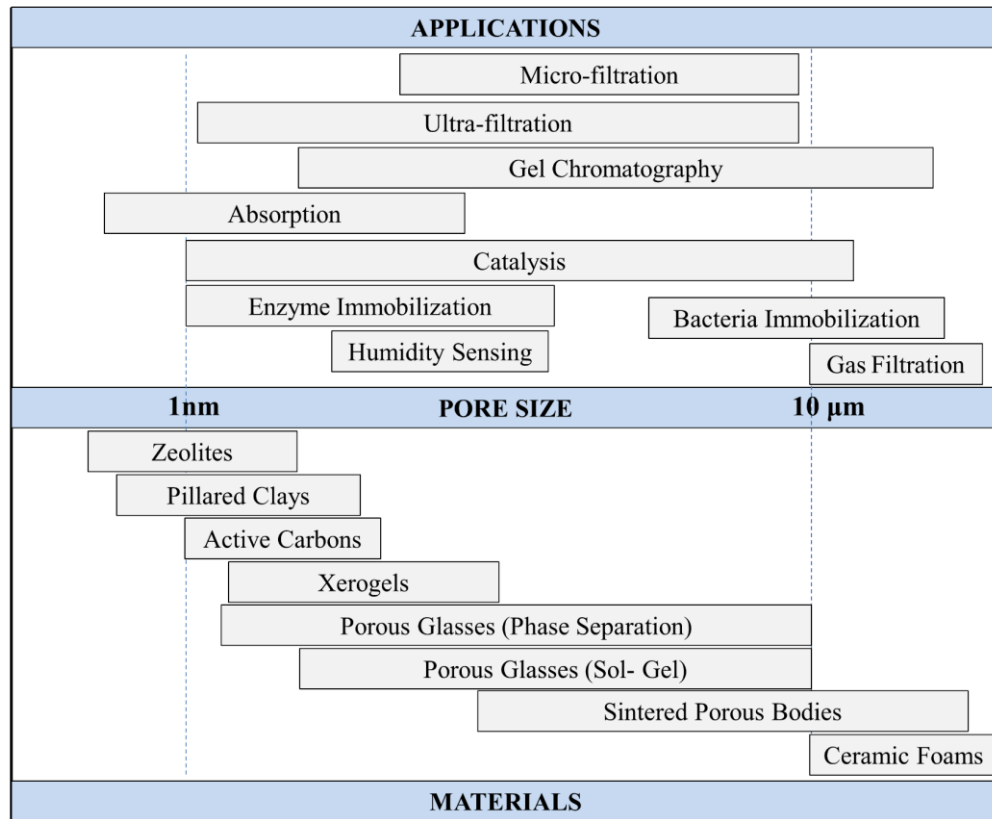
Figure 2.2. The relevance between the material type, pore size and the application area of the porous solids [33].

Porous metals are significant by their mechanical properties such as toughness and strength. They are preferred materials when energy absorption is desired due to their ability to undergo plastic deformation, e.g. aluminum foams are one of the most widely used porous metals. Nickel foams used as battery electrodes and porous titanium alloys utilized as biomaterials, are the examples of the most commonly used porous metals [34].

Porous polymers are low cost porous materials but they have the disadvantages of low thermal resistance, restricted mechanical properties and, toxicity. Utilizing porous polymers as insulators and ion-exchange resins are most common

applications for many years. Also, with developing polymer technology, porous polymers have been serving as materials for column chromatography and gel separation media [4].

Porous ceramics and glasses are important members of the porous materials with their high thermal and chemical resistance. Activated carbon, mcm-41, porous alumina, porous glasses, and zeolites are among the most popular porous ceramics on which scientists have been working for many years [4,35,36].

2.3   Porous Glasses

A glass is simply defined as a non-crystalline solid which exhibits glass transformation behavior [20]. Glass is an inorganic material possessing short-range atomic order. While many different novel methods of glass production have emerged with the developing science and technology in recent years, commercial glasses are mainly produced by fusing batch components at elevated temperatures. The batch components are selected and weighed according to the type of glass to be produced. They undergo many physical and chemical changes during the melting process and form the glass melt [20,37].

On the basis of their role in the glassmaking process the glass batch materials can be divided into five categories; network formers, intermediates, modifiers, colorants, and fining agents [37]. Glass formers are the primary source of the glass structure to form a highly cross-linked network of chemical bonds and serves as the basis for the generic name used for the glass. SiO_2, B_2O_3 P_2O_5, and Al_2O_3 are the most common glass former oxides. The glass modifiers are alkali and alkaline earth oxides such as Na_2O, K_2O, CaO, and MgO. They disrupt the glass network thus reduce the processing temperature. They decrease the glass forming tendency when added to glass forming batches but, decrease chemical durability. Intermediate oxides like Al_2O_3, ZrO_2, and TiO_2 partially counter the reduction in properties of the resulting glass. Colorants are added in small quantities to control the color of the final glass.

Fining agents such as As_2O_3 and Sb_2O_3 get rid of gas bubbles present in the melt and very essential for commercial glass production [37].

The term "Porous Glass (PG)" is reserved for the glass containing some amount of porosity derived by acid leaching of phase separated sodium borosilicate glass (SBG) [10]. PG also covers amorphous silica materials produced by many methods such as sintering [13], high pressure sintering [38], sol-gel [16,39], colloidal suspension foaming method [40], preceramic polymer method [41], electrospinning [42], sacrificial template method [12] and, derived by using foaming agents [15]. Among these methods, the phase separation followed by acid leaching, often referred to as "Vycor Process", is most commonly practiced because it offers several advantages for example suitability for low cost mass production, formation of narrow pore size distribution and, reusability of waste glass. PGs derived by phase separation and acid leaching, in other words phase separated PG is the main focus of this dissertation study.

2.3.1   Phase Separated Porous Glass

In 1938, Hood and Nordberg discovered a unique process that circumvents the need for high temperatures in melting and forming the high silica containing glass. They patented this method under the trade name "Treated Borosilicate Glass". The formation of 96% SiO_2 containing glass by leaching of phase separated SBG is frequently called the Vycor process after the name of a commercial material produced by Corning Glass Works Company [10,18]. There are simply four main steps in Vycor process [10];

  i. Heat treatment of an alkali borosilicate glass, mostly SBG, to provide phase separation in the temperature range 500-750 °C.
  ii. Leaching out the soluble alkali-borate phase from the heat treated glass by hot dilute acid solutions containing either one of the acids HCl, HNO_3, and H_2SO_4

to generate the interconnected open-pore structure what is called liquation channels in the remaining silicate matrix.

iii. Washing and drying the porous structure left from the acid leaching process.

iv. Final heat treatment slowly up to 1200 °C to provide consolidation.

Upon completion of these steps, a dense glass with a composition 96% SiO_2, 3% B_2O_3, 1% Al_2O_3 or ZrO_2 in weight percentage (wt %) could be obtained. If this process is intervened in the third step, i.e. before the consolidation heat treatment, it is possible to get a PG which contains approximately 35 volume percentage (vol %) interconnected porosity. This intermediate product is what actually called as Porous Vycor Glass. The physical properties of the phase separated PG depends mainly on three parameters of production process; (i) the composition of initial glass, (ii) the heat treatment conditions (time and temperature) and, (iii) the acid type and leaching conditions [10,11].

PG is distinguished from other porous solids by reason of its unique sponge-like interconnected microstructure. It is an amorphous porous material with very high SiO_2 content (~ 96 wt %). Pore size can be controlled in the range between 0.3 and 1000 nm and also high pore volumes together with large SSA can be achieved [11]. Depending on the pore size, PG can exhibit high optical transparency and good mechanical stability. Besides, it shows high chemical resistance to acids (except HF) and organic solvents. PG monoliths can be manufactured with various geometries for instance; beads, plates, rods, tubes, fibers, and ultrathin membranes [2,10,11]

Haller carried out a study on phase separation kinetics of alkali borosilicate glasses in 1965 [43]. He reported that the finely dispersed silica clusters remains in the cavities of the main silica framework because of the small amount of silicate dissolved in alkali-borate phase that has a low solubility in acidic media. This silica clusters effects the pore structure and pore volume of the resulting PG. The colloidal silica deposits can be removed by alkali solutions and alkali treated PG products termed "Controlled Pore Glass (CPG)" is produced. A very narrow pore size distribution over a range from 7.5 to 300 nm can be tailor-made in CPG [4,23,43,44].

2.3.1.1   Boron Anomaly

A continuous change in properties is observed when alkali oxide content is increased in borosilicate glass. Small additions of alkali oxides to vitreous silica breaks oxygen bonds and creates non-bridging oxygen (NBO) thus, results in a decrease in glass transition temperature (Tg). However, this is not valid for alkali borate glasses, until about 16 mol% alkali oxide additions cause an increase in Tg. Boron occupies both 3-fold [BO_3] and 4-fold [BO_4] coordination in oxide crystals [37]. Small additions of alkali oxide to alkali borate glasses transform BO_3 groups to BO_4 groups without NBO formation. This change in structure increases the connectivity of the network so that Tg increases and the thermal expansion coefficient of the glass decreases. When BO_4 groups reach a critical concentration, further alkali oxide additions causes the formation of NBO, which results in a reversal in property/composition trends [20,37]. This unusual behavior (a reversal in the properties with increasing alkali content) in alkali borate glass is termed as "boron anomaly".

The phase separation phenomenon in SBG is originated from boron anomaly and as a result of this relation the miscibility gap, to be discussed in Section 2.3.1.2, reaches a maximum around 16 mol% Na_2O. BO_4 have an excess negative charge of -1 so act as anion [20]. BO_4 must be accompanied by a cation to ensure local charge neutrality and for the SBG system the associated cation is NaO_2. **Figure 2.3** represents the composition region of phase separation in the sodium borosilicate ternary and the straight line represents increasing SiO_2 content at constant $Na_2O:B_2O_3$ ratio=16:84. The line corresponds to the maximum immiscibility in the binary, and the "anomaly" concentration. The ternary immiscibility region covers this line and immiscibility decreases with each departure from the 16:84 region [20,37].
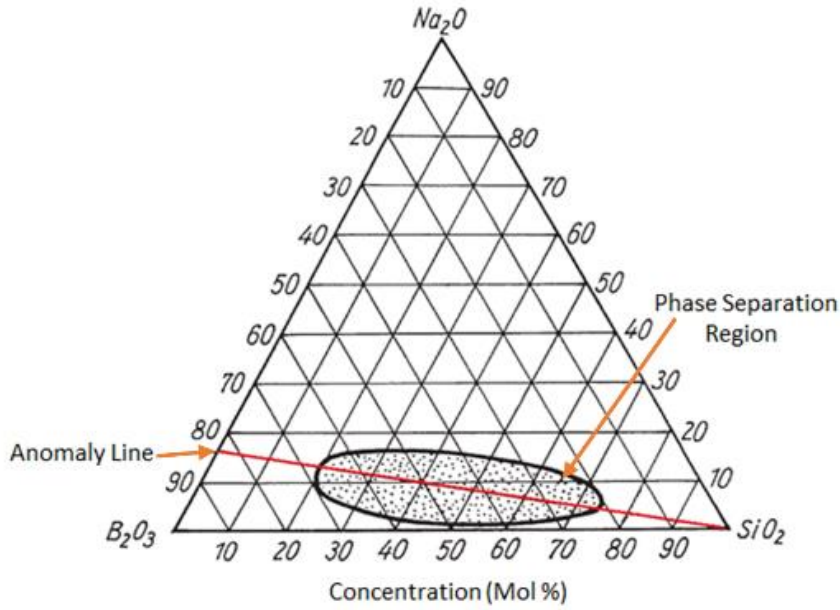
Figure 2.3. The composition region of phase separation and anomaly line in the sodium borosilicate ternary diagram [20].

2.3.1.2   Phase Separation Phenomenon

In glass forming melts, phase separation or liquid-liquid immiscibility is a common phenomenon. Phase separation can be explained by the thermodynamics of regular solutions. The free energy of mixing of a solution, ΔG_m, is related to the enthalpy of mixing, ΔH_m, and entropy of mixing, ΔS_m, by the expression:

$$\Delta G_m = \Delta H_m - T\Delta S_m \tag{1}$$

For regular solutions, at temperature T, ΔH_m and ΔS_m is given as [20,45]:

$$\Delta H_m = \alpha.X_1.X_2 \tag{2}$$

$$\Delta S_m = -R.[X_1.lnX_1 + X_2.lnX_2] \tag{3}$$

Where; X_1 and X_2 are mole fractions of the phases 1 and 2, respectively, R is the gas constant and, α is a constant related to the energy of the bonds among the various components. Combining the equations (2) and (3), the expression below is obtained.

12

$$\Delta G_m = \alpha . X_1 . X_2 + T . R . [X_1 . \ln X_1 + X_2 . \ln X_2] \qquad (4)$$

Phase separation occurs if the separation of the mixture into two components yields a lower free energy. Simply; if $\Delta G_m > 0$, mixing is not favored. As anticipated from expression (4), in the cases where α is positive, the sign of ΔG_m can be negative or positive depending on the temperature. The phase diagram (temperature vs. composition) resulting from this behavior will exhibit a shape like dome and the region inside the dome is called the miscibility gap. At sufficiently high temperatures above the maximum temperature of the miscibility gap that is termed as critical temperature (T_{CR}), the free energy of mixing is always negative and mixing is favored above T_{CR} [20]. In the miscibility gap region, if kinetic conditions do not hinder the phase separation, the melt will spontaneously separate into two phases whose compositions are expected by their location on the dome. If the viscosity of the glass melt is too high, below the glass transition region (T<Tg) phase separation will not occur. Likewise, at temperatures greater than $T_{CR,}$ phase separation is not possible. Consequently, a glass melt can change its microstructure through phase separation between the temperatures T_{CR} and Tg [4,20].

There are two phase separation mechanisms, results in relatively different microstructures in the glass. The first mechanism is "nucleation and growth" where it is valid in the metastable region of the miscibility gap. The new nucleus forms and grows without a change in chemical composition over time [20]. The separated phase occurs as "isolated/droplet like" spheres in a continuous matrix as shown in **Figure 2.4** (Region I and III). The second mechanism is "spinodal decomposition". This mechanism is valid in the unstable region of the miscibility gap and involves a gradual change in composition of the two phases until they reach the immiscibility boundary where the free energy of the system is at the lowest state [20]. The interface between the phases will initially be very diffuse, but will sharpen with time. Finally both phases will have a high degree of connectivity and each phase have continuous pathways through material. This morphology, shown in **Figure 2.4** (Region II) is termed "interconnected/worm-like" structure [20].
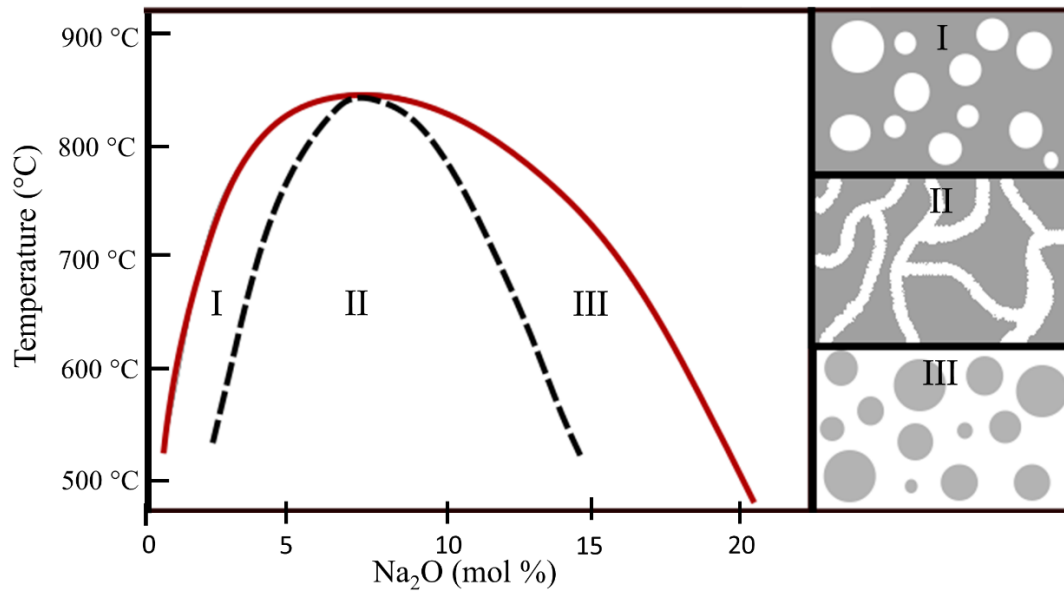
Figure 2.4. Immiscibility diagram for the sodium silicate system [20].

2.4   Previous Studies on Porous Glass

Until now, several studies [19,22,23,44,46–51] were performed on the production of PG and on their properties and applications. The examinations of the effects of the several production step variables on the physical properties of PG are an important and remarkable part of these studies.

The initial glass composition is the first parameter that determines the total pore volume, pore size distribution, and specific surface area of PG [4]. Researchers have shown that minor components such as Al_2O_3 [52], Zr_2O_3 [50], and NaO_2/B_2O_3 molar ratio [4] added to the alkali borosilicate glass affect the resultant pore structure. If simply the SiO_2 ratio of the composition chosen within the immiscibility dome shown in **Figure 2.5** is considered, changing the composition from point 1 to point 2 that are in the same temperature line will cause the increase of soluble phase volume ratio. Thus total pore volume may increase after etching as well.

14
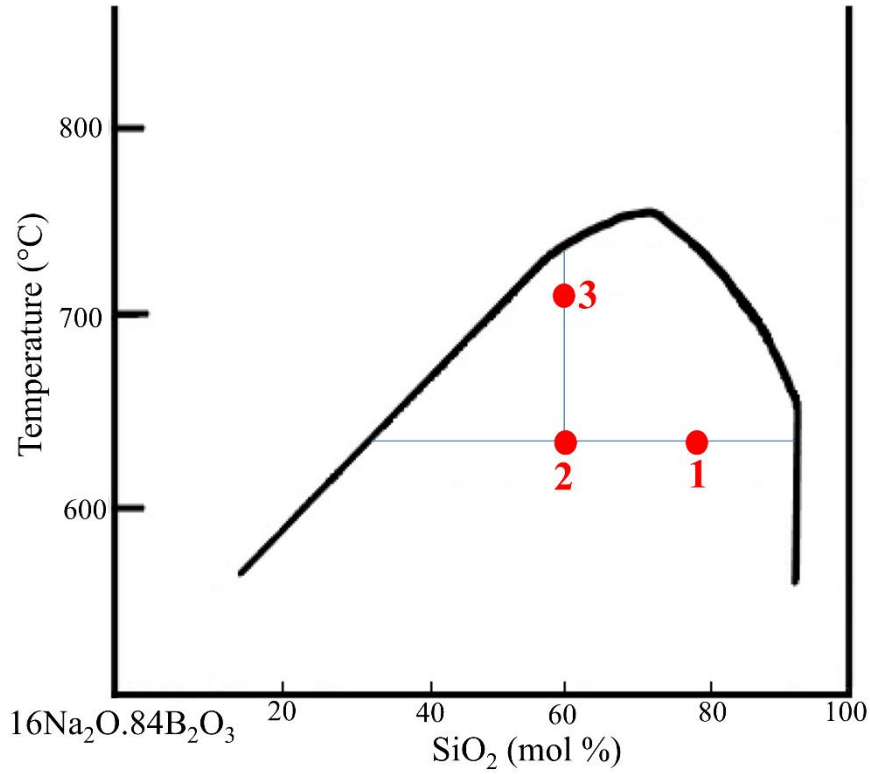
Figure 2.5. Asymmetrical immiscibility dome in the system Na_2O-B_2O_3-SiO_2, alongside the anomaly line [4].

The variation in the heat treatment temperature affects both the soluble phase volume and the chemical compositions of the phases separated. Increasing the heat treatment temperature, that is changing the temperature from point 2 to point 3 in **Figure 2.5**, will cause the increase of soluble phase volume ratio and the SiO_2 content in the soluble phase although the composition is the same. The solubility of sodium borate is relatively low in the SiO_2-rich phase, because of the steep right flank of the asymmetric miscibility dome. In contrast, the left side (i.e. alkali borate rich part) of the dome where the curve is not steep, indicates a strong increase of SiO_2 solubility in the primarily formed alkali-borate phase with increasing temperature. During acid leaching process, the silicate-rich regions remaining in the alkali-borate phase pass into the leaching solution and form colloidal silica ($Si(OH)_n$) [19].

The dissolved silica coagulates inside the liquation channels as dispersed silica-gel [4,23]. When the colloidal silica fills the pores of the structure, the pore volume is

reduced and so the diffusion through the porous glass. For these reasons, the total pore volume of PG first shows an increasing trend with increasing heat treatment temperature then decreases when the colloidal silica concentration reaches a critical level [4]. However, Enke et al. [19] suggested that with increasing silica concentration in the alkali-borate phase, silica forms an independent network in the alkali borate phase. This network cannot be dissolved by the acidic solution and retains in the PG structure after the leaching process.

Takamori and Tomozawa [53] studied the HCl leaching rate of a SBG. The leaching rate significantly increased with increasing heat treatment time for heat treatments at low temperatures however, only a minor increase in leaching rate was observed with increasing heat treatment time for heat treatments at high temperatures. It was concluded that the maximum leaching rate depended on the heat treatment temperature upon heat treatment for a long enough time. Also, the composition of the alkali-borate phase was still fluctuating to reach the equilibrium composition even after 400 h. The HCl leaching rate of borosilicate glasses also depends on the composition of the glass and the microstructure of the soluble phase.

Zhou et al. [48] studied the effect of heat treatment parameters on the pore structure of PG. They reported that the SSA and pore volume become larger with increasing heat treatment time and temperature. Spinodal decomposition could be formed during cooling of molten glass. If there was no additional heat treatment applied to SBG in order to promote phase separation, the pore size of PG depended on the cooling rate of the molten glass. Yazawa et al. [51] reported that the roller-quenched samples (106 K/s) have less pore volume and surface area than the air-quenched samples (10 K/s). For both cases the final material had pore diameter less than 1 nm. Shimbo [54] stated that the leaching process of PG can be divided into three main steps; i) diffusion of reactants (acids) from bulk solution to the glass interface through the pores for leaching of the glass, ii) hydrolysis (leaching) reaction of alkali-borate phases in the rigid glass, iii) diffusion of hydrated products to the bulk solution. There was a linear relationship between square root of leaching time and

the thickness of leached layer implying that the leaching process is controlled by diffusion and the first step is the rate determining one.

The interaction of the leaching solution with phase separated SBG consists of three stages; the dissolution of the soluble alkali borate phase, the diffusion of the interchanging substances from glass to the leaching solution and, the precipitation of colloidal silica particles within the liquation channels [55–57]. Another important parameter controlling the pore structure is the molarity of the acid leaching solution. At low acid molarities, the solution may not be strong enough to dissolve all the alkali borate phase resulting relatively low SSA and total pore volume. Increasing the acid molarity causes higher amount of alkali-borate and silica-rich interface to dissolve. Also due to the low solubility of colloidal silica, SiO_2 aggregates remain finely dispersed within the pores of the silica framework. This leads to increase in the SSA where most of the surface area of a PG results from the silica particles. Also increasing the acid molarity may cause an increase in the total pore volume, essentially due to larger dissolution of the alkali-borate phase interface [22].

At high acid molarities, the small silica particles may precipitate due to the hydrolysis-condensation phenomenon [4]. The agglomeration of the silica precipitates leads to the formation of silica clusters with large diameters. The agglomerated silica precipitates could also block liquation channels leading a lower total pore volume and SSA. After leaching, the pore size of PG strongly depends on the size and packing density of silica clusters in the liquation channels [19,22,58]. **Figure 2.6** schematically shows the characteristic pore structure of PG. The gaps between silica precipitates are referred to as primary pores and the gaps between liquation channel walls are named as secondary pores.

Liquation Channels SiO_2 Clusters   Secondary Pores   Primary Pores
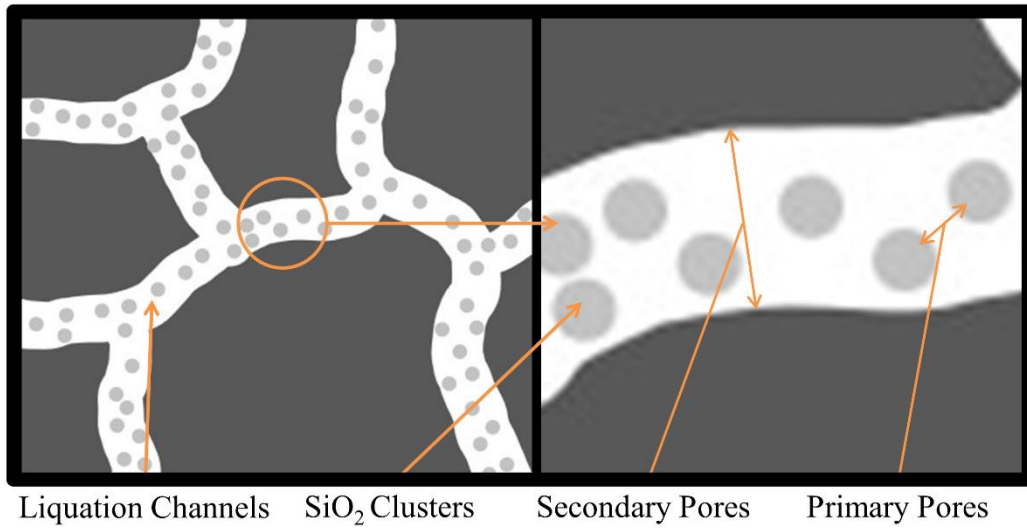
Figure 2.6. The pore structure of PG.

Toquer et al. [22] reported that SSA and total pore volume can be tailored regarding the acid concentration and leaching time. Increasing the HCl concentration up to 0.7 M caused an increase in SSA and total pore volume but, further increases resulted in a decrease in both properties. Similarly, Kreisberg et al. [47] studied the effects of acid concentration on the pore size. They demonstrated that two main pore sizes existed in the structure of PG. The first one is the mesopore with bimodal pore size distributions; in the range of 3.6-4.6 nm arising from gaps between secondary silica clusters in the channels formed upon phase separation and in the range 17-21 nm can be associated with the diameters of channels that are almost free from silica clusters. The second one is the micropore formed in regions of cluster contacts, which has 0.6 nm pore size. When the HCl concentration of the leaching solution was increased from 1 M to 3 M the mesopore and micropore volumes hence SSA decreased.

Tanaka et al. [59] studied the precipitation of colloidal silica in liquation channels. The authors emphasized that the acid solution volume/glass mass ratio is one of the most important factor that dictates the size and volume of primary pores where heat treatment temperature has no significant effect on. Kawamura et al. [60] observed that the pore structure depends on the thickness of glass pieces so that the larger pores exist in the surface layer of the piece while the small ones remains in the inner

18

part. Kreisberg and Antropova [58] performed an extensive research on the effects of production parameters on pore structure in 2014 and reported that the size and packing density of silica clusters govern the pore structure of PG. They defined mesoporosity by the width of the gaps between walls and liquation channels and microporosity in places of secondary silica cluster contacts. Alkali treatment removed silica clusters. So, microporosity almost vanished and mesoporosity was controlled by the diameter of liquation channels. The schematic drawing of CPG microstructure at different stages of production is depicted in **Figure 2.7**.
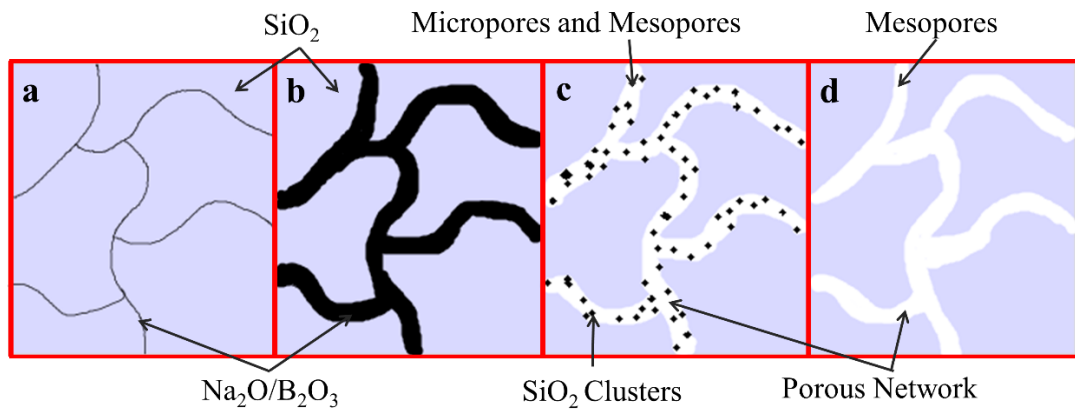
Figure 2.7. The schematic microstructure of CPG at different stages of production: (a) quenched glass (b) phase separated glass after heat treatment (c) porous structure after acid leach (d) porous structure after alkali leach.

The stress development in PG is very important and must be taken into account to ensure that the final product is not cracked or broken as all PGs are produced after single or multiple leaching procedures. Scherer and Drexhage [61] studied the reasons of the stresses in PG and indicated that there are four main sources for stress.

i. The first one is thermal stress due to thermal expansion coefficient mismatch of the two separated phases formed during cooling. When the alkali borate phase which has high thermal expansion coefficient is removed, the thermal stresses are relieved and the residual silica rich phase tends to expand.

ii. Second one is capillary stresses associated with the surface energy incensement of the residual PG.

19

iii.   Third reason is the ion exchange by the acid with the silica rich phase during leaching.

iv.   The last reason is hydration; the absorbed water into the solid phase causes compression stresses.

In order to have crack free glass monoliths, swelling or shrinking tendency of silica rich phase must be eliminated. The first point to note is that the leaching process should be adapted to the entire volume and no unleached parts should remain in the final product. Kukizaki and Nakashima [49] examined the reasons of the PG membrane cracking during acid leaching. The authors suggested that PG membranes can be produced without cracks when the rate determining reaction model of the leaching process is the leaching reaction at the interface rather than the diffusion of reactants. If the average pore size is less than 200 nm, the remaining silica clusters expand at elevated temperatures, leading to cracking by inhibiting the diffusion of the reactants, and the way to avoid such issue is to leach at the lower temperatures. Besides, the glass composition should be chosen carefully. In 1942, Hood and Martin [62] patented the optimum glass composition to manufacture crack free glasses. The appropriate composition range is formulated as shown in **Eq. 5.** [63].

$$(Na_2O)=9.5-0.1[S]-0.17[A]^2 \tag{5}$$

Where; $[S]=SiO_2-55$, $[A]=Al_2O_3$ and balance up to 100% is B_2O_3 by weight The authors reported that Al_2O_3 additions up to 4 wt% strengthen the glass structure against devitrification and deformation. The fraction of 4-fold coordinated boron decreases as the amount of Al_2O_3 is increased. If one considers that the origin of phase separation is the tendency of sodium ions to accompany with 4-fold boron to provide electrical neutrality, phase separation is suppressed with the decrease in 4-fold boron fraction. Also, the –B-O-Al– bond with 3-fold boron formed in Na_2O-B_2O_3-SiO_2-Al_2O_3 glasses is difficult to be broken due to the high bond energy. As a result, spinodal phase separation is greatly inhibited by Al_2O_3 addition [52].

Stolyar et al. [24] investigated the shrinkage of PG at elevated temperatures. They reported that there was a small expansion up to 250 °C due to moisture removal but,

shrinkage observed for the samples heat treated between the temperature range 300-550 °C because of sintering of secondary silica particles and surface dehydroxilation. Between 600 and 800 °C, the shrinkage of the samples increases drastically due to softening of silica skeleton. Similarly, Volkova et al. [26] and Yamamoto et al. [64] reported that the total pore volume of PG decreased due to the sintering of the smallest pores at temperatures above 700 °C.

In order to widen the pore size distribution range and to have macropores together with mesopores, other production methods can be used together with the phase separation method. Reinhardt et al. [27,65] successfully prepared hierarchically structured, mesoporous-macroporous monoliths by a combination of salt-sintering and phase separation of a SBG. Secondary pores between 20 and 150 μm formed after an aqueous leaching of the glass-salt-composite. The pore size of the final component can be designed by controlling the process parameters of sintering and different grain fractions of glass and salt particles. Also, different primary pores ranging from 1 to 70 nm can be formed by annealing and successive acid leaching. The resulting hierarchical PG exhibited surface areas up to 420 m^2/g and total porosity up to 74%. In a different approach, hierarchical PG foams having primary pores down to 3 nm and secondary pores up to 1 mm were prepared by Reinhardt et al. [66] via combination of phase separation and sacrificial templating.

2.5   Applications of Porous Glass

The application areas of PG are limited only by the imagination of industrialists since it has unique customized properties. The diversity of the applications areas is understood better as the remarkable results of the outstanding scientific studies performed on PGs in recent years are investigated.

Kim et al. [67] reported that LiPF$_6$ infiltrated PG has potential to be utilized as hybrid electrolyte membrane in lithium secondary batteries due to its nano-scale pores. Schadeck et al. [68] utilized PG as a novel separator for lithium-ion batteries as an

alternative to polymer-based separators at high temperatures and they concluded that PG platelets are suitable for high current battery applications. PG can be utilized also as a solid adsorbent medium to remove organic or inorganic pollutants from industrial and agricultural wastewaters. Kuznetsova et al. [69] investigated the adsorption efficiency of PG in diluted iron(III) chloride solutions and they revealed that the maximum adsorption value of iron ions was 3.4×10^{-11} mol/cm^2. Mazilu et al. [70] have characterized bio-properties of PG and emphasized that PG permitted a good cellular viability and proliferation.

Sensor applications have been one of the most popular application areas since PG was discovered. In a typical sensor application, a sensitive molecule is fixed on the PG utilized as support material. The sensitivity of the device can be increased by taking advantage of the high SSA of PG. Gas sensors such as Ozone and NO_2 [71–73], pH sensor [8,74] and, biosensors [75] are few of the examples.

Polymer-PG composites are one of the interesting application areas. O'Brien et al. [28] suggested a novel transparent polymer- porous glass composite can be used as an intermediate acoustic impedance layer material of the lightweight laminated composite armor. The transparent nanocomposite was created by infiltrating PG with different polymers.

Metallic or metal oxide nanoparticles inside the pores of PG generate completely new possibilities for PG applications. Dejneka et al. [76] revealed that transparent magnetic glass-ceramics can be produced by impregnation of PG with ferric nitrate salts and thermal treatment. The resultant glass-ceramic composites contained ferrite nanocrystals that exhibited ferromagnetic and superparamagnetic behavior. Lee et al. [77] studied the optical properties of Ag-glass composites prepared by impregnation of PG with $AgNO_3$ solution followed by reduction and densification at various temperatures. Similarly, Arakcheev et al. [78] obtained a transparent metal-dielectric composite by impregnation of PG with a silver containing precursor and annealing. Mazali et al. [79] reported that nano sized anatase TiO_2 crystals could be formed in the PG and they showed that the growth was not depended on the thermal

treatment time. The nanopores acting as space limitation and Ti-O-Si linkages acting as chemical anchors could be associated with TiO_2 nanocrystal size controlling factors. Anpo et al. [80] studied on the photocatalytic activity of TiO_2 anchored on PG. The anchoring was achieved by the reaction of titanium (IV) chloride with the hydroxyl groups on PG surface. Also, Yazawa et al. [81] indicated that due to its transparency and large SSA, a PG tube supported TiO_2 showed high photocatalytic activity.

In the light of the inspirational studies done earlier by several researchers, the PGs with various pore texturs were produced in the frame of this dissertation studies. The relationship between production parameters and the pore architecture of PGs was researched. In addition, the tribological properties namely friction coefficient and wear rate of PG were investigated. To the best of the author's knowledge, there is no study performed on the tribological properties of PGs. Finally, the limitations of powder TiO_2 based photocatalysis have motivated us to conduct a search on the TiO_2 embedded PGs in wastewater treatment applications. Considering that PG is already used as a solid absorbent [69], TiO_2 embedded PGs are thought to be utilized as promising material in wastewater treatment because of their synergistic effect of both photocatalytic activity and absorbent properties.

CHAPTER 3

EXPERIMENTAL PROCEDURE

3.1   Production of Porous Glass

Reagent grade Na_2CO_3 (Merck), H_3BO_3 (Eti Maden), $Al(OH)_3$ (Eti Alüminyum) and, SiO_2 (Eczacıbaşı) powders were used in appropriate amounts to yield a glass with nominal composition of $55.7SiO_2$-$33.6B_2O_3$-$9.2Na_2O$-$1.5Al_2O_3$ (wt %) by a conventional melt-quenching. First, the powders were mixed in an agate mortar with pestle to produce a homogeneous mixture of ~ 42 g. Then, the batch was put in a 90Pt-10Rh crucible and placed in an electrically heated furnace (atmospheric, PT1700M, China) for melting. The melting process took place at 1300 °C without controlling the atmosphere. The heating rate was 10 °C/min. After keeping the melt at 1300 °C for 2 h, it was quenched in air onto a stainless-steel plate. The resulting glass shards were further crushed and re-melted in the same crucible at 1400 °C for 2 h to ensure the chemical homogeneity and to get a readily castable melt. After that, the melt was cast onto a stainless-steel plate of room temperature (RT) and another steel plate weighing 1 kg (causing an approximate pressure of 0.001 MPa) was placed on the cast (with no additional pressure) to obtain a flat surface while solidification proceeding. The temperature vs time graphs applied to obtain SBG is illustrated in **Figure 3.1**.
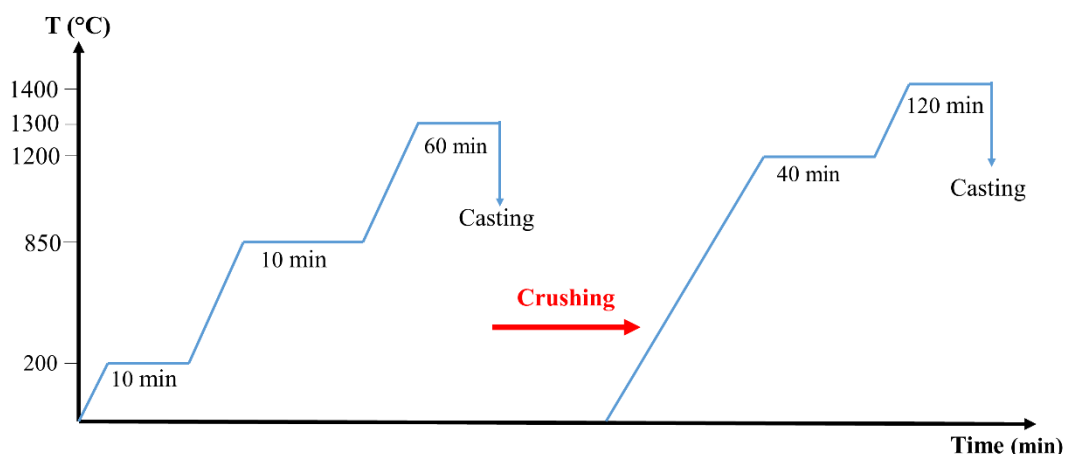
Figure 3.1. The melting process of SBG glass.

In order to provide phase separation, the SBG chunks were heat treated at 475, 500, and 525 °C for 9 h. It is commonly known that the surface of glass specimens are covered with a thin SiO_2 rich layer caused by volatilization of sodium and borate during heat treatment [18]. The unwanted SiO_2 rich layer was removed by mechanical polishing using 3 μm diamond paste finish. The final thickness of the pieces was 2±0.1 mm.

Upon heat treatment the soluble alkali borate phase was removed by immersing the SBG chunks, i.e. phase separated glass pieces, into either 0.5M, 1M, or 3M HCl aqueous solution at 80 °C for 24 h. Acid leaching was performed using 125 mL of acid solution for every 1 g of SBG for all samples. The acid treated glass were then washed with distilled (DI) water and ethanol for several times and finally dried at 90 °C for 3 h in an oven. In order to remove silica clusters (those already dissolved in borate-rich phase) remained in the liquation channels of acid leached glass matrix, an additional alkali treatment was done by using 0.5M NaOH solution for 2 h at room temperature (RT). Also an additional heat treatment i.e. consolidation treatment was applied to PG500M1 at 800 °C for 1 h.

The PGs produced were named based on their heat treatment temperature and HCl molarity as PG500M1, where the number in the middle represent the heat treatment

26

temperature and the number after 'M' stands for the HCl molarity applied. Names of the PGs produced and their production parameters were presented in **Table 3.1**.

Table 3.1. The summary of the glasses investigated.

Glass Name	Heat Treatment Temperature (°C)	HCl Molarity	NaOH Molarity	Consolidation Treatment Temperature (°C) and Time (h)
PG475M0.5	475	0.5	x	x
PG500M0.5	500	0.5	x	x
PG525M0.5	525	0.5	x	x
PG475M1	475	1	x	x
PG500M1	500	1	x	x
PG525M1	525	1	x	x
PG475M3	475	3	x	x
PG500M3	500	3	x	x
PG525M3	525	3	x	x
PG500M1-AL	500	1	0.5	x
PG500M1-HT	500	1	x	800, 1

3.2 TiO$_2$ Crystallization within the Porous Glass

PG500M1, PG500M1-HT, and PG500M1-AL were utilized as a support material for the crystallization of TiO$_2$ crystallites within the porous structure. In order to get convenient specimens for the impregnation process, the PG's to be utilized in TiO$_2$ crystallization hence, in photocatalytic tests were produced with the thickness of 1.5 mm. 1 M Titanium (IV) Isopropoxide (TTIP)/isopropyl alcohol solution was employed as titanium precursor. The PG monoliths more or less the same size and shape were impregnated with precursor solution for 24 h at RT while the solution was continuously mixed with a magnetic stirrer at 900 rpm. Then, it was degassed with ultrasonic for about 1 h to ensure that the precursor solution penetrated into the glass. After the impregnation, PG monoliths were removed from the solution, the

excess solution on the surface of PG was gently wiped by an adsorbent paper. The Ti impregnated PG monoliths were allowed to proceed hydrolysis reaction with water in air (i.e., humidity) for 24 h. After that, they were dried at 100 °C in an oven to remove the solvents. Next, the dried PG monoliths were heat treated at 450 °C for 4 h in open air. Finally, they were cleaned with isopropyl alcohol in ultrasonic cleaner for 30 mins to remove the free TiO_2 crystals that grew on the surface and could not attach to the pores in PG.

Titanium impregnated (TiO_2 embedded) glasses were named by adding "Ti" in front of the code of PG like TiPG500M1. The name Tix2PG500M1 was reserved for PG500M1 exposed to the impregnation and calcination processes twice. A TiO_2 powder, coded as TiPow, was prepared by the same procedure applied to the Ti impregnated PGs for comparison purpose by using the solution remaining left from impregnation stage.

The steps involved in the production of various types of PGs and in the crystallization TiO_2 within the pores of PGs are shown in **Figure 3.2**.
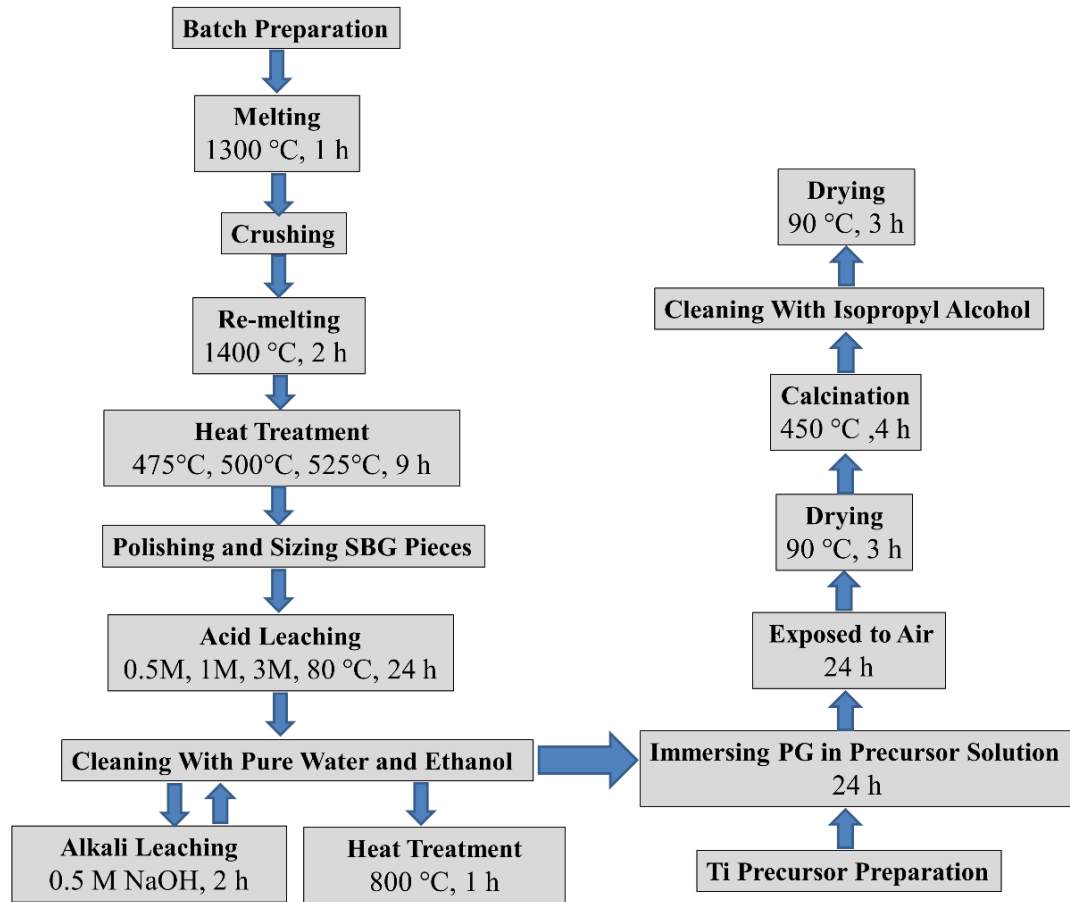
Figure 3.2. The steps in the PG production processes and TiO_2 crystallization within the PG.

3.3   Characterization

3.3.1   Differential Thermal Analysis (DTA) and Thermogravimetric Analysis (TGA)

Glass samples for differential thermal analysis (DTA) and thermogravimetric analysis (TGA) were pulverized in an agate mortar with pestle down to 150 µm (100 mesh). The measurements were carried out in a Pt crucible at a heating rate of 5 °C/min from RT up to 1025 °C under nitrogen/air atmosphere using SII Exstar 7300 unit DTA-TGA unit.

3.3.2 X-Ray Diffraction Analysis (XRD)

SBG and PG samples were analyzed by an X-ray diffractometer (Bruker-AXS, D8 Advance A25) between 10-90° at a scanning rate of 2°/min using CuKα radiation with a wavelength of 1.54056 Å in bulk form before and after heat treatments. To have more accurate XRD patterns of TiPG and TiPow, the scanning rate was set to 0.2°/min. The crystalline phases were identified by using the database of the Joint Committee on Powder Diffraction Standards (JCPDS). The verification of the phase identification was confirmed using Rigaku 4.2 software program.

3.3.3 N_2 Adsorption-Desorption Analysis

Pore characteristics were evaluated by N_2 adsorption desorption using Quantachrome Autosorb-6. Prior to the measurement, the specimen was evacuated at 250 °C for 3 h. The SSA was measured by using Brunauer–Emmett–Teller (BET) equation from the adsorption isotherm. The total pore volume (V_P) was calculated from the amount of gas adsorbed at the relative pressure $P/P_0 = 0.99$. The pore size distributions (PSD) were determined from the desorption branch of the nitrogen sorption isotherm according to the BJH (Barrett, Joyner, Halenda) method, based on the Kelvin equation, which relates the pore size with critical condensation pressure assuming a straight cylindrical pore model.

3.3.4 Mercury Porosimeter Analysis

The Mercury Porosimeter measurements were carried out on a Quantachrome Poremaster 60 instrument up to 33000 psi (227.5 MPa) pressure. The cumulative pore volume at a given pressure represents the total volume of mercury taken up by the sample at that pressure. The pore diameter was calculated by the Washburn equation and assuming a cylindrical pore model.

30

3.3.5 Morphological Analysis and EDS

The microstructure of SBG, PG and TiPG was examined using a scanning electron microscope (FESEM, Nova Nanosem) in combination with Energy Dispersive X-Ray Spectroscopy (EDS) to provide the information of the elemental composition of samples. Before SEM examinations sample surfaces were coated with a thin layer of gold by a sputtering. Operation voltage was changed between 10 to 20 kV, while the spot size was adjusted 3.5 or 5.5 during imaging depending on the sample conditions.

3.3.6 FTIR Analysis

The Fourier transform infrared (FTIR) transmission spectra of SBG, PG, TiPG and TiPow was measured by Perkin Elmer Frontier instrument equipped with ATR (Pike Gladi) apparatus in the range of 400–4000 cm^{-1} with a resolution of 1 cm^{-1}. A linear baseline was fitted to the IR spectra then normalized to signal intensity.

3.4 Property Measurements

3.4.1 Density

The bulk density (ρ) and open porosity (V_O) of the glasses were measured by the Archimedes method in accordance with ASTM C373-18 standard by using **Eq.6** and **Eq.7**, respectively.

$$\rho = \frac{W_D}{W_w\text{-}W_s} \times \rho_{water} \qquad (6)$$

$$V_o = \frac{W_w\text{-}W_D}{W_w\text{-}W_s} \qquad (7)$$

Where ρ_{water} is the density of water at 25 °C (0.99 g/cm^3). W_D, W_W, and W_S are dry, wet, and suspended weight of the specimen, respectively [82]. The bulk density and

open porosity values were determined as the arithmetic mean of the six measurements of three samples tested for each glass.

3.4.2   Hardness

The Vickers hardness (H_V) values were determined by taking the average of 15 indents from a microhardness tester (Shimadzu, HSV-20) at 500 g load for 10 s. H_V values were calculated by means of **Eq.8.**

$$H_V = \frac{1.8544N}{d^2}$$

(8)

Where d stands for diagonal length of the indentation imprint in m, N is the applied force in N and Hv is the microhardness in MPa. The indentation imprints were subsequently analyzed using an optical microscope (Huvitz HDS-5800, Republic of Korea).

3.4.3   Tribological Measuraments

Tribological tests of different PGs were performed using a pin-on-disc tribometer (CSM Instruments, USA) in accordance with ASTM G99-95A standard. Loads of 1 N and 5 N were applied at 100 Hz rate at 0.03 m/s linear speed at ambient atmosphere. The sliding distance (L) was 60 m and application radius was 0.003 m for each test. A high purity zirconia ball of 0.0025 m radius was employed as a pin material and no significant pin wear was observed after the test. Surface profile of the worn specimens was measured using a stylus profilometer (Mitutoyo Surftest SJ-400, USA) to determine the worn track area. The wear rate was calculated by means of **Eq. 9.**

$$W = \frac{V}{P.L}$$

(9)

Where; W is the wear rate in $mm^3/N.m$, V is the calculated volume loss in mm^3, P is the normal load in N and L is the sliding distance in m. The W values were calculated by the arithmetic mean of the five measurements for each sample.

3.4.4   Transmittance Measurements

The transmission spectra of SBG, and selected PGs and TiPGs were measured on a UV-Vis spectrometer (Scinco S-3100, Korea) in the wavelength range of 250–850 nm with a step of 1 nm.

3.4.5   Band Gap Measurements

The optical band gap energy (Eg) values, which is the energy corresponding to electron excitation from valence band to conduction band, of the Ti impregnated samples were measured using UV-Vis diffuse reflectance spectra. The reflectance (R) data was converted to the F(R) values which is proportional to the extinction coefficient (α) using the Kubelka–Munk equation

$$F(R) = (1-R^2) / 2R \tag{10}$$

than $(F(R)h\nu)^{1/2}$ as y axis against hν (eV) as x axis graph was plotted and Eg for indirect allowed transition was calculated by extrapolating the midsection of the graph to the x axis [83].

3.4.6   Methylene Blue Decolorization Tests

Methyl Blue (MB) adsorption and photocatalytic properties of selected PGs and TiPGs were investigated by MB concentration change during the experiments which were performed using 30 mL MB/DI water solution with concentration of 10 ppm in a 250 mL glass container. Three pieces of TiPG or PG chunks with a thickness of 1.5 mm and a total weight of 0.3 g were horizontally placed into glass container. The

MB concentration change was defined as the absorbance of the solution at a wavelength of 664 nm. For the measurements, 3 mL of the solution was periodically taken and analyzed by a UV-Vis spectrometer (Scinco S-3100) than added back to the glass container. All the tests were carried out under continuous stirring (~500 rpm) using a magnetic stirrer in a homemade enclosed box, which provides a fully dark environment.

For the photocatalytic degradation measurements of TiPG samples, the MB solution irradiated by a 100W UV lamp (UVP, Blak-Ray, CA, USA) with a wavelength at 365 nm. The removal efficiency (RE) of the glasses was calculated using the formula:

$$RE = \frac{(C_0 - C_n)}{C_0} \times 100 \tag{11}$$

Where; C_0 and C_n are the concentrations of MB at initial and different irradiation times, respectively.

CHAPTER 4

RESULTS AND DISCUSSION: PRODUCTION OF POROUS GLASS

4.1   General Remarks

The pore architecture of PG is a complex phenomenon that varies with many parameters in the production steps. Although the most effective of these parameters are glass composition, heat treatment temperature and acid leaching concentration, there are other parameters such as heat treatment time, acid leaching temperature and the ratio of leaching solution volume to glass mass. By keeping all other parameters constant, different sets of PGs in terms of pore volume and pore size distribution were produced using different heat treatment temperatures (475, 500, 525 °C) and acid leaching concentrations (0.5, 1, 3 M), to the observe the effect of these parameters on the pore architecture of PGs produced. In this part of the thesis, the results of the PGs produced with various pore architectures and their physical, structural, and optical properties were presented and discussed.

The appearance of the representative pieces for the PGs produced, as shown in **Figure 4.1,** revealed that all PGs were colorless and transparent to the naked eye (in visible region). No macroscopic crack formation in PG500M1 was detected but, PG525M3 completely disintegrated. The other PGs showed surface cracks. It is obvious that the stress development in PG is very significant and causes cracking during either the acid leaching process or drying the acid leached glass. The glass PG500M1, which did not crack in repeated productions, was chosen for further investigations.

Figure 4.1. The photographs of SBG and PGs produced.

4.2   Differential Thermal Analysis (DTA) and Thermogravimetric Analysis (TGA)

The DTA/TG thermograms of PG500M1 are shown in **Figure 4.2**. The weight loss about 11% was interpreted as the removal of physically and chemically bond water in PG500M1. The loss of mass ~6% up to 200 °C was interpreted as the removal of physisorbed water molecules within the pores. Increasing the temperature above 200 °C led the departure of the chemisorbed water by condensation of two hydroxyl groups into a siloxane bridge (Si-OH + Si-OH = Si-O-Si + H_2O), so called dehydroxylation [68,84–86].

The first endothermic peak in DTA curve at temperature of 660 °C is attributed to the glass transition temperature (Tg) and the exothermic peak at 965 °C corresponds to the crystallization temperature (Tc) of the glass. The Tg of SBGs with similar chemical compositions have been reported in the range of 480-510 °C in the literature [25,53,70]. In addition, studies carried out with differential scanning calorimetry asserted that the two phases contained in SBG lead to two different Tg observations, while the alkali-borate phase had low Tg (445 to 560 °C) and the silicate phase had high Tg (520 to 740 °C) [46,61]. Considering that, PG500M1 was produced by removing the low Tg alkali-borate phase from SBG with acid leaching, the Tg value of PG500M1 is consistent with the values reported in literature.
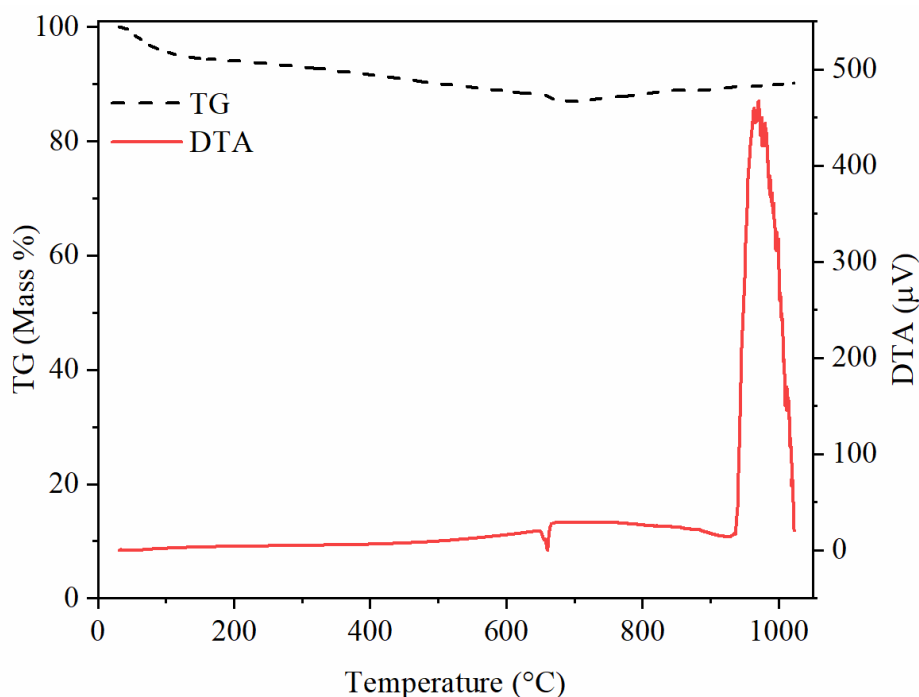
Figure 4.2. DTA/TG curve of PG500M1.

4.3   X-Ray Diffraction Analysis (XRD)

Prior to the XRD analysis, the surfaces of the bulk glass pieces were polished using 1000 grid SiC grinding paper to remove the silica rich layer formed after casting since devitrification mostly initiates from the surfaces, due to nucleation sites on

surface, if volume nucleation is not promoted [87]. Polishing was applied also to make the surfaces of the samples parallel.

Figure 4.3 (a) shows the XRD patterns of the SBGs heat treated for 9 h at temperatures from 500 °C up to 600 °C. The XRD patterns were taken from the representative samples in the bulk form. The patterns indicated no XRD peaks corresponding to certain crystallographic planes in the crystal structure. Instead, noisy background and a halo present in between 15-30° (2θ) in all SBGs, an evidence of short-range order, confirmed the completely amorphous nature of the samples. A broad peak barely noticed at 2θ of ~45° associated with the heterogeneous microstructure generated by spinodal decomposition [67]. The results suggest that the amorphous silica-silicate related glass is produced in as cast piece and it maintains the amorphous state when heat treated at temperatures up to 600 °C. The XRD patterns of the SBGs heat treated at temperatures of 625 °C and 650 °C are shown in **Figure 4.3 (b).** The XRD peak at 2θ of 22.2° begins to become apparent at 625 °C. It is obvious that crystalline phase(s) developed in or at least on the surface of SBG after heat treatment at 625 °C for 9 h.

As the heat treatment temperature increases to 650 °C, some other peaks become distinct and noisy background together with the halo diminishes, implying full crystallization of the sample. This pattern was compared to the standard card of the crystoballite phase (JCPDS No. 39-1425) and diffraction peaks at 2θ of 21.8°, 28.2°, 31.2°, 35.9°, 44.5° and, 48.2° were assigned to (101), (111), (102), (200), (202), and (212) of crystoballite. When the SBG heat treated at 625 °C in bulk form is pulverized down to 150 μm before the XRD analysis, the peaks belonging to crystoballite disappeared, indicating that the crystallization initiated at the surface, but, did not took place in the entire volume. Similar reports were published previously by other researchers [88,89].
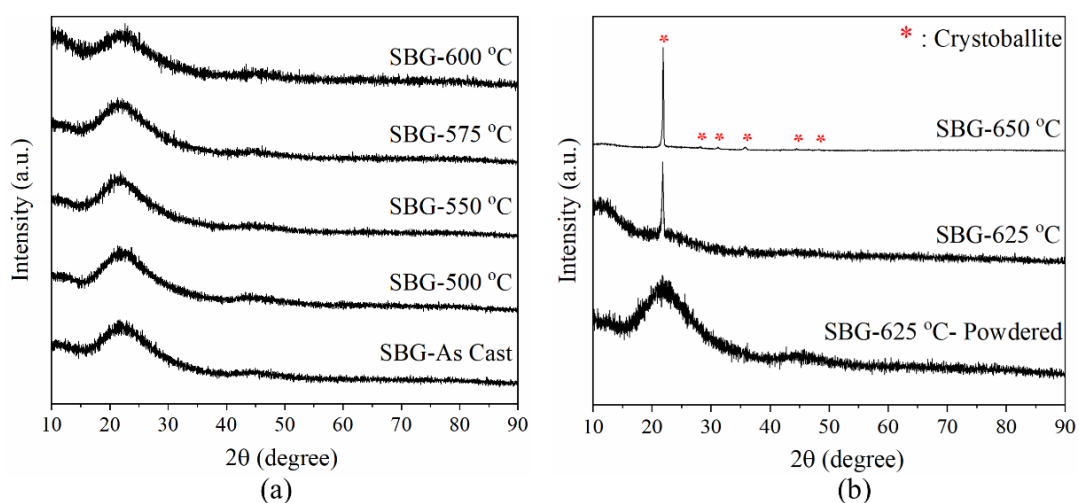
Figure 4.3. XRD patterns of SBG heat treated at various temperatures (a) up to 600 °C and (b) 625 and 650 °C for 9 h.

Figure 4.4 shows the XRD patterns of PG500M1, PG500M1-HT, and PG500M1-AL. The XRD patterns suggest that all PGs were in amorphous state. The fingerprint of spinodal decomposition at 2θ of ~45° detected in SBG500, diminished upon acid leaching, akin to the results reported by Lee et al. [90].
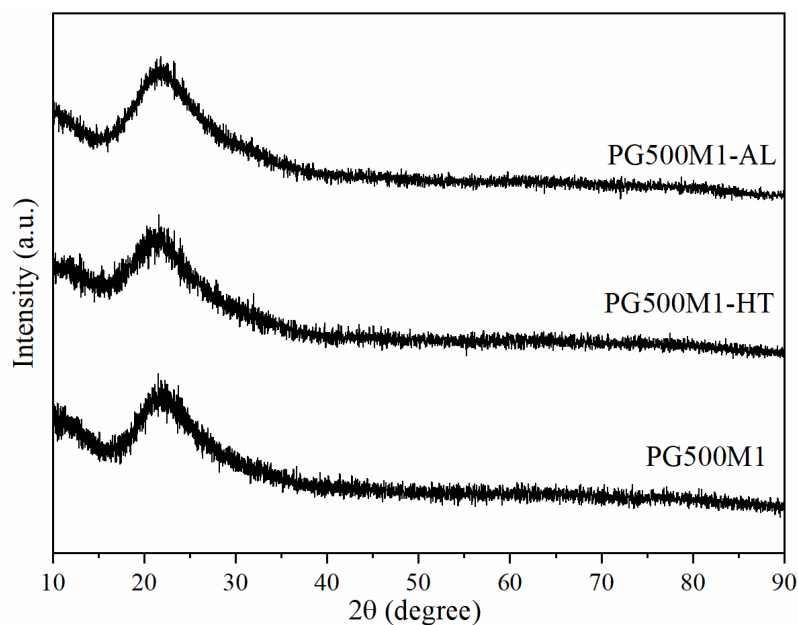
Figure 4.4. XRD patterns of selected PGs.

4.4   N₂ Adsorption-Desorption Analysis

Figures 4.5 and **4.6** indicate the N₂ adsorption-desorption isotherms of the selected PGs. The pore structure determines the isotherm shape and all the PGs show a type IVa isotherm according to the IUPAC classifications, while almost no N₂ adsorption was observed for non-porous SBG500. The capillary condensation is accompanied by hysteresis and PGs exhibit combination of H2a and H2b type of hysteresis which is generally related with pore-blocking/percolation in a narrow range of pore necks or cavitation-induced evaporation [91].
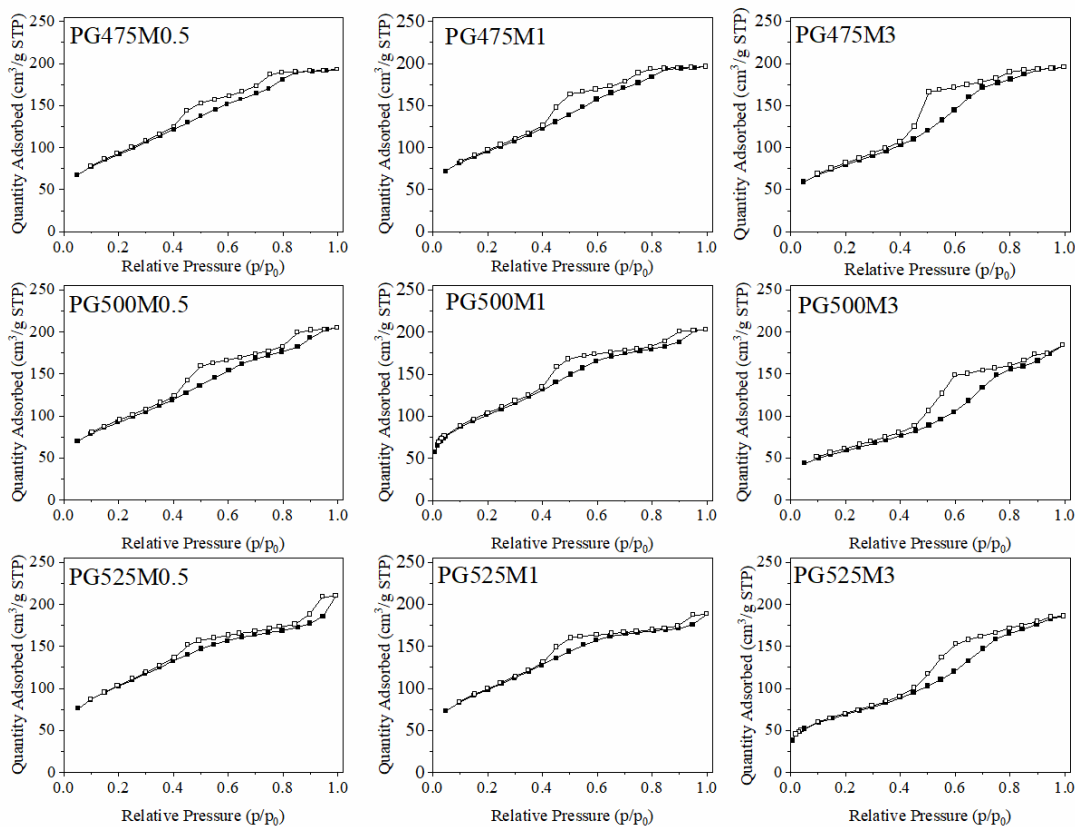
Figure 4.5. N₂ adsorption-desorption isotherm of the selected PGs.
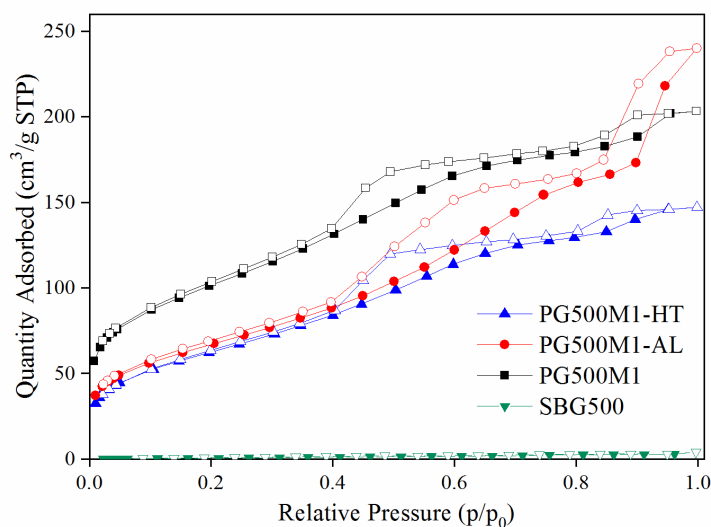
Figure 4.6. N$_2$ adsorption-desorption isotherm of SBG500, PG500M1, PG500M1-AL, and PG500M1-HT.

The PSD curves in **Figures 4.7** and **4.8** illustrate that the PGs prepared have different size of pores, implying that the pores developed hierarchically. The pores concentrated in the range of 3–5 nm (primary pores) are associated with the inter-particle spaces in between the channel walls and silica clusters (themselves as well). Indeed, the relatively larger mesopores evolved in a broader range from 7 to 30 nm are due to the so called liquation channels (secondary pores) [22,47,92].
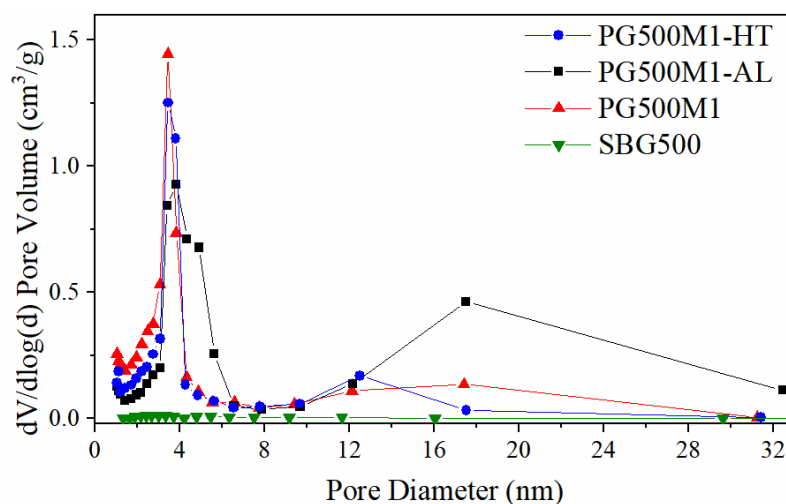
Figure 4.7. Pore size distribution curves of SBG500, PG500M1, PG500M1-AL, and PG500M1-HT.

41
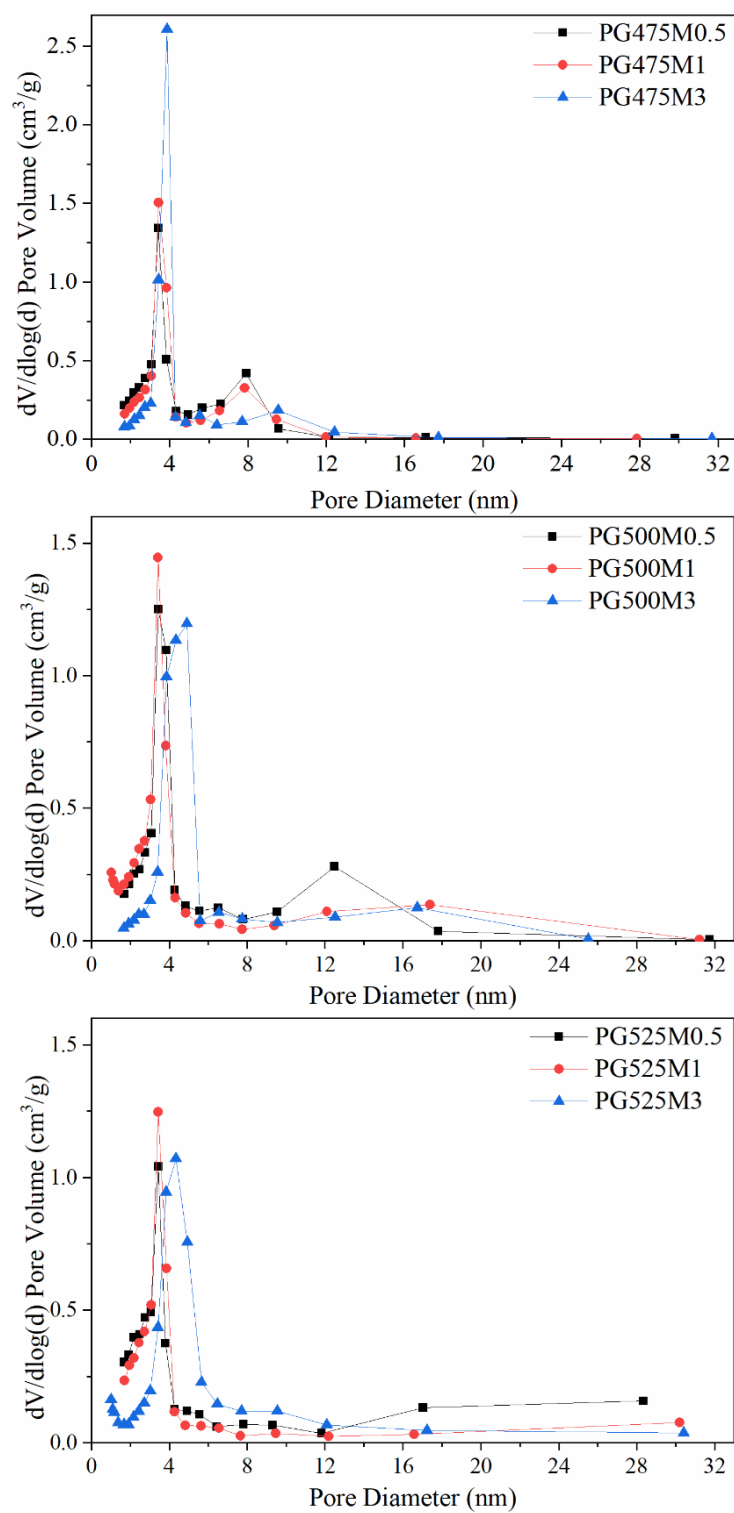
Figure 4.8. Pore size distribution curves of the selected PGs with various acid leaching molarities.

Increasing the acid molarity from 0.5 M to 1 M did not have a significant effect on the primary pores but, when the acid molarity was increased to 3 M, the first peak slightly shifted to a higher pore size. This change in primary pore size was due to the agglomeration of small silica precipitates hence development of larger precipitates which leads to the formation of larger primary pores [22]. Also increasing the acid molarity caused slightly enlarged secondary pores and the second peak on PSD curve broadened. The more concentrated acidic solution could dissolve the alkali richer phase more hence enlarges liquation channels. The broadening of the peaks is explained by the agglomeration of silica precipitates and partially closing the liquation channels [47]. Closure of the liquation channels results in the absence of an apparent peak in heat treated samples at 525 °C as shown in **Figure 4.8**. There was no significant effect of heat treatment temperature on the primary pore size but, had a remarkable effect on the secondary pores. Similar findings were reported previously by other researchers [59]. The volume fraction of the alkali-borate phase increased with increasing heat treatment temperature thus, enlarged the liquation channels. Increasing the heat treatment temperature increased the width of secondary pores and formed a broader pore size distribution in mesopore range [49].

When a comparison is made between pore architectures in PG500M1-HT and PG500M1, it is evident that the primary pore size in PG500M1-HT slightly increased and the secondary pore size decreased as shown in **Figure 4.7**. It is assumed that the silica clusters partially sintered and the liquation channel narrowed due to partial sintering of the matrix by consolidation treatment at 800 °C for 1 h [26,64]. Both primary and secondary pore size as increased in PG500M1-AL as compared to PG500M1. This was expected since alkali treatment causes the silica clusters to dissolve in the alkali solution together with probable partial dissolution of the silica skeleton. The primary pore size increased but, primary pores did not totally vanish. This situation was interpreted as either the silica clusters cannot completely remove from PG500M1 or new small pores formed during the dissolution of the silica skeleton. The increment in the secondary pore size supports the hypothesis that the

silica skeleton partially dissolved during the alkali treatment as also mentioned by Lyubavin et al. [93].

The SSA and V_P values as determined from N_2 adsorption-desorption analysis for the selected PGs were listed in **Table 4.1**. For the PGs heat treated at 475 °C and 500 °C, SSA first increased with increasing acid molarity then, drastically decreased as the molarity reached to 3 M. The SSA of the PG heat treated at 525 °C decreased with increasing acid molarity from 0.5 M to 1 M. The observations reveal that the SSA of PG mostly depends on the concentration of dissolved silica in the acid solution in the liquation channels. At lower heat treatment temperatures, the dissolved silica concentration is low thus, the increase in acid molarity results in a slight increase in SSA by forming more silica precipitates. When the acid molarity increased to 3 M, these precipitates started to aggregate and formed bigger precipitates leading to a decrease in SSA.

At higher heat treatment temperatures than 525 °C, the dissolved silica concentration was high enough to form bigger silica precipitates even by a small increase in the acid molarity. The SSA and V_P of PG525M3 were higher than those of PG500M3. However, it should be taken into consideration that this PG was completely disintegrated during acid leaching process (see **Figure 4.1**). The disintegration probably initiated the removal of the dissolved silica from the liquation channels easily during the acid leaching process. The dissolved silica concentration could not reach higher levels and the precipitation was lesser than that was noticed in bulk PGs. It should be stated that, the utilization of powdered samples in N_2 sorption test provides higher SSA as compared to the bulk samples. The graph in **Figure 4.9** shows the effect of acid molarity of the leaching solution and heat treatment temperature on SSA for the selected PGs.

Table 4.1 The specific surface area and total pore volume of PGs.

Sample Name	Specific surface area (m^2/g)	Total pore volume (cm^3/g)
PG475M0.5	331.4	0.298
PG500M0.5	327.7	0.316
PG525M0.5	367.1	0.324
PG475M1	335.2	0.303
PG500M1	358.0	0.314
PG525M1	350.6	0.291
PG475M3	280.9	0.302
PG500M3	207.8	0.284
PG525M3	243.0	0.287
PG500M1-AL	241.2	0.370
PG500M1-HT	228.4	0.227
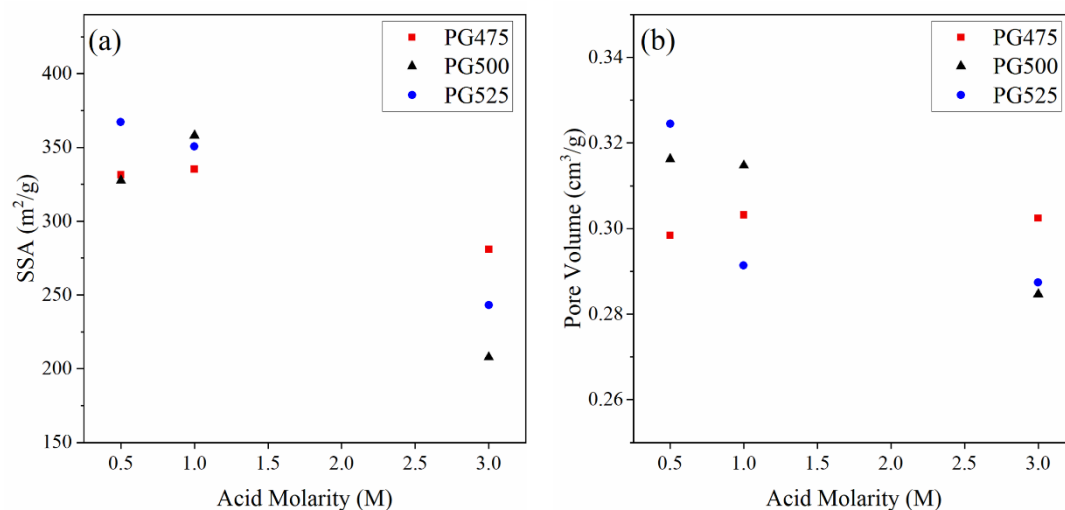
Figure 4.9. The effect of acid molarity and heat treatment temperature on (a) spesific surface area and (b) total pore volume.

PG525M0.5 had the highest V_P indicating that it possessed large liquation channels and small sized silica precipitates in these channels. The V_P of PG500M0.5 was

greater than that of PG475M0.5 though the SSA of both PGs was almost equal. This behavior suggests that the width of liquation channels increases with increasing heat treatment temperature. Although PG500M0.5 had larger V_P, the bigger silica precipitates formed in liquation channels of PG500M0.5 caused the SSA to become almost equal with PG475M0.5.

An increase in the acid molarity, drastically decreased the V_P of the PG heat treated at 525 °C. The decrease in V_P suggest that, as a result of the high dissolved silica concentration, even a small increase of acid concentration leads to the formation of bigger precipitates that can block liquation channels. For the PGs heat treated at 475 °C, V_P first slightly increased with increasing acid molarity because the more concentrated acidic solution can dissolve more alkali-borate phase and enlarge liquation channels. A further increase in acid molarity did not cause a significant change in V_P. At this point it can be said that leaching conditions reached the maximum volume of alkali-borate phase that can be dissolved.

Related with the findings about pore size alteration, the V_P of PG500M1-AL increased while SSA decreased as compared to PG500M1 due to the removal of silica clusters and enlargement of liquation channels. Also the SSA and V_P of PG500M1-HT decreased with the compaction of silica clusters and shrinkage of the liquation channels.

The weight and nominal dimensions of PGs were measured using an electronic balance (accuracy of 0.1 mg) and an electronic caliper (accuracy of 0.01 mm), respectively, before and after different treatments, i.e., heat and leaching treatments. SBG lost weight by ~40% after acid leaching. No significant dimensional change was noticed. The weight of PG500M1 was ~ 5.7% lesser after heat treatment. The decrease in weight was attributed to the removal of water in the porous structure and probably dehydroxylation, i.e. removal of -OH groups that were created during acid leaching on the porous network [24,94]. Additionally, a ~4.1% linear shrinkage was recognized as a result of the heat treatment. After the alkali treatment, the weight of PG500M1 decreased by ~25%. This decrease may not be entirely due to the removal

of the silica precipitates since a thin layer is peeled off from the surface during drying.

4.5   Mercury Porosimeter Analysis

PSD curves of PG500M1-AL, PG525M1, and PG500M1 as traced by a mercury porosimeter are shown in **Figure 4.10**. Mercury porosimeter analysis was performed to observe larger pores that could not be detected with N_2 adsorption-desorption analysis. The results revealed that there was no macro pore formation in PGs.

The maximum observed pore size of PG525M1 was larger than that of PG500M1, which indicates that the incresement of heat treatment temperature enlarged the liquation channels. In addition, the pore size of PG500M1-AL was increased up to 30 nm as a result of the alkali treatment due to the removal of silica clusters together with the partial erosion of the silica skeleton as a result of alkali treatment. The findings agree with those gathered by the N_2 sorption analysis.
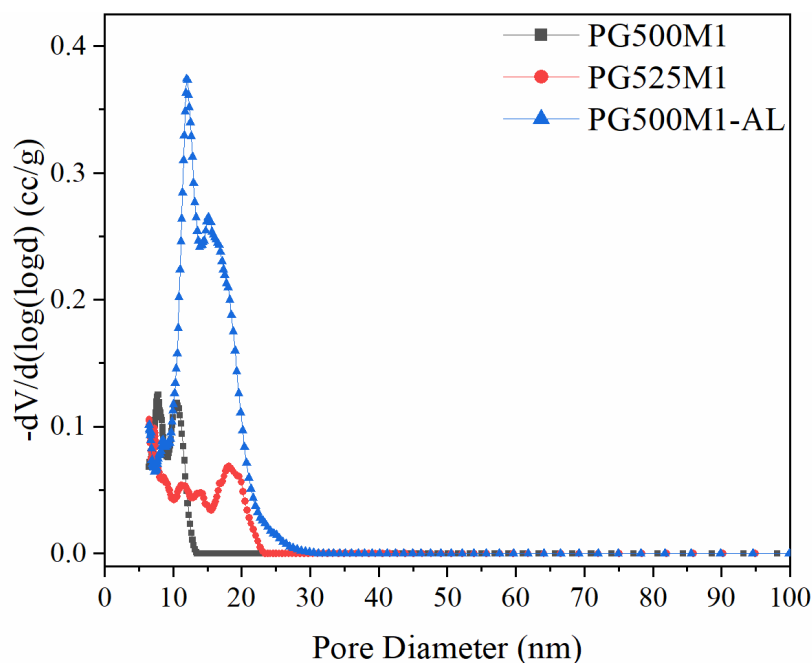
Figure 4.10. The pore size distribution curves of PG500M1-AL, PG525M1, and PG500M1 determined by mercury porosimeter.

4.6   Morphological Analysis

The representative SEM images taken from the surfaces of SBG500 and selected PGs are shown in **Figure 4.11**. It is evident that the characteristic "worm-like" porous structure seemed in all PGs. The worm-like structure becomes more visible with increasing heat treatment temperature. In the SEM images, the liquation channels, previously defined as the secondary pores, were better distinguishable. It is noted that the liquation channels enlarge with increasing heat treatment temperature, confirming the findings of the N_2 sorption analysis. The silica skeleton of the alkali leached PG deformed and the pores became bigger. However, the pores in PG500M1-HT somewhat contracted.
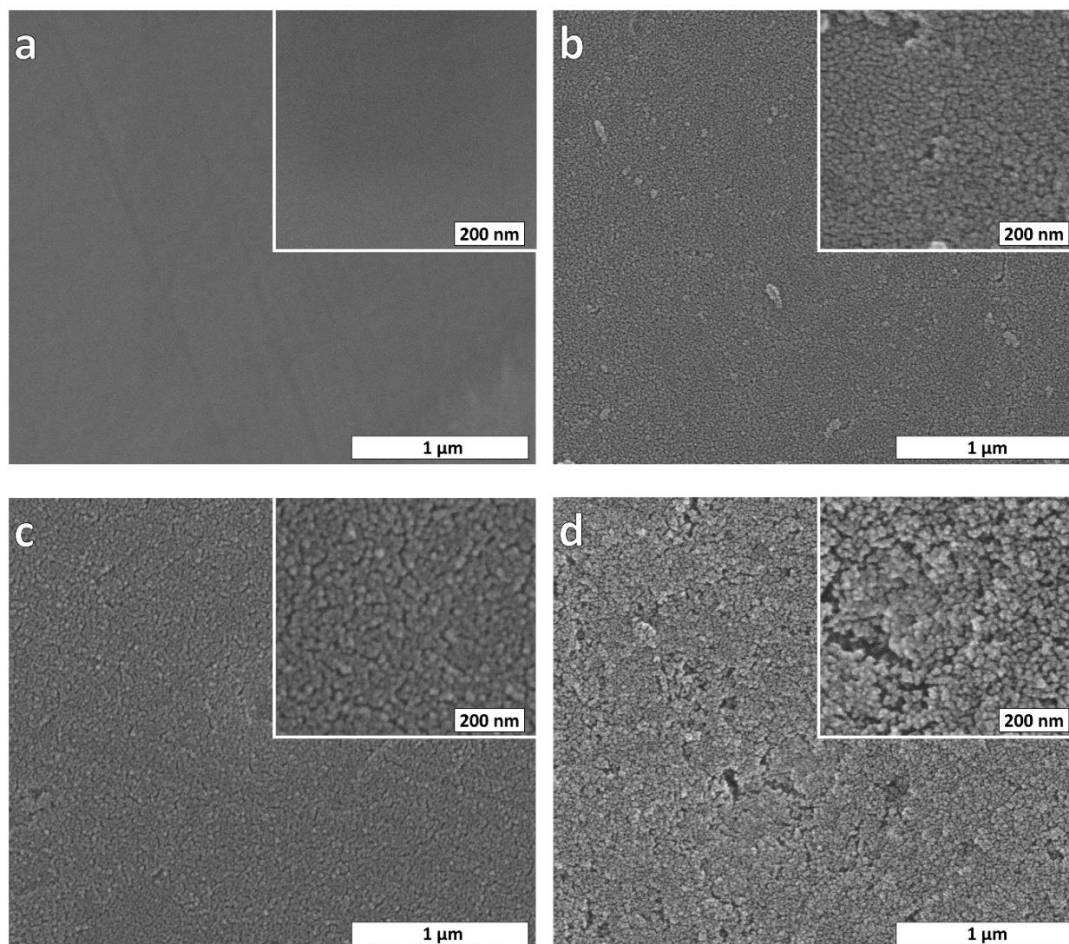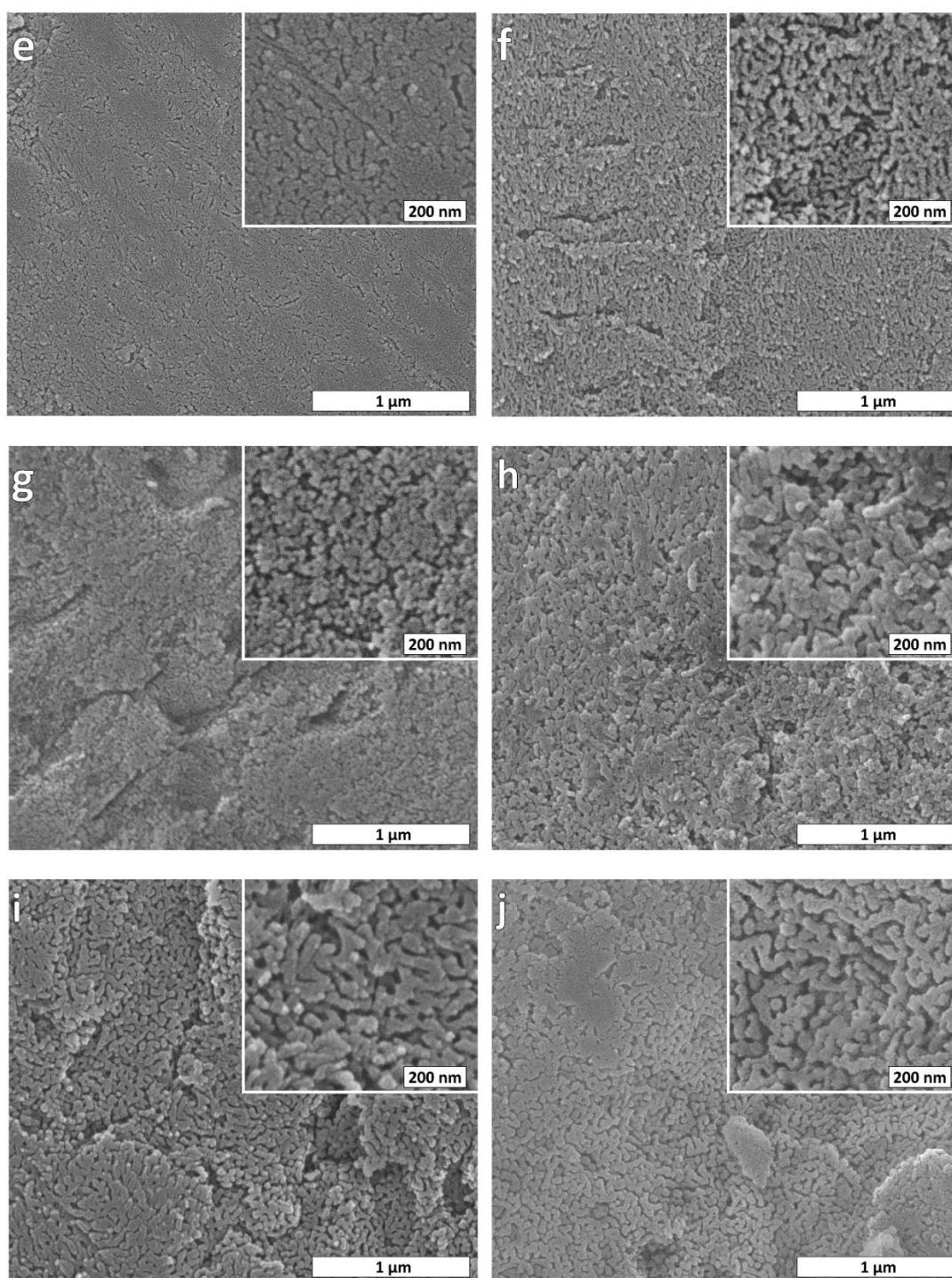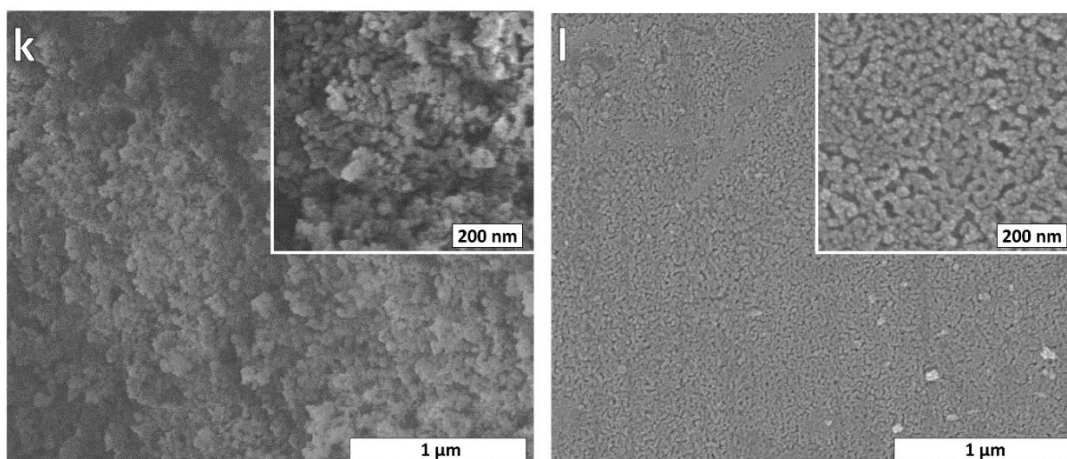
Figure 4.11. SEM images taken from the surface of (a) SBG500, (b) PG475M0.5, (c) PG475M1, (d) PG475M3, (e) PG500M0.5, (f) PG500M1, (g) PG500M3, (h) PG525M0.5, (i) PG525M1, (j) PG525M3, (k) PG500M1-AL, and (l) PG500M1-HT. All images were taken at 100,000X (inlets at 200.000X).

4.7   FTIR Analysis

The FTIR spectra of SBG500 and PG500M1 are shown in **Figure 4.12**. The infrared bands are mainly related to silicate and borate groups and the broad bands arises from the overlapping the various vibration modes of these groups. Only qualitative information can be obtained by comparing these FTIR spectra. It is extremely difficult to identify the peaks in the FTIR spectrum due to the variety of bonds in the glass network and definitive identifications can be made by comparing the spectrum of the glasses with different chemical compositions.

The peaks located at ~450, ~800, and ~1080 cm^{-1} are assigned to Si–O–Si bonds in silicates with three-dimensional network structure or in vitreous SiO_2 [89,95–99] while those at ~920 and ~670 cm^{-1} (with shoulder at ~695 cm^{-1}) correspond to Si-O-B bonds [95,97,100]. Also many bands on the spectra arise from the vibration of B-O bonds. For example, the B-O stretching vibration bands at ~1370 and ~1280 cm^{-1} are related to BO_3 units [95,96,101,102] whereas, those at ~880 and ~980 cm^{-1} are related to BO_4 units [98,103,104].

The FTIR spectrum of SBG500 have wide band regions formed by overlapping vibrations of B-O, Si-O, and Si-O-B bonds between 600-1200 cm^{-1}. After acid leaching, peaks associated with B-O and Si-O-B bonds either decreased in intensity or disappeared completely. In addition, the intensity of the bands assigned to Si-O-Si bonds increased, indicating that the alkali-borate phase formed as a result of phase separation was removed by acid leaching and that the remaining porous structure mostly consisted of silica. The FTIR spectrum of PG500M1 is highly compatible with that previously reported by several researchers [22,100].
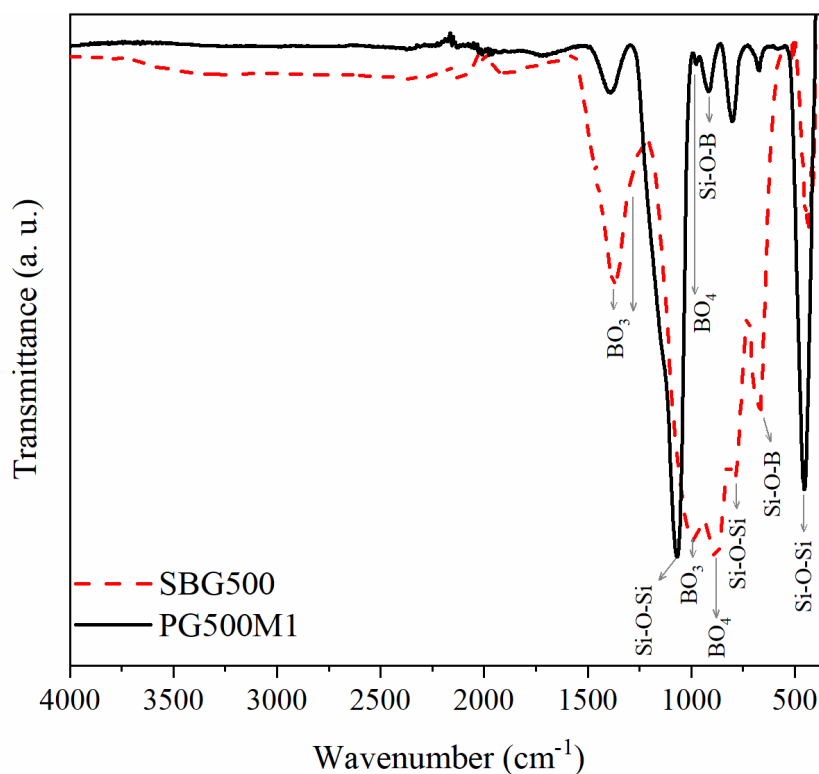
Figure 4.12. FTIR spectra of SBG500 and PG500M1.

4.8 Optical Transmittance

Figure 4.13 represents the transmittance spectra of SBG500, PG500M1, PG500M1-HT, and PG500M1-AL. The optical property of a PG is a quite complicated issue

51

due to its complex structure that has several substances (silica network, pores and silica precipitates) of different refractive indices. Factors such as size and volume of the liquation channels, size, amount and packing density of the silica clusters in these channels affect the transparency of the glass [105–107]. The pore diameter of PG500M1, PG500M1-AL, and PG500M1-HT is so small (up to ~22 nm) compared to the wavelength of the incident light (400 to 800 nm). Consequently, they act as Rayleigh scatterers.

The visible region transparency of SBG500 decreased from ~85% to ~75% as a result of acid leaching process resulting in the formation of porosity. Previous studies reported that turbidity and light transmittance decrease with increasing pore size, i.e. the size of scatterer [108]. The distinct decrease in the transparency of PG500M1-AL by ~10% was attributed both to the increase in pore size and to the partial erosion of the silica skeleton by alkali treatment which also caused the formation of micro cracks on the surface and increased the surface roughness. No significant difference was noticed in the visible region transparency of PG500M1 and PG500M1-HT.

Considering the ultraviolet (UV) region of the transmittance spectra, it was noticed that the PGs were transparent in a wider UV region than SBG. The removal of Na_2O from the structure and the elimination of the impurity atoms that cause UV absorption even in small amounts, are thought to be the reasons for the shift of the absorption edge of PG to lower wavelength as compared to SBG. It is known that the phase separation and acid leaching process is one of the valid methods to obtain UV transparent glass [109,110].
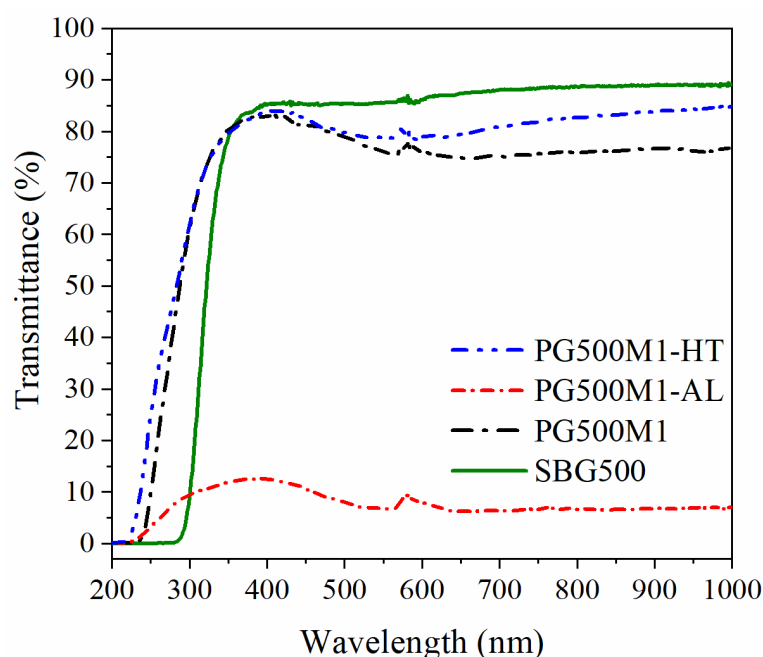
Figure 4.13. The transmittance spectra of SBG500, PG500M1, PG500M1-HT, and PG500M1-AL.

4.9 Density

The bulk density and volume of open pores of the selected PGs were compared with each other as shown in **Figure 4.14**. The error bars in the graph indicates standard deviation from the arithmetic mean values. The values are in good agreement with those previously reported by other researchers for the glasses having similar chemical composition and exposed to similar treatments i.e., heat and leaching treatments [2,10,25,28]. The density of PG500M1-AL is less than that of PG500M1 but, that of PG500M1-HT is greater than that of PG500M1. These findings suggest that the acid leaching resulted in a decrease in density but, heat treatment caused a densification in the porous structure. The open pore volume increased after acid leaching process but, decreased after heat treatment. As expected, the open pore volume increased and bulk density decreased with alkali leaching process.

53
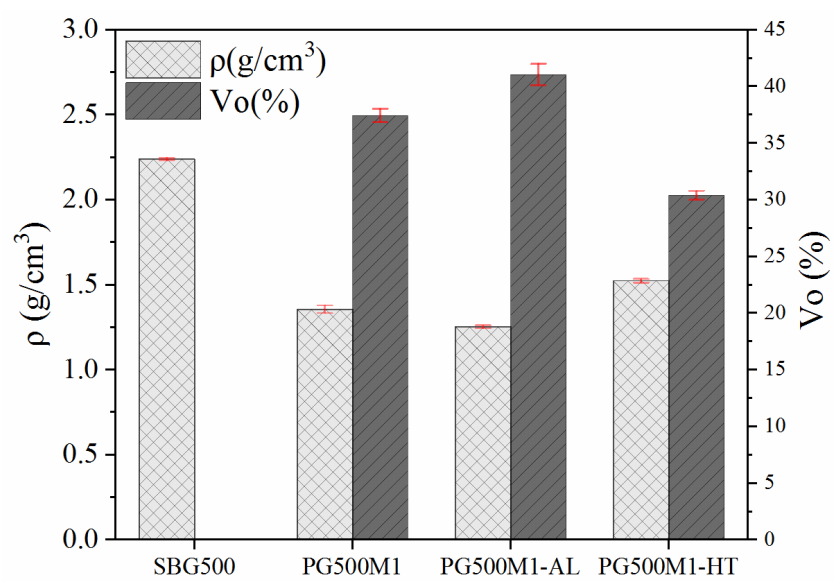
Figure 4.14. The bulk density and open porosity of SBG500, PG500M1, PG500M1-AL, and PG500M1-HT.

CHAPTER 5

RESULTS AND DISCUSSION: TRIBOLOGICAL PROPERTIES OF POROUS GLASS

5.1   General Remarks

In this part of the thesis, the results of the microhardness and tribological properties of SBG and the PGs produced with various pore architectures were presented and discussed. The unique tribological characteristics of PG may extend its application areas where PG will be in contact with different surfaces in relative motion. In recent years, porous bearings have attracted research interests, where pores act as a lubricant reservoir to provide hydrodynamic lubrication so that the systems do not require an external lubricant supply. The wear rate and friction coefficient of PGs with different pore architectures were determined using a pin-on-disc tribometer. Microhardness of PGs was measured and the effects of alkali leaching and thermal treatment on microhardness were discussed.

5.2   Hardness

The optical microscopy images of indentation imprints taken from the Vickers hardness of SBG500, PG500M1, PG500M1-AL, and PG500M1-HT are shown in **Figure 5.1**. The radial and lateral secondary cracks in **Figure 5.1 (a)** are clear evidences for the typical anomalous behavior of the borosilicate glass [111]. The presence of interconnected pores deflects the microcracks causing crack branching and blunting. Therefore, the characteristic secondary cracks observed in SBG500 indentation imprints were not seen in PGs.
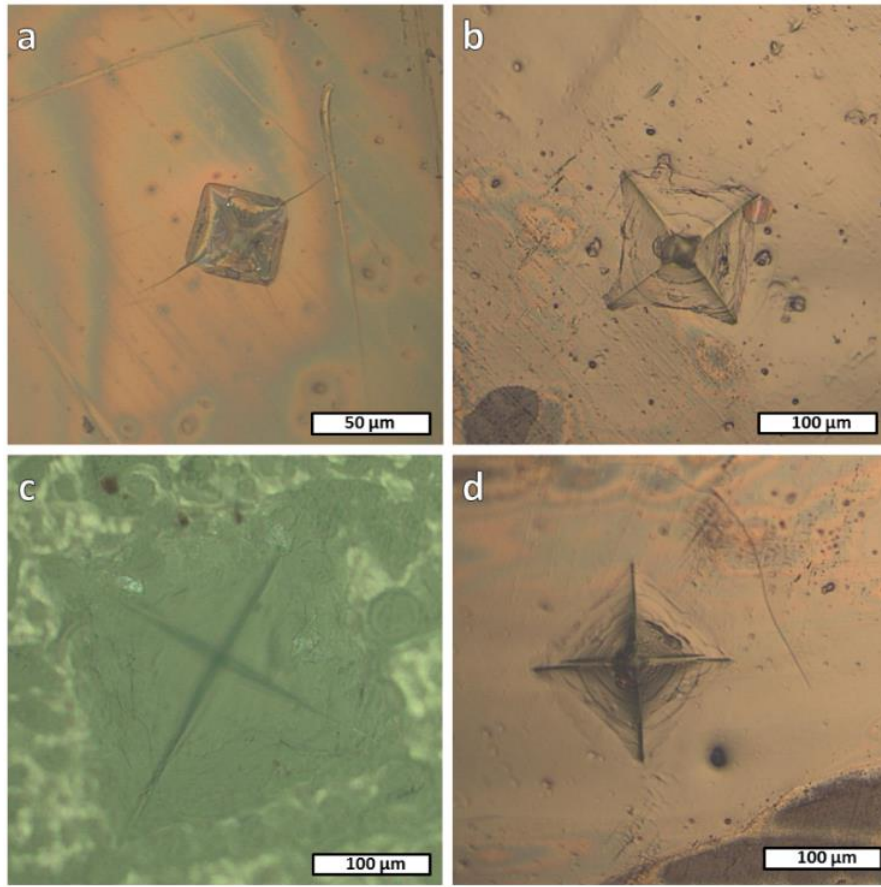
Figure 5.1. Optical images of indentation marks for (a) SBG500, (b) PG500M1, (c) PG500M1-AL, and (d) PG500M1-HT.

The Vickers hardness values of SBG500, PG500M1, PG500M1-AL, and PG500M1-HT are listed in **Table 5.1**. The microhardness of these PGs was compared with each other in **Figure 5.2**. The error bars in graphs and the plus and minus values next to the data indicate standard deviation from the arithmetic mean. The microhardness of PG500M1 is considerably lower than that of SBG500. The decrease in hardness may be attributed to two reasons. First, the thin pore walls cannot withstand the highly localized pressure of the indenter and collapse. Second, the porosity prevents elastic recovery of the indents due to huge free volume in the indented area [112].

56

Table 5.1. Microhardness and tribological properties of SBG500, PG500M1, PG500M1-AL, and PG500M1-HT.

Glass	Hv (MPa)	W ($\times 10^{-4}$mm^3/Nm)		μ mean	
		1 N	5 N	1 N	5 N
SBG500	4296 ± 120	1.06 ± 0.3	2.73 ± 0.8	0.80	0.79
PG500M1	298 ± 20	11.82 ± 1.2	26.02 ± 3.1	0.47	0.50
PG500M1-AL	79 ± 8	90.19 ± 8.1	135.47 ± 19.2	0.41	0.49
PG500M1-HT	332 ± 18	11.91 ± 0.9	23.83 ± 2.2	0.49	0.48
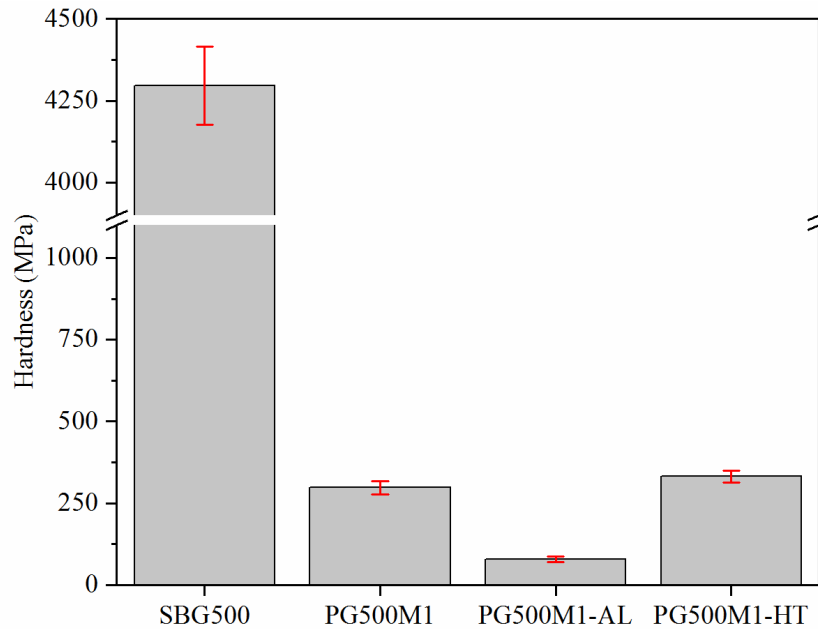
Figure 5.2. The microhardness of SBG500, PG500M1, PG500M1-AL, and PG500M1-HT.

As a result of consolidation heat treatment, a slight enhancement in the microhardness (from 298 to 332 MPa) was recognized due to partial sintering although the specimen was still highly porous and still prone to indentation failure as compared to parent SBG500. Along the same line, Scherer et al. [94] showed that the Young's modulus of PG can be increased by successive heat treatments but, the micro cracks formed during acid leaching can not be healed. For PG500M1-AL, due

to the erosive effect of alkali leaching, the thickness of the pore walls decreased and became weaker against localized pressure. Therefore, a much more dramatic reduction in microhardness (from 298 to 79 MPa) was noted. Supporting the findings of this study, Imakita et al. [113] reported that the hardness of PG samples decreased to one third as a result of alkali leaching.

5.3   Tribological Tests

Friction coefficient (μ) and wear rate (W) values of the glasses are also given in **Table 5.1**. Typically, the W of PG500M1 is about an order of magnitude bigger than SBG500 under the loads of both 1 and 5 N, implying that the thin pore walls are easily damaged during the experiment [114]. When alkali treatment was conducted on PG500M1, as expected, the generation of additional residual etching stresses and more porosity caused an increase in the W of PG500M1-AL compared to that of PG500M1 under both loads. V_P of PG500M1 and PG500M1-AL are 0.314 and 0.370 g/cm^3, respectively. On the other hand, successive heat treatment had no significant effect on W, similar to microhardness results. The Ws of PG500M1 and PG500M1-HT were almost the same under both loads because the pore walls of PG500M1-HT were still as weak as PG500M1.

The variation in μ with sliding distance under loads of 1 and 5 N is shown in **Figure 5.3**. It is clear that the μ of all porous glasses was lower than that of SBG500. This finding is consistent with previous publications which reported that porous and textured surfaces act as a lubricant reservoir and reduce friction coefficient [115,116]. Further experiments are necessary to elucidate these findings. Nonetheless, it should be kept in mind that PG is a good moisture absorber, too. The water molecules bound in the glass skeleton may play a lubricating role [117] and/or fine wear debris may act as a self-lubricating character.
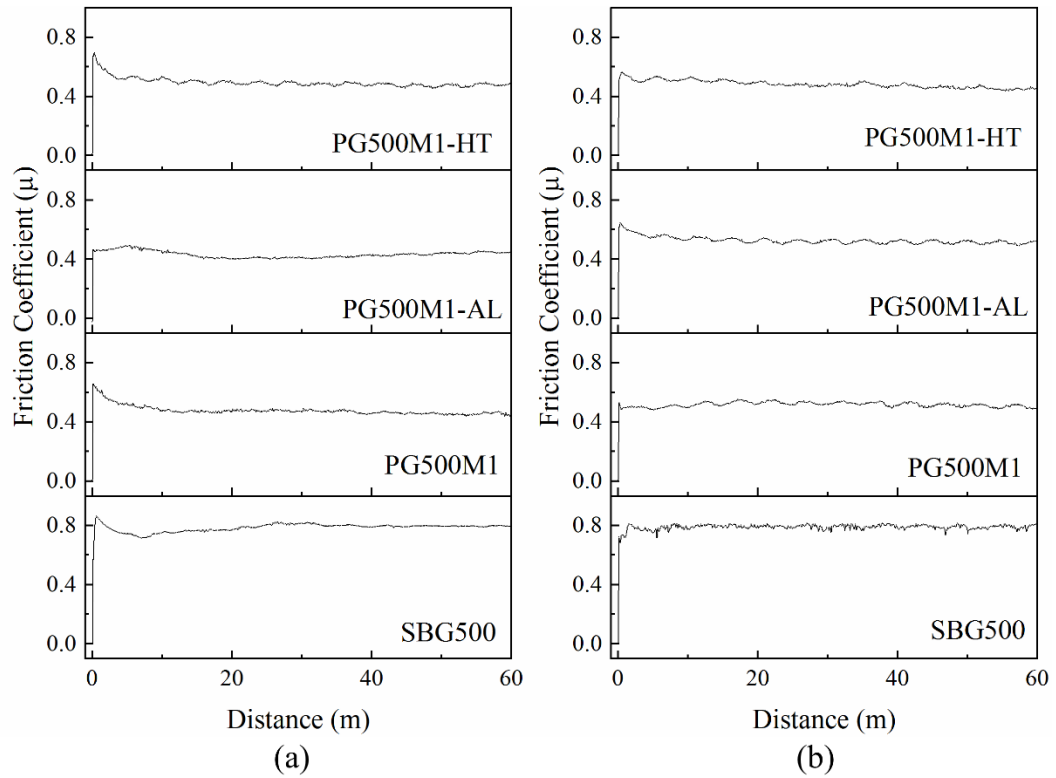
Figure 5.3. Variation in the friction coefficient with sliding distance at a load of (a) 1 N and (b) 5 N.

The optical microscopy images of wear tracks for SBG500, PG500M1, PG500M1-AL, and PG500M1-HT are given in **Figure 5.4**. The debris formed during friction was accumulated and a debris layer formed on the worn surface. The area of these layers was larger in SBG500 as compared to that in PG500M1.

SEM images of wear tracks for SBG500 and PG500M1 are shown in **Figure 5.5**. The images developed at 1 N were taken from the center of the glasses. The magnified images shown in **Figures 5.5 (c)** and **(d)** were taken from the edges to show wear tracks. The white arrows in the SEM images indicate the sliding direction of the counterface. For SBG500, there are cracks spreading from the edge to the outside of the wear track. The size of the cracks ranges from 10 to 40 μm. Instead for PG500M1, such large flaws were not detected in the wear track due probably to the nano-sized pores prevented the crack propagation.

59
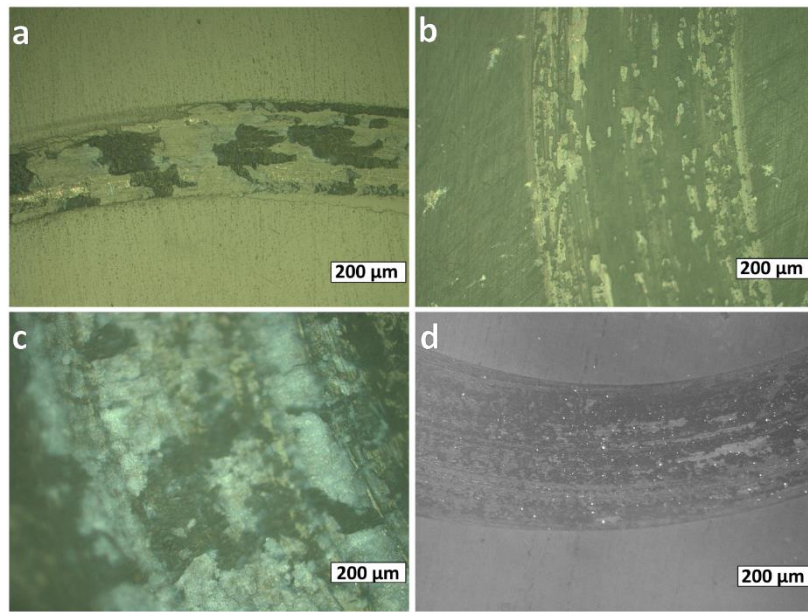
Figure 5.4. Optical microscope images of wear tracks at a load of 1 N (a) SBG500, (b) PG500M1, (c) PG500M1-AL, and (d) PG500M1-HT.
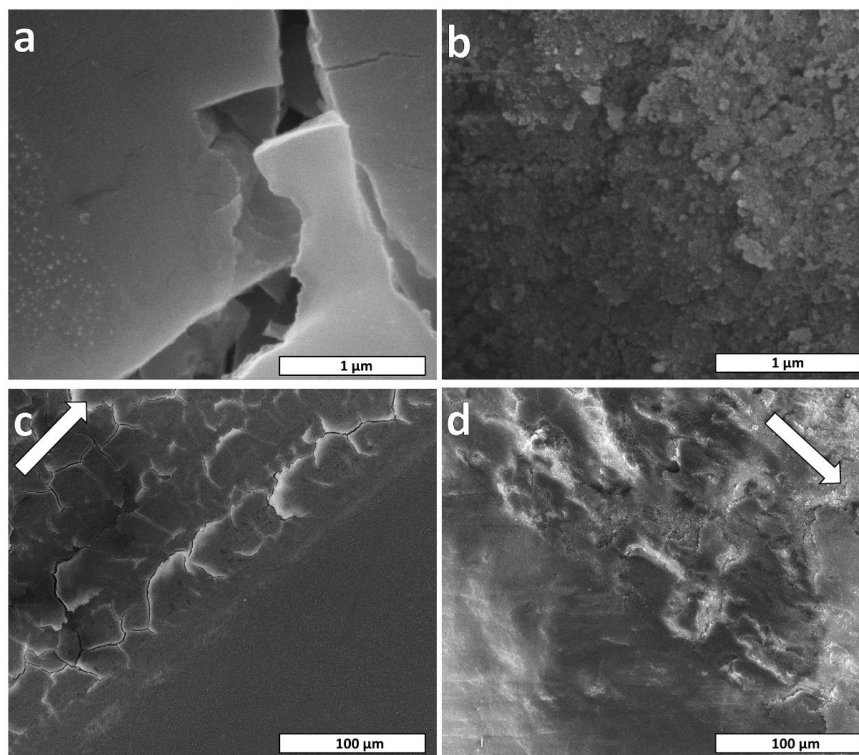
Figure 5.5. SEM images of wear tracks developed at 1 N for (a) SBG500 and (b) PG500M1. Magnified images taken from the edges for (c) SBG500 and (d) PG500M1.

60

The wear surface of SBG500 is smoother than that of all other PGs however, the presence of debris layer was observed as a protrusion in the middle area of wear track. On the other hand the wear tracks formed in the PGs surfaces have taken surface shape of the counterface properly. The wear track profiles shown in **Figure 5.6** corroborating further a higher μ value for parent SBG500 compared to that for PGs [118]. Since the hardness values were much lower than that of the zirconia ball counterface, all the surface layers were worn away significantly due to mechanical abrasion and brittle failure [119–121].
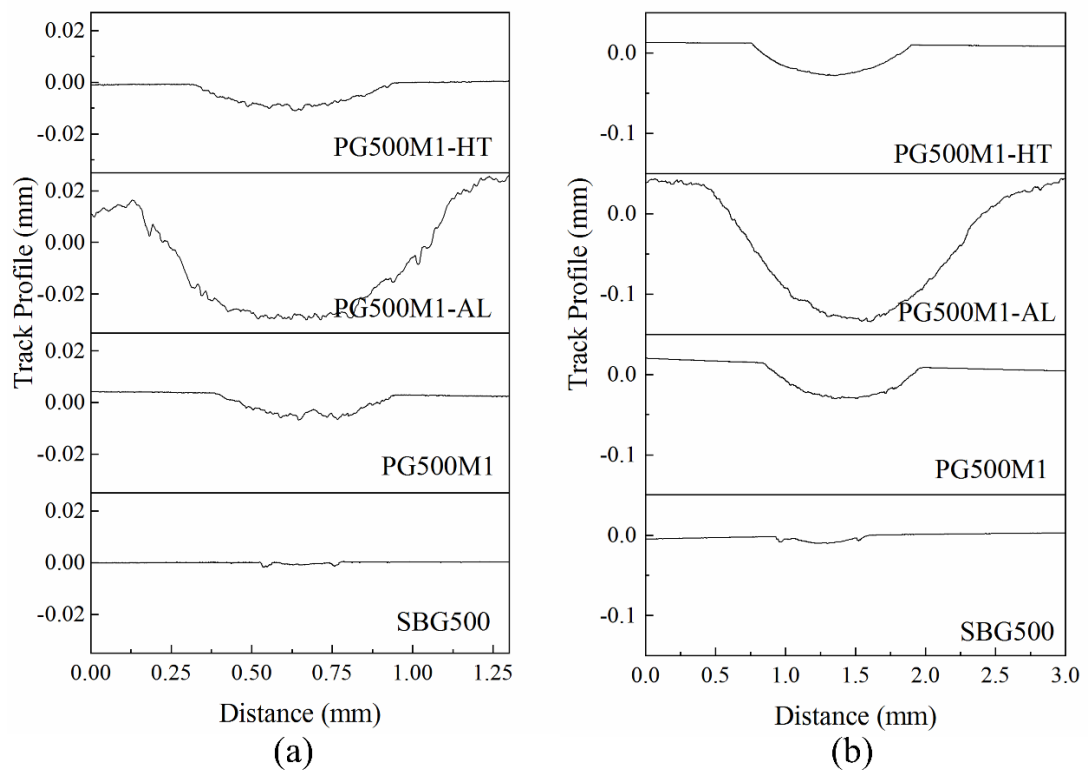
Figure 5.6. Wear track profiles traced at a load of (a) 1 N and (b) 5 N.

CHAPTER 6

RESULTS AND DISCUSSION: TiO$_2$ CRYSTALLIZATION WITHIN POROUS GLASS

6.1   General Remarks

In this part of the thesis, the results gathered from the experimental studies performed on TiO$_2$ crystallization within PGs and the photocatalytic properties of the TiO$_2$ embedded PGs (TiPGs) were presented and discussed. The crystallization of TiO$_2$ within PGs having different pore architectures and their metylene blue (MB) absorption and degradation properties were investigated. The photocatalytic performance of TiPGs under UV light was outlined by MB decolorization tests.

The appearances of TiPGs are shown in **Figure 6.1**. The surfaces of TiPG500M1 and TiPG500M1-AL seemed clear and homogeneous but, there were stained areas on the surfaces of TiPG500M1-HT and Tix2PG500M1, indicating that the TiO$_2$ crystallization did not form homogeneously and TiO$_2$ crystallites did not distribute uniformly from top to bottom and from side to side of the glass piece.

After TiO$_2$ crystallization process, the weight of PG500M1, PG500M1-AL, and PG500M1-HT increased by 2.8%, 3.3% and 1.8%, respectively. The application of the Ti impregnation process twice resulted in a negligible additional weight gain. Indeed, only 1% increase in the weight of TiPG500M1 was marked.
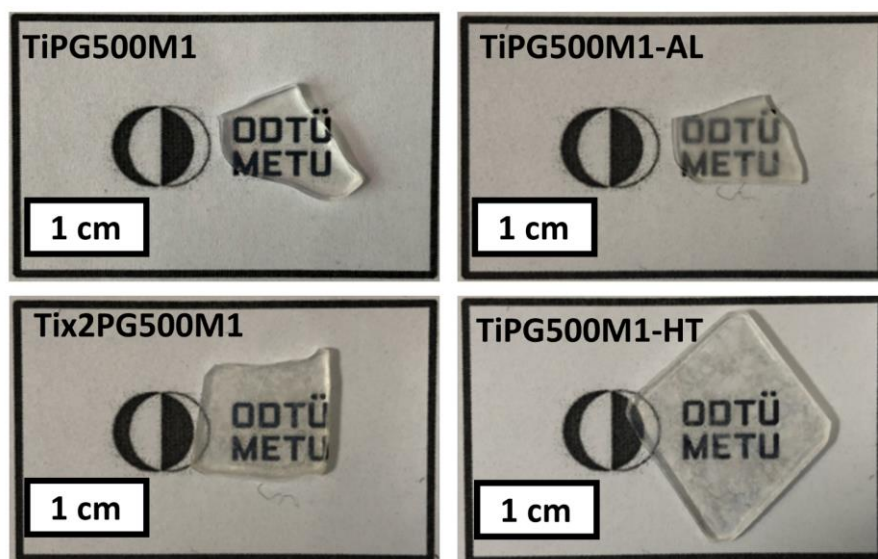
Figure 6.1. The photographs of the TiO$_2$ embedded PGs.

6.2   X-Ray Diffraction Analysis (XRD)

The XRD patterns of TiPGs and TiPow are illustrated in **Figure 6.2**. The XRD pattern of TiPow suggested that the powder is composed of only anatase crystallites (JCPDS card no. 21-1272). The XRD peaks at 2-theta of 25.3°, 36.9°, 37.7°, 38.5°, 48.0°, 53.8°, and 55.0° corresponding to the (101), (103), (004), (112), (200), (105), and (211) of anatase phase, respectively. The mean crystallite size (D) as calculated by using the Debye–Scherrer formula (D $=0.9\lambda$/FWHM* $\cos\theta$) was 30.9 nm. For calculations full-width at half maximum (FWHM) for the peaks corresponding to (101), (004), and (200) were considered.

The small but visible peak at 2θ of 25.3° belonging to the anatase phase in the XRD patterns of TiPG500M1 and TiPG500M1-AL suggested that the TiO$_2$ crystallites developed in these glasses. But, the peak was rather broad and actually there was no sign for other anatase peaks probably due to two reasons. The impregnated Ti precursor was not fully crystallized and/or the small amount of TiO$_2$ crystallites developed within the amorphous structure was too small to be detected by the x-ray diffractometer. Based on the same reasons, there was no peak observed in the XRD

pattern of TiPG500M1-HT. The peak became distinct in the XRD pattern of the two times Ti impregnated PG (Tix2PG500M1). Also new peaks emerged at 2θ of ~37°, ~48°, and ~55° agree with the findings of Anpo et al. [80]. The detection of new peaks in Tix2PG500M1 is related to both an increase in the number of titanium crystals within the glass structure and the growth of the primary crystallites developed during the first impregnation process as a result of the second impregnation. Since the grain growth of TiO_2 is a kinetic process based on diffusion [122], the heat treatment applied after secondary impregnation increased the total calcination time and led to the growth of TiO_2 grains .
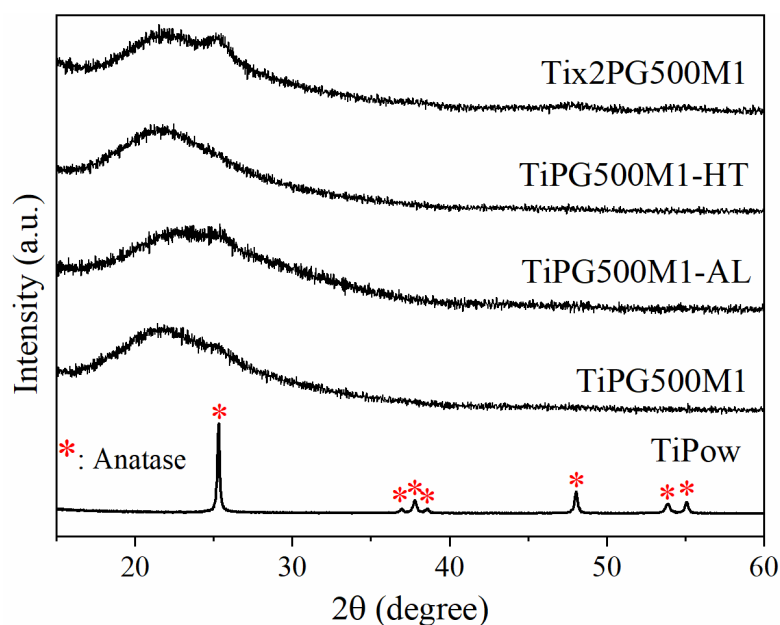
Figure 6.2. XRD patterns of Tix2PG500M1, TiPG500M1-HT, TiPG500M1-AL, TiPG500M1, and TiPow.

6.3   N₂ Adsorption-Desorption Analysis

Figure 6.3 shows the N_2 adsorption-desorption isotherm and PSD curve of TiPG500M1. PG500M1 and TiPG500M1 exhibits similar isotherms implying that TiO_2 crystallization did not affect the pore structure. Type IVa isotherm and the combination of H2a and H2b type hysteresis loops were recognizable. Nevertheless, the TiO_2 crystallites caused a decrease in SSA and V_P. SSA decreased from 358 to

282.9 m^2/g and V_P decreased from 0.314 to 0.277 cm^3/g upon crystallization of TiO_2 crystallites within the pore structure of PG500M1.
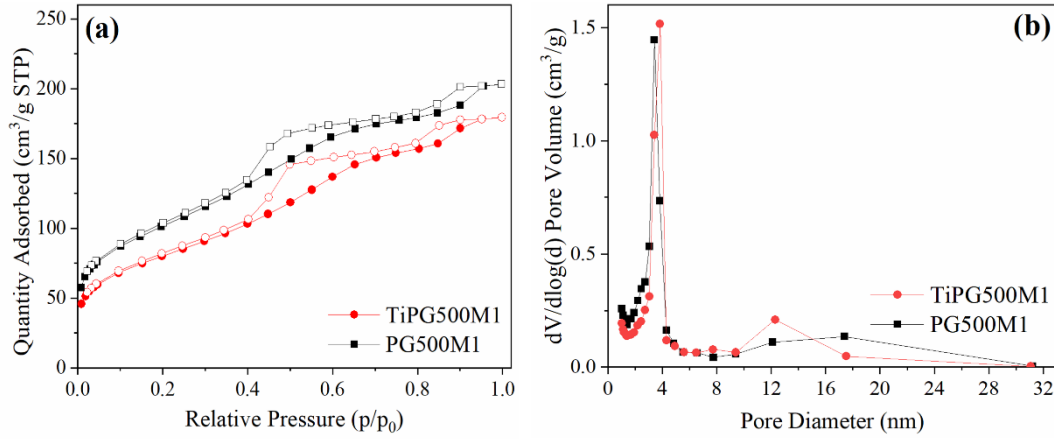
Figure 6.3. (a) N_2 adsorption-desorption isotherm and (b) PSD curves of TiPG500M1 and PG500M1.

6.4 Morphological Analysis and EDS

SEM images taken from the surfaces of TiPG500M1, TiPG500M1-AL, TiPG500M1-HT, and Tix2PG500M1 and their EDS spectra are shown in **Figure 6.4.** The surface pores of TiPGs are visible. But, a thin layer in some regions partially covered the porous structure. It was observed that the area of coated layer in TiPG500M1-HT and Tix2PG500M1 was wider than that in the other TiPGs. The detection of Ti peak in the EDS spectra of all samples proves that Ti is successfully impregnated and TiO_2 crystallites grown within the porous structure.

In order to identify the coating layer, EDS analysis was performed on the porous and covered regions. The SEM images taken from the surface of TiPG500M1 and the EDS spectra of the marked areas shown in **Figure 6.5 (a)** revealed that Si, Al, and Ti elements present in both porous and covered regions but, the Ti peak intensity is superior in the covered area. This finding proves that the coated layer is related to Ti. It is believed that the Ti layer formed on the surface and decreased pore size as a result of the first impregnation and caused formation of more Ti covered layers on the surface when the impregnation process was repeated.
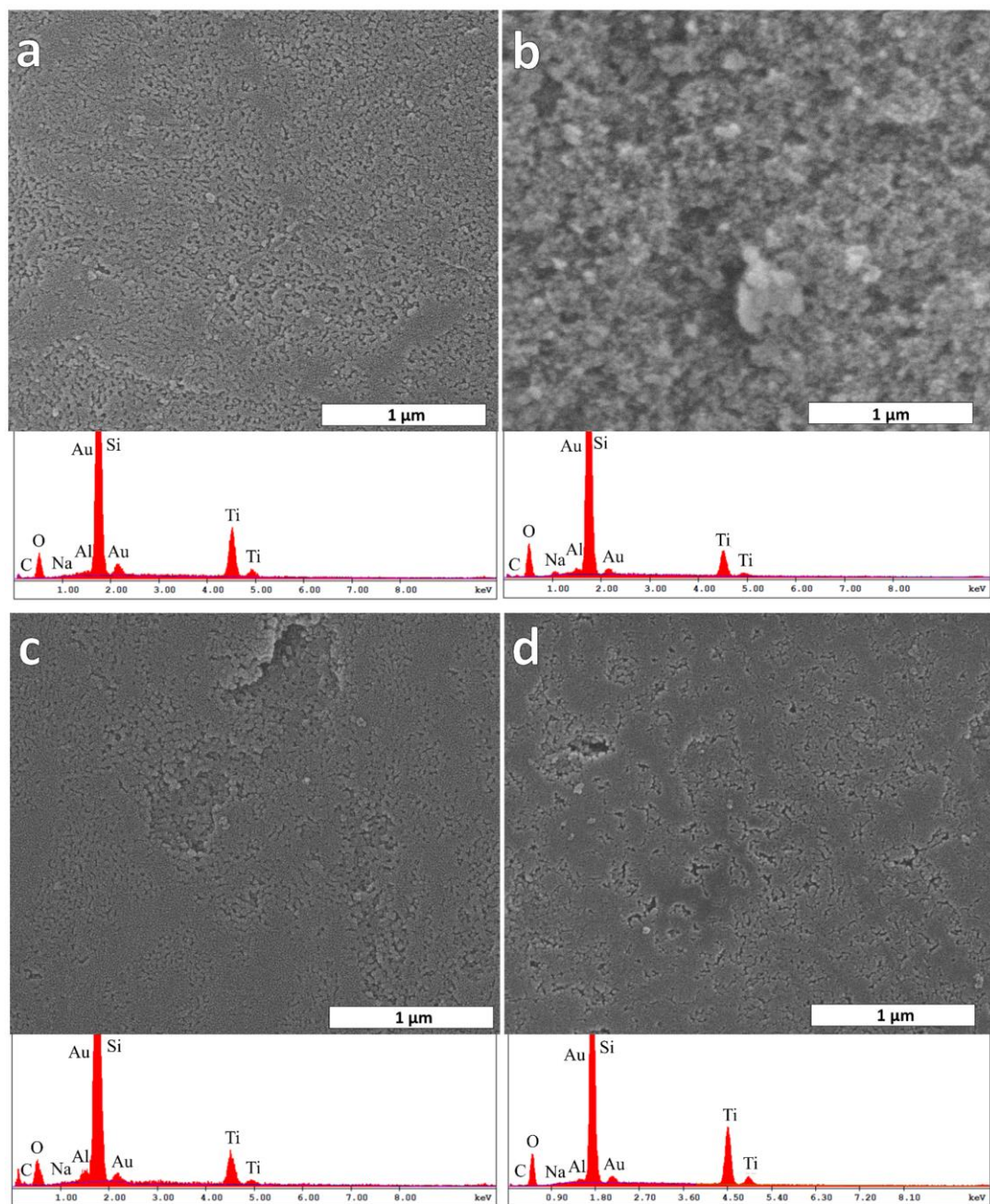
Figure 6.4. SEM images of (a) TiPG500M1, (b) TiPG500M1-AL, (c) TiPG500M1-HT, and (d) Tix2PG500M1 surface and their EDS spectrum.
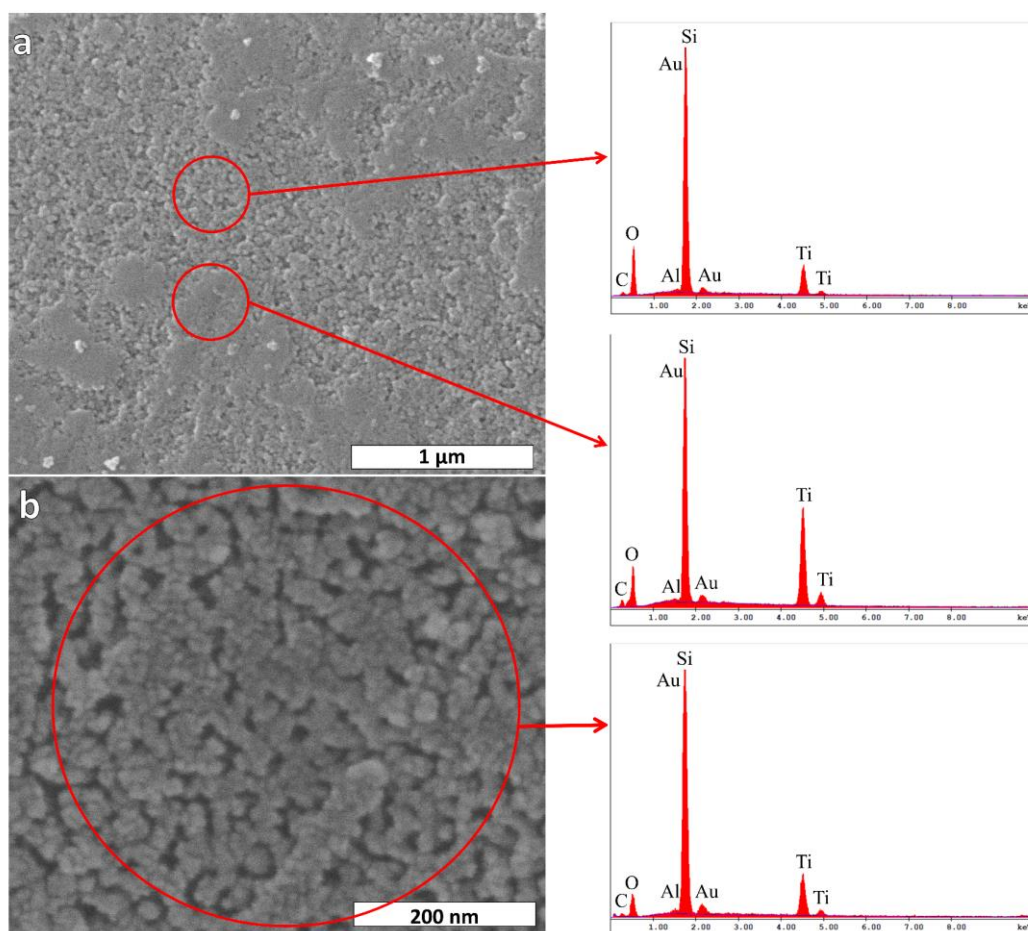
Figure 6.5. SEM image taken from the surface of TiPG500M1 at (a) 100,000X and (b) 500,000X and, corresponding EDS spectra of the marked areas.

Previous studies [3,4,84] revealed that B atoms migrate to the PG surface from interior as a result of heat treatment. The migrated B atoms form B-OH groups and borate clusters on the surface, which increases surface acidity. For TiPG500M1-HT, the acidic regions together with the decreased pore size might induce the formation of more Ti covered areas on the surface. Similar explanations were made also by Behnajady et al. [123] who reported that the acidic media promotes the polymerization of Ti-O-Ti species.

Although Ti was detected in EDS analysis of TiPG500M as shown in the EDS spectra in **Figure 6.5 (a)**, Ti crystallites developed could not be distinguished in the

SEM images even under magnification of 500,000X taken from the surface of TiPG500M1, shown in **Figure 6.5 (b)**.

The SEM and EDS analyses were performed on TiPGs to examine the morphology and chemical nature of the TiO_2 crystallites in the porous structure. **Figure 6.6** shows the SEM images taken from the edge (close to the surface) and on the middle of the fracture surfaces and EDS line analysis data for TiPG500M1, TiPG500M1-AL, TiPG500M1-HT, and Tix2PG500M1. The EDS line analysis was performed on the cross sectional view of TiPGs with a magnification of 300x shown by inlets in **Figure 6.6**, aiming to include the half thickness of the monolith (~750 µm). The EDS peaks of SiKα and TiKα were converted to ZAF corrected (intensity corrections applied by the instrument, related to the atomic number (Z), absorption (A) and fluorescence (F) effects) wt % ratio of these element by instrument which gives an information whether TiO_2 crystallites are distributed homogeneously throughout the thickness of the sample analyzed. The results revealed that at ~330 µm from the outer surface of TiPG500M1, the Ti concentration suddenly decreased by 90%. Repeated examinations of the same sample at different sections suggested that the Ti-rich layer depth varied ±40 µm.

The decrease in Ti concentration from the surface to the interior of TiPG500M1 could be interpreted in two ways. First, it can be considered that the Ti solution cannot infiltrate sufficiently to the interior of the glass due to nano size pores. The infiltration of the Ti solution may also be hindered by the relatively high concentration of silica clusters in the interior of the glass. Second, the water molecules in air could not penetrate inside of the glass so that the hydrolysis reaction with humidity in the air does not occur. Yamashita et al. [124] reported similar results. They anchored Ti into PG by metal ion implantation method and reported that the Ti concentration was higher in the near the surface region (~40 nm depth). On the contrary, Kawamura et al. [125] reported that the Ti concentration increased in the center of the sample. They proposed that a small amount of silica gel remaining in the pores promotes the adsorption of Ti in the glass structure.

The concentration of Ti in the near-surface region of TiPG500M1-AL was about 2 times more than TiPG500M1. Ti concentration gradually decreased to the interior and reached about TiPG500M1 level within ~40 μm as shown in **Figure 6.6 (b)**. This is thought to be due to the presence of larger pores on the surface of TiPG500M1-AL. Thus, the Ti solution easily penetrated into the glass. Also, thanks to the voids formed by the larger pores and microcracks, TiPG500M1-AL had less space constraint factor than TiPG500M1 so TiO_2 agglomeration was easier. The Ti-rich layer depth was almost identical to that observed in PG500M1. For TiPG500M1-HT, the thin pores caused a partial reduction of the Ti concentration and reduced the Ti-rich layer depth by ~150 μm as shown in **Figure 6.6 (c)**. As expected, the second impregnation process resulted in an increase in both Ti-rich layer depth and Ti concentration as shown in **Figure 6.6 (d)**.
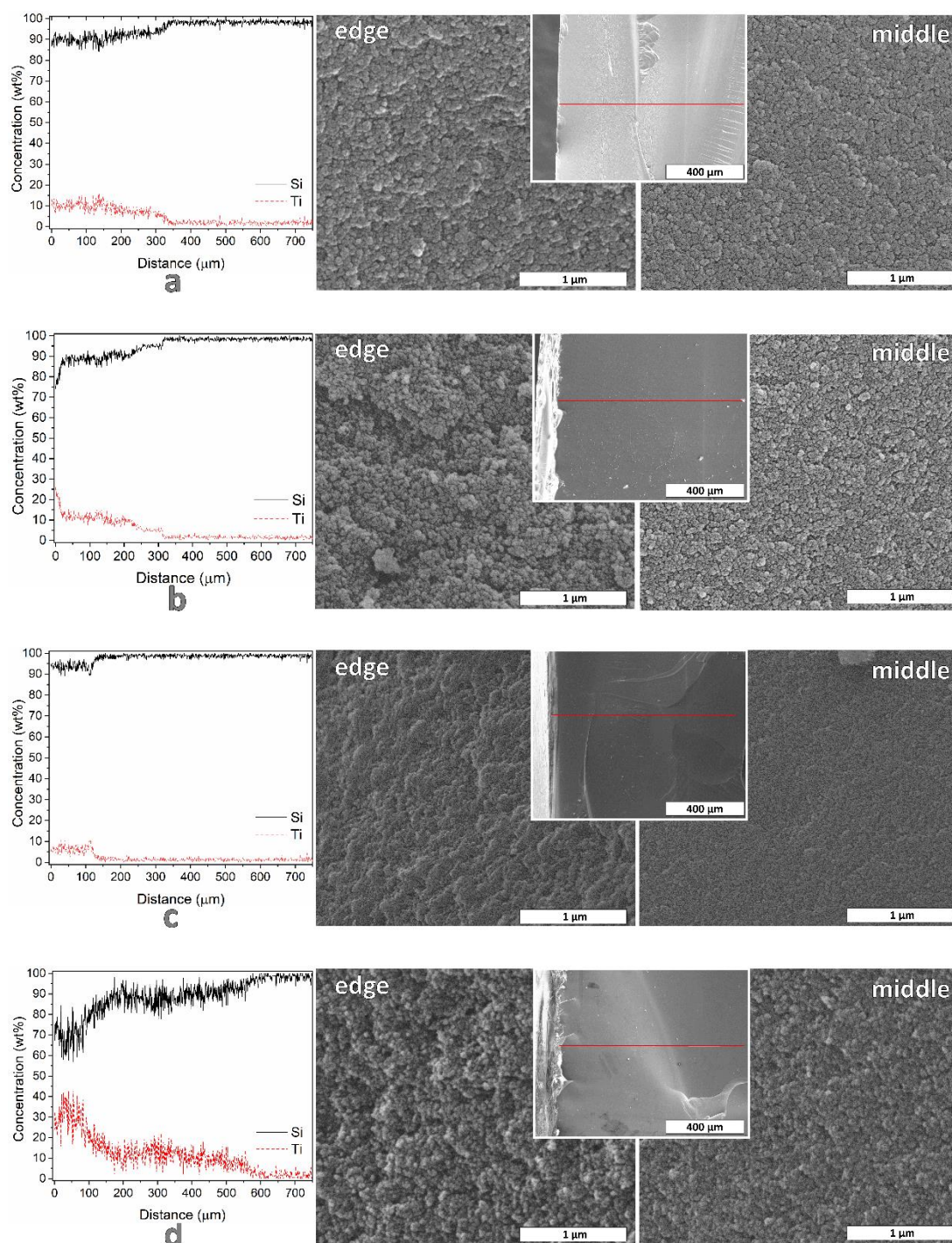
Figure 6.6. EDS line analysis and the cross sectional view taken from the edge (close to the surface) and the middle of the fracture surfaces for (a) TiPG500M1, (b) TiPG500M1-AL, (c) TiPG500M1-HT, and (d) Tix2PG500M1.

6.5   FTIR Analysis

The FTIR spectra for TiPow, TiPG500M1, and PG500M1 are shown in **Figure 6.7**. The dominant band centered at ~438 cm^{-1} in the spectrum of TiPow is assigned to Ti–O–Ti bonds in crystalline TiO$_2$ structures [126,127]. The bands of the Ti-O-Ti and Si-O-Ti bonds at 430 and 960 cm^{-1}, respectively [128,129] were expected in TiPG500M1. But, they were absent due to overlapping of the bands present at the same wavenumbers in PG500M1.
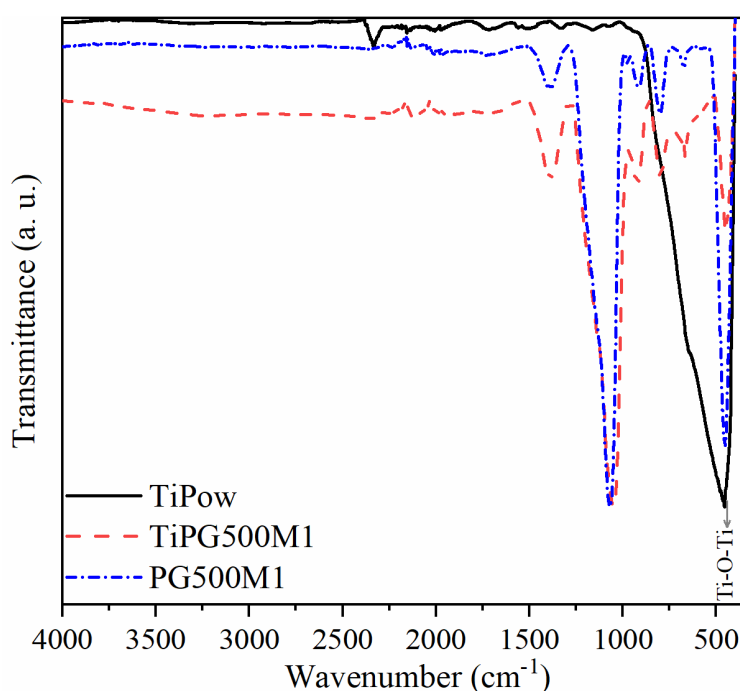
Figure 6.7. FTIR spectra of TiPow, TiPG500M1, and PG500M1.

6.6   Optical Transmittance

Figure 6.8 represents the optical transmittance spectra for Tix2PG500M1, TiPG500M1-AL, TiPG500M1-HT, and TiPG500M1. It was recognized that the transparency of the glasses decreased significantly after Ti impregnation. TiO$_2$ crystallites developed within or on the surface of glass caused scattering and decreased the transparency. It is commonly known that the increase in the surface roughness, TiO$_2$ layer thickness, and the crystallite size of TiO$_2$ or non-homogeneous

coatings cause significant loss in transparency [81,130,131]. This is evidenced by the fact that Tix2PG500M1 had lower transparency than TiPG500M1. Also, the transparency of TiPG500M1-HT decreased more than that of TiPG500M1 after Ti impregnation due probably to the non-homogeneous regions on the surface.

The absorption edge of PG500M1 at ~225 nm (see **Figure 4.12**) shifted to ~340-370 nm in TiPGs. The adsorption edge at 370-380 nm (~3.2 eV) was assigned to the intrinsic band gap absorption of anatase TiO_2 [130,132]. The shift in the adsorption edge is one of the evidences that TiO_2 crystallites grown within the PG structure. Even though an Eg value for TiO_2 crystallites could be calculated from the absorption edge [126,132–134], it is not acceptable because of the surface roughness and coating thickness that are the factors affecting the Eg calculations, are variable in these inhomogeneous samples. Nevertheless, it could be said that the distinctive shifting of the absorption edge of Tix2PG500M1 to higher wavelengths resulted in a lower Eg value. The Eg of TiO_2 decreased with increasing TiO_2 content deposited on the surface and this was associated with increased number of TiO_2 layers on the surface and bigger grain size due to agglomeration [80,124,135].
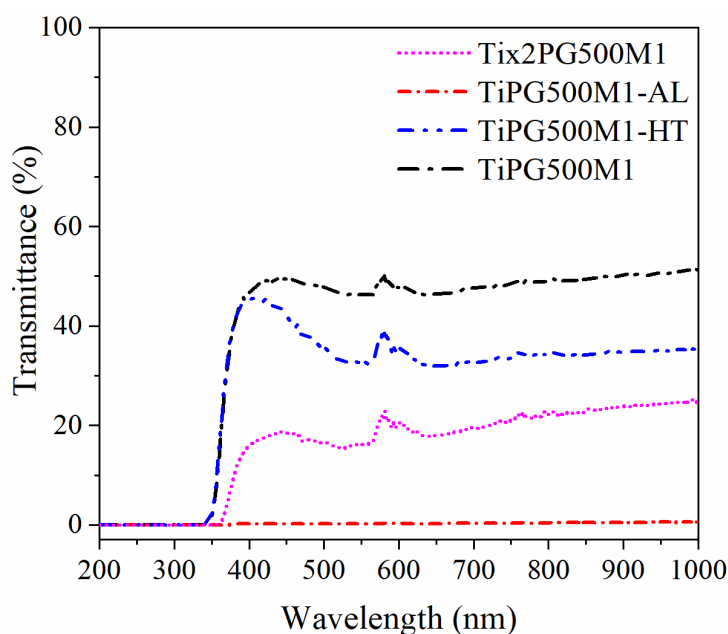
Figure 6.8. The transmittance spectra of Tix2PG500M1, TiPG500M1-AL, TiPG500M1-HT, and TiPG500M1.

6.7　Band Gap Measuraments

Kubelka-Munk transformed reflectance graphs of TiPG500M1, TiPG500M1-AL, TiPG500M1-HT, Tix2PG500M1, and TiPow are illustrated in **Figure 6.9**. The values for the indirect Eg were tabulated in **Table 6.1**. The Eg value of TiO_2 vary depending on the crystallite size [132,136,137], dopant elements [138,139], coexistance of rutile and anatase phases together [140,141] and lattice defects in the structure [141,142]. It is frequently reported that, anatase and rutile phases of TiO_2 have Eg values of 3.2 and 3 eV, respectively [83,143]. Also, some other researchers [136,144] reported that the Eg value of the pure anatase phase is around 3 eV, similar to that measured for TiPow.

It is well known that Eg increases with decreasing particle size due to the quantum size effect [83,145]. The higher Eg value of TiPG500M1 as compared to TiPow indicates that the TiO_2 crystallites developed within the pores were small in particle size due to the size restriction effect of the pores. Also, porous structure inhibited the agglomeration tendency of the TiO_2 particles trapped in the pores [79,145]. The Eg value of TiPG500M1-AL was lower than that of TiPG500M1 attributed to the decrease of volume restriction effect due to the increased pore size on the surface, which leads to growth of larger TiO_2 particles on the glass surface. Although the pore size of TiPG500M1-HT was lower than that of TiPG500M1, the TiO_2 coated layers formed on this glass surface led a lower Eg value by allowing the presence of larger grains on the surface. The Eg value of Tix2PG500M1 was almost the same as that of TiPow. It is believed that the decrease of Eg caused by the double impregnation that promotes agglomeration and grain growth, together with the increase of TiO_2 coated layers on the surface. In like manner, Jiang et al. [146] showed that TiO_2 particles synthesized on porous supports exhibit Eg's between 3.1 to 3.5 eV and Eg decreased with increasing TiO_2 loading rate.

Furthermore, for TiPG500M1-HT and Tix2PG500M1, there was a deviation of 0.05 eV between Eg values measured from different regions of the samples. It is possible to speculate that the Ti coated layer formed on the surface of these samples is high.

That is, the presence of crystallites growing on the porous structure rather than inside the pores, led to the development of larger TiO_2 particles. It was concluded that the non-homogeneous distribution of TiO_2 on the surface revealed a variation of Eg values measured for these inhomogeneous samples.
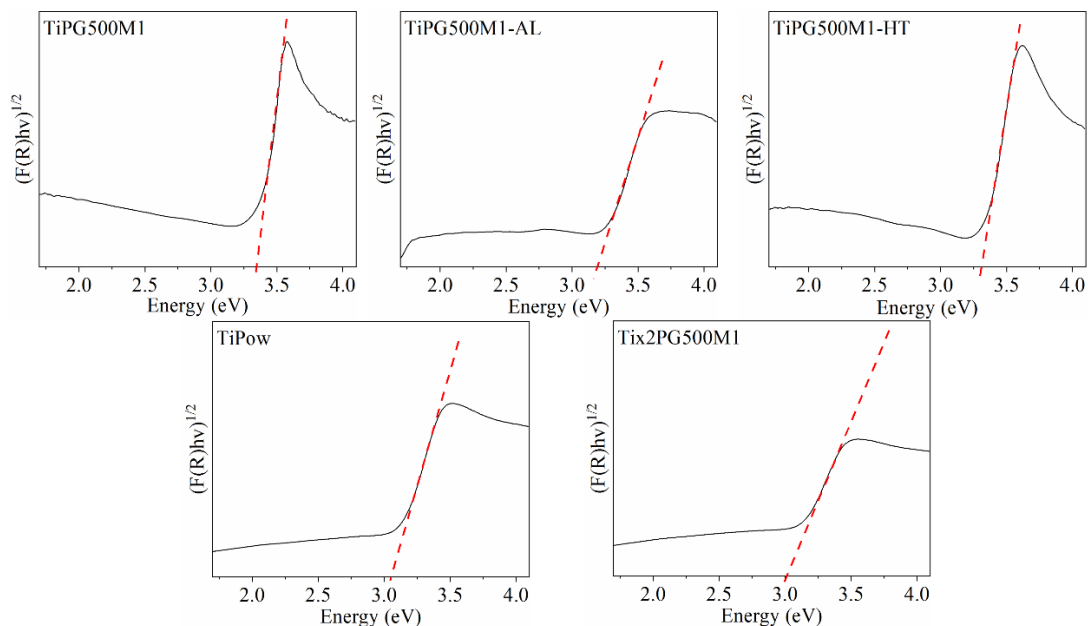
Figure 6.9. Kubelka-Munk transformed reflectance graphs for TiPG500M1, TiPG500M1-AL, TiPG500M1-HT, TiPow, and Tix2PG500M1.

Table 6.1. Band gap energy values of TiPow, TiPG500M1, TiPG500M1-AL, TiPG500M1-HT and, Tix2PG500M1.

Sample	Band Gap (eV)
TiPow	3.05
TiPG500M1	3.35
TiPG500M1-AL	3.19
TiPG500M1-HT	3.31
Tix2PG500M1	3.03

6.8 Methylene Blue Degradation

In general, the adsorption-desorption equilibrium is maintained in the dark environment in the photocatalytic performance measurements. Then, the photocatalytic performance measurement is performed under UV light. However, in the present study, it was experienced that the maintenance of the adsorption-desorption equilibrium takes a long time for the PGs investigated. The MB absorbance spectra and removal efficiency (RE) values of PG500M1 are given in **Figures 6.10 (a)** and **(b)**, respectively. Even after 9.5 h of testing time adsorption continued throughout, no desorption was noticed. Since the adsorption takes rather a long time, it is not practical to conduct photocatalytic performance measurements after the adsorption-desorption equilibrium is achieved. It is also thought that, even if complete adsorption is maintained, the concentration of MB in the solution will be too low to produce reasonable and reliable results. For that reasons, the MB decolorization tests were performed to investigate the photodecomposition performance of TiPGs both in the dark and under UV light. The photocatalytic performance was defined by the difference of the MB concentrations between the two measurements.
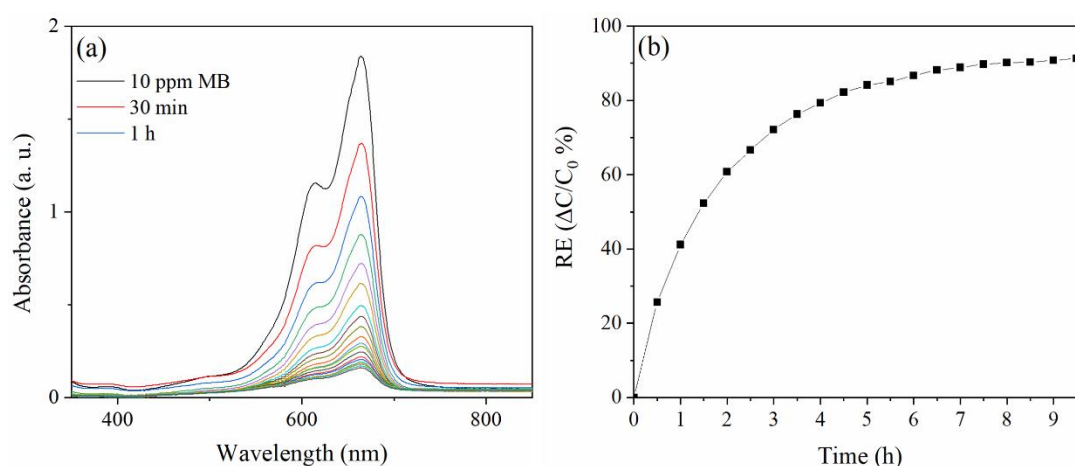
Figure 6.10. (a) Absorbance spectra for MB solutions and (b) removal efficiency of PG500M1 with time.

76

Figure 6.11 (a) shows the RE values measured at dark for PG500M1, PG500M1-HT, and PG500M1-AL. The adsorption rate of all glasses decreases over time as seen in **Figure 6.11 (a).** The adsorption rate was very high within the first 3 h but, subsequently decreased as shown in **Figure 6.10 (b)**. The high adsorption capability of PG is related to the nano size porous structure, high SSA, and V_P as well as the negatively charged silanol residues on the surface of this structure [4,147]. Being a cationic dye, MB molecules are attracted by the negatively charged surface of the glass. Although PG is a good adsorbent, the diffusion rate of adsorbate into the porous structure is very low and decreases as the pore size decreases because of the physical reasons such as the fractal geometry and tortuosity of the porous structure, together with chemical effects such as the sticking effect of the active sides [148–150]. The decrease in the MB adsorption rate with time is related to the attachment of the molecules to the pore walls. The MB molecules attached to the pore walls block the active sides on porous surface and retard the MB solution to infiltrate into the glass. It should also be mentioned that the experiments were carried out on PG chunks instead of powder. The use of PG chunks in the experiments prolongs the path that the MB solution has to travel to reach the pores and active areas in the specimen. PGs seemed in the color of MB during the MB degradation tests and as the test progress the color gradually darkens and reaches a dark blue at the end. A representative photograph of PG500M1 after the MB degradation test is depicted in **Figure 6.11 (b)**.

Li et al. suggested that there are two stages in the adsorption of MB molecules to the adsorbate [151]. In the first stage, MB molecules are attached to the surface active sites and external diffusion together with number of the active sites control this stage. This adsorption is based on the electrostatic attraction between the negatively charged Si-OH on the PG surface and the positively charged MB molecules in the solution, together with the hydrogen bonding between the amine group of MB molecule and Si-OH [152]. Once the surface active sites are completely filled, the intra-pore diffusion mechanism, i.e. the second stage, begins to play an active role [151]. It is believed that the first stage has a great effect on the second stage and there

is a delicate balance between these two mechanisms particularly in adsorption experiments using bulk samples. Excessive surface active sites may reduce the diffusion of MB molecules into the pores.
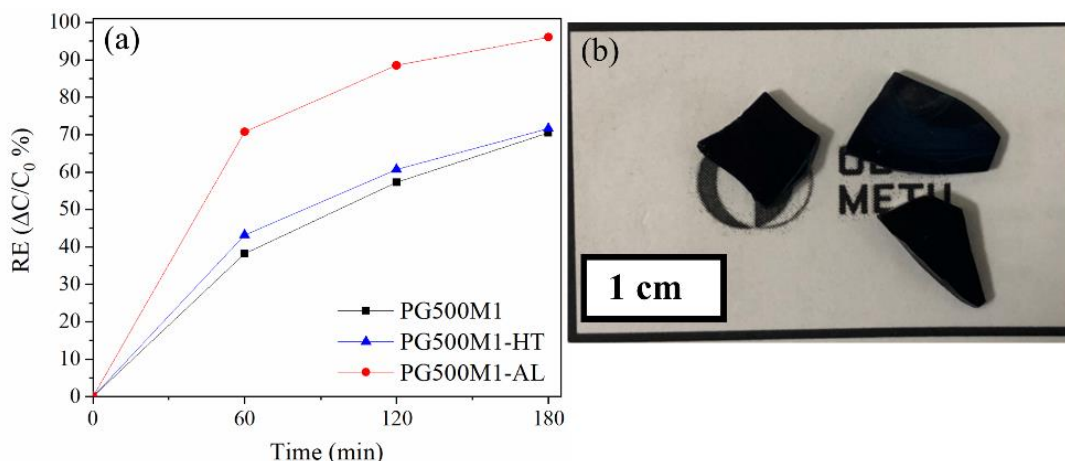
Figure 6.11. (a) The removal efficiency values measured at dark for PG500M1, PG500M1-HT, and PG500M1-AL and (b) the photograph of PG500M1 after MB degradation test.

The SSA of PG500M1-AL was the lowest one in the tested glasses but, PG500M1-AL has the highest MB adsorption capacity. The data clearly put forward that SSA is not the main contributing parameter for the adsorption capability. Conclusively, more accessible surface area is more beneficial than a large surface area for the MB adsorption for PGs. The secondary pore size has a direct effect on the adsorption rate. Also, removing the silica clusters by alkali leaching enables the penetration of the MB solution through the porous structure easier. This may be explained by the fact that the expansion of the liquation channels allows the MB solution to diffuse more easily into the PG structure [8,81,153].

Although both the secondary pore size and V_P of PG500M1-HT was less than those of PG500M1, the RE values of both PGs were almost equal. This could be attributed to the increase in the primary pore size, i.e. the reduction of the complexity of the structure by the sintering of silica clusters during heat treatment. The effect of changes in surface chemistry of PG due to the heat treatment should also be considered. Several researchers reported that as a result of heat treatment, Si-OH

groups on the surface were removed while B-OH groups and surface acidity were increased [3,4,84]. Tan et al. stated that increased surface acidity increases MB adsorption [154]. There are also studies reporting that B-OH groups increase water adsorption [155] and surface reactivity [4,156]. One of the reasons why PG500M1-HT has the RE value as much as PG500M1 may be related to these changes in surface chemistry. Further detailed studies are needed to reveal the effects of surface chemistry on MB adsorption.

In order to compare the RE of TiPGs with that of a TiO_2 powder under the same experimental conditions, TiPow was subjected to MB experiments. The amount of TiPow subjected to the test was 0.01 g that is more or less equal to the TiO_2 content in TiPGs. **Figures 6.12 (a)** and **(b)** shows the comparison of MB removal efficiency of TiPGs and TiPow at dark and under UV light, respectively. To calculate the realistic photocatalytic performance (PP) of TiPGs, the RE value in dark and the self-degradation of MB under UV light (~ 2.3% per hour) were subtracted from the RE value under UV light thus PP values calculated by the following equation.

$$PP = RE_{UV} - (RE_{Dark} + \text{Self Degradation}) \tag{12}$$

The RE and PP values as calculated at the end of the 3 h of tests for TiPGs and TiPow are given in **Table 6.2**.
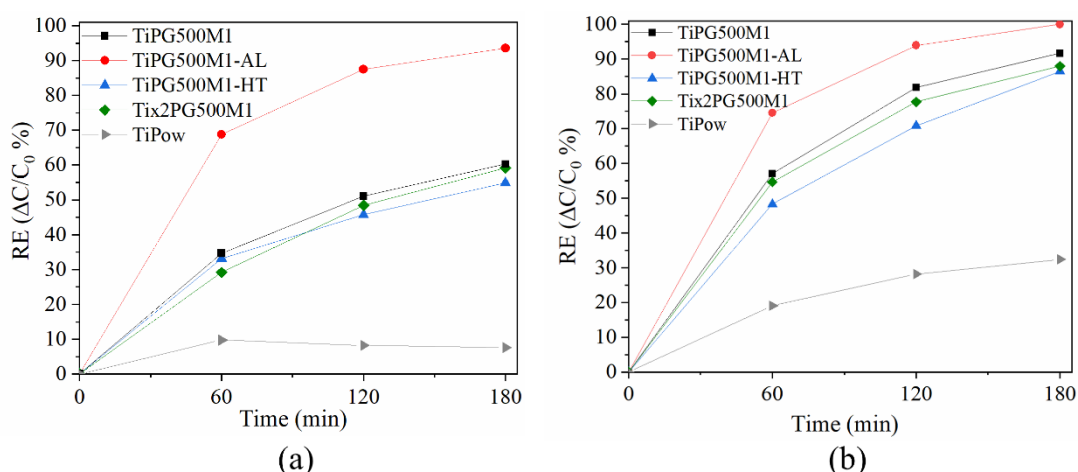
Figure 6.12. The removal efficiency values measured (a) at dark and (b) under UV light for TiPGs and TiPow.

Table 6.2. The removal efficiency and photocatalytic performance values at the end of the 3 h tests for TiPGs, and TiPow.

Sample	RE in Dark	RE under UV	PP
TiPG500M1	60.2	91.6	24.5
TiPG500M1-HT	54.8	86.4	24.7
TiPG500M1-AL	93.5	100	0
Tix2PG500M1	59.8	87.9	21.2
TiPow	7.6	32.3	17.8

Positive PP value for all TiPGs except TiPG500M1-AL is evidence that TiPGs are photocatalytically active. Indeed it is difficult to compare the photocatalytic performance of TiPG500M1-AL due to its very high MB adsorption rate. The PP values of TiPG500M1 and TiPG500M1-HT were ~7% bigger than that of TiPow. It was reported in many studies [79,145,146,157–161] that TiO_2 crystals dispersed in a porous structure exhibit better photocatalytic performance than bulk TiO_2. The reasons for the enhanced photocatalytic activity are:

i. Highly dispersed TiO_2 crystals on the high surface area of support material can react with reactant molecules easily. This effect increases if the support material has adsorbing capability, due to the increasing the quantity of reactants close to the TiO_2 sites relative to the solution [160].

ii. The attachment of TiO_2 crystals to the support surface prevents agglomeration.

iii. The crystallized TiO_2 particles in the pores of support material become smaller thanks to the volume restriction. Smaller particle size decreases the path of the charge carriers to migrate to surface of the TiO_2, resulting in a decrease of the recombination rate of the charge carriers. Also, due to quantum confinement effect, Eg of TiO_2 increases with decreasing particle size [80,145,146].

iv. If transparent materials such as PG are used as the support material, more TiO$_2$ could be exited through penetrating UV light into the support material [81].

The PP values of TiPG500M1 and TiPG500M1-HT were almost the same and that of Tix2PG500M1 was lower than the others. Conclusively, high TiO$_2$ concentration in PG had no significant effect on photocatalytic performance. Similar results have been reported previously by Yamashita et al. [124] and Yazawa et al [81]. It can be concluded that shielding effect [159,162] decreased photocatalytic performance of Tix2PG500M1 due to reduction of UV light penetration. In addition, the separation of TiO$_2$ crystallites from each other is one of the parameters that increase photocatalytic performance but, this effect decreases with increasing Ti concentration [80].

CHAPTER 7

CONCLUSIONS

Porous glasses (PGs) with various pore architectures are successfully produced by acid leaching process conducted on a sodium borosilicate glass with a nominal composition of $55.7SiO_2$-$33.6B_2O_3$-$9.2Na_2O$-$1.5Al_2O_3$ (wt %). Surface crystallization takes place when the SBG is heat treated at 625 °C for 9 h. But PGs maintain their amorphous nature upon heat treatment at 800 °C for 1 h. The glass transition temperature of PG500M1 is around 660 °C.

The transparency of the PG500M1 is 75% in the visible region and decreases to 10% due to alkali treatment which causes enlargement of the pores, increase of surface roughness, and micro cracks.

The pore architecture can be tailored depending on the process variables such as heat treatment temperature, molarity of the acid leaching solution, alkali treatment, and heat treatment after acid leaching. SSA and V_P of PGs produced range from 207 to 367 m^2/g and from 0.227 to 0.370 cm^3/g, respectively. The heat treatment temperature mainly affects the width of liquation channels. On the other hand the acidic strength of the leaching solution influences the primary pores associated with silica precipitates.

The acid and successive alkali treatments have profound effects on the pore structure, microhardness, and tribological properties of PG500M1. While the hardness (298 MPa) and friction coefficient (0.47) of PG500M1 is lower, the wear rate (11.82×10^{-4} $mm^3/N.m$ at 1 N load) is higher than that of the SBG500 due to additional porosity and residual etching stresses. The total pore volume and wear rate further increases with successive alkali treatment and the microhardness decreases. Instead, the heat treatment conducted on does not have a significant effect on the microhardness and the wear rate.

TiO$_2$ embedded porous glass can be successfully produced by solution impregnation method. The TiO$_2$ distribution continues throughout the sample thickness while the concentration near the surface is higher. After TiO$_2$ crystallization, the visible region transparency of PG500M1 decreased to ~48%.

Methylene blue degradation tests reveas that PG has high MB adsorption capability and TiO$_2$ embedded PG exhibits superior photocatalytic performance than TiO$_2$ powder thanks to the finely dispersed TiO$_2$ crystals formed in the pores. It is assumed that the TiO$_2$ embedded porous glass is a suitable candidate for practical wastewater cleaning applications.

CHAPTER 8

FUTURE WORKS

The following investigations are recommended to be carried out in future.

In order to fully understand the factors affecting the pore structure, it will be useful to do further experiments by changing the heat treatment temperature, molarity of the acid and alkali leaching solution, and consolidation heat treatment temperature in a wider range.

It will be beneficial to demonstrate other mechanical properties such as rupture strength and elastic modulus of PG.

Ti impregnation process should be tested with different precursor solutions with different Ti source molarity.

Although the impregnation and calcination method utilized to grow TiO_2 crystals into PG is a simple and device-free technique, it causes an inhomogeneous Ti layer to form on the PG surface. Vapor deposition methods might be useful for a better TiO_2 dispersion.

REFERENCES

[1]   G.Q. Lu, X.Z. Zhao, Nanoporous Materials: Science and Engineering, Ser. Chem. Eng. 4 (2004).

[2]   M.E. Nordberg, Properties of some Vycor brand glasses, J. Am. Ceram. Soc. 27 (1944) 299–305.

[3]   A.L. Dawidowicz, Controlled porosity glasses (CPGs) as adsorbents, molecular sieves, ion-exchangers and support materials, in: Stud. Surf. Sci. Catal., 1996: pp. 31–56.

[4]   F. Schüth, K.S.W. Sing, J. Weitkamp, Handbook of porous solids, Wiley-Vch, 2002.

[5]   W.-Y. Dong, Y.-C. Long, Preparation and characterization of preferentially oriented continuous MFI-type zeolite membranes from porous glass, Microporous Mesoporous Mater. 76 (2004) 9–15.

[6]   H. Ohya, J.J. Kim, A. Chinen, M. Aihara, S.I. Semenova, Y. Negishi, O. Mori, M. Yasuda, Effects of pore size on separation mechanisms of microfiltration of oily water, using porous glass tubular membrane, J. Memb. Sci. 145 (1998) 1–14.

[7]   C. Schmöger, T. Szuppa, A. Tied, F. Schneider, A. Stolle, B. Ondruschka, Pd on porous glass: a versatile and easily recyclable catalyst for suzuki and heck reactions, ChemSusChem. 1 (2008) 339–347.

[8]   R. Müller, N. Anders, J. Titus, D. Enke, Ultra-thin porous glass membranes: An innovative material for the immobilization of active species for optical chemosensors, Talanta. 107 (2013) 255–262.

[9]   S. Li, L. Nguyen, H. Xiong, M. Wang, T.C.C. Hu, J.-X. She, S.M. Serkiz, G.G. Wicks, W.S. Dynan, Porous-wall hollow glass microspheres as novel potential nanocarriers for biomedical applications, Nanomedicine Nanotechnology, Biol. Med. 6 (2010) 127–136.

[10]   T.H. Elmer, Porous and reconstructed glasses, ASM Int. Eng. Mater.

Handbook. 4 (1991) 427–432.

[11]   D. Enke, F. Janowski, W. Schwieger, Porous glasses in the 21st century—a short review, Microporous Mesoporous Mater. 60 (2003) 19–30.

[12]   E.C. Bucharsky, K.G. Schell, R. Oberacker, M.J. Hoffmann, Preparation of transparent glass sponges via replica method using high purity silica, J. Am. Ceram. Soc. 93 (2010) 111–114.

[13]   A. Sadighzadeh, M. Ghoranneviss, A.S. Elahi, Application of partial sintering of waste glasses for preparation of porous glass bodies, J. Porous Mater. 21 (2014) 993–999.

[14]   K. Yanagisawa, N. Bao, L. Shen, A. Onda, K. Kajiyoshi, Z. Matamoras-Veloza, J.C. Rendón-Angeles, Development of a technique to prepare porous materials from glasses, J. Eur. Ceram. Soc. 26 (2006) 761–765.

[15]   H.R. Fernandes, D.U. Tulyaganov, J.M.F. Ferreira, Preparation and characterization of foams from sheet glass and fly ash using carbonates as foaming agents, Ceram. Int. 35 (2009) 229–235.

[16]   Y. Xi, Z. Liangying, W. Sasa, Pore size and pore-size distribution control of porous silica, Sensors Actuators B Chem. 25 (1995) 347–352.

[17]   W.E.S. Turner, F. Winks, The influence of boric oxide on the properties of chemical and heat-resisting glasses. Part II. The resistance to chemical reagents, J. Soc. Glas. Tech. 10 (1926) 102–113.

[18]   H.H. Porter, N.M. Emery, Treated borosilicate glass, Patent No. 2,106,744, 1938.

[19]   D. Enke, K. Otto, F. Janowski, W. Heyer, W. Schwieger, W. Gille, Two-phase porous silica: Mesopores inside controlled pore glasses, J. Mater. Sci. 36 (2001) 2349–2357.

[20]   W. Vogel, Glass chemistry, Springer Science & Business Media, 2012.

[21]   D. Enke, F. Janowski, W. Gille, W. Schwieger, Structure and texture analysis of colloidal silica in porous glasses, Colloids Surfaces A Physicochem. Eng.

Asp. 187 (2001) 131–139.

[22] G. Toquer, C. Delchet, M. Nemec, A. Grandjean, Effect of leaching concentration and time on the morphology of pores in porous glasses, J. Non. Cryst. Solids. 357 (2011) 1552–1557.

[23] W. Haller, Rearrangement kinetics of the liquid—liquid immiscible microphases in alkali borosilicate melts, J. Chem. Phys. 42 (1965) 686–693.

[24] S. V Stolyar, T. V Antropova, D. V Petrov, I.N. Anfimova, Viscosity and shrinkage of porous and quartzoid glasses of the $Na_2O\text{-}B_2O_3\text{-}SiO_3$ system, Russ. J. Appl. Chem. 81 (2008) 974–977.

[25] T. V Antropova, I.A. Drozdova, T.N. Vasilevskaya, A. V Volkova, L.E. Ermakova, M.P. Sidorova, Structural transformations in thermally modified porous glasses, Glas. Phys. Chem. 33 (2007) 109–121.

[26] A. V Volkova, L.E. Ermakova, M.P. Sidorova, T. V Antropova, I.A. Drozdova, The effect of thermal treatment on the structural and electrokinetic properties of porous glass membranes, Colloid J. 67 (2005) 263–270.

[27] B. Reinhardt, D. Enke, F. Syrowatka, Preparation of porous, hierarchically organized glass monoliths via combination of sintering and phase separation, J. Am. Ceram. Soc. 95 (2012) 461–465.

[28] D.J. O'Brien, T.F. Juliano, P.J. Patel, S.H. McKnight, Optically transparent nanoporous glasspolymer composites, Army Research Lab., 2006.

[29] T. Aytug, J.T. Simpson, A.R. Lupini, R.M. Trejo, G.E. Jellison, I.N. Ivanov, S.J. Pennycook, D.A. Hillesheim, K.O. Winter, D.K. Christen, Optically transparent, mechanically durable, nanostructured superhydrophobic surfaces enabled by spinodally phase-separated glass thin films, Nanotechnology. 24 (2013) 315602.

[30] J. Rouquerol, D. Avnir, C.W. Fairbridge, D.H. Everett, J.M. Haynes, N. Pernicone, J.D.F. Ramsay, K.S.W. Sing, K.K. Unger, Recommendations for the characterization of porous solids (Technical Report), 1994.

[31] B.-L. Su, C. Sanchez, X.-Y. Yang, Hierarchically structured porous materials: from nanoscience to catalysis, separation, optics, energy, and life science, John Wiley & Sons, 2012.

[32] P. Colombo, C. Vakifahmetoglu, S. Costacurta, Fabrication of ceramic components with hierarchical porosity, J. Mater. Sci. 45 (2010) 5425–5455.

[33] K. Ishizaki, S. Komarneni, M. Nanko, Porous Materials: Process Technology and Applications, Springer Science & Business Media, 2013.

[34] L. Lefebvre, J. Banhart, D.C. Dunand, Porous metals and metallic foams: current status and recent developments, Adv. Eng. Mater. 10 (2008) 775–787.

[35] C. Vakifahmetoglu, T. Semerci, G.D. Soraru, Closed porosity ceramics and glasses, J. Am. Ceram. Soc. 00 (2020) 1–29.

[36] C. Vakifahmetoglu, Zeolite decorated highly porous acicular calcium silicate ceramics, Ceram. Int. 40 (2014) 11925–11932.

[37] J.E. Shelby, Introduction to glass science and technology, Royal Society of Chemistry, 2005.

[38] M.B. Ostergaard, R.R. Petersen, J. König, M. Bockowski, Y. Yue, Foam glass obtained through high-pressure sintering, J. Am. Ceram. Soc. 101 (2018) 3917–3923.

[39] A.M.M. Santos, W.L. Vasconcelos, Properties of porous silica glasses prepared via sol–gel process, J. Non. Cryst. Solids. 273 (2000) 145–149.

[40] W. Huo, S. Yan, J. Wu, J. Liu, Y. Chen, Y. Qu, X. Tang, J. Yang, A novel fabrication method for glass foams with small pore size and controllable pore structure, J. Am. Ceram. Soc. 100 (2017) 5502–5511.

[41] C. Ohl, M. Kappa, V. Wilker, S. Bhattacharjee, F. Scheffler, M. Scheffler, Novel open-cellular glass foams for optical applications, J. Am. Ceram. Soc. 94 (2011) 436–441.

[42] Y. Hong, X. Chen, X. Jing, H. Fan, B. Guo, Z. Gu, X. Zhang, Preparation, bioactivity, and drug release of hierarchical nanoporous bioactive glass

ultrathin fibers, Adv. Mater. 22 (2010) 754–758.

[43]   W. Haller, Chromatography on glass of controlled pore size, Nature. 206 (1965) 693–696.

[44]   B. Biliński, A.L. Dawidowicz, Investigation of porous structure and surface properties of controlled porosity glasses, Colloids Surfaces A Physicochem. Eng. Asp. 118 (1996) 149–160.

[45]   D. Gaskell, Introduction to the Thermodynamics of Materials, Sixth Edition, CRC Press, 2017.

[46]   S.S. Moosavi, P. Alizadeh, Effect of acid leaching time on pore diameter and volume of porous hollow glass microspheres, Mater. Lett. 167 (2016) 98–101.

[47]   V.A. Kreisberg, V.P. Rakcheev, T. V Antropova, Influence of the acid concentration on the morphology of micropores and mesopores in porous glasses, Glas. Phys. Chem. 32 (2006) 615–622.

[48]   Z. Zhou, M.-C. Wang, J. Han, F. Xu, X. Zhao, Effect of heat treatment on $7Na_2O–23B_2O_3–70SiO_2$ glass, Ceram. Int. 37 (2011) 1769–1773.

[49]   M. Kukizaki, T. Nakashima, Acid leaching process in the preparation of porous glass membranes from phase-separated glass in the Na_2O-CaO-MgO-Al_2O_3-B_2O_3-SiO_2 system, Membrane. 29 (2004) 301–308.

[50]   M. Hasanuzzaman, A. Rafferty, A.G. Olabi, Effects of zircon on porous structure and alkali durability of borosilicate glasses, Ceram. Int. 40 (2014) 581–590.

[51]   T. Yazawa, K. Kuraoka, W.-F. Du, Effect of cooling rate on pore distribution in quenched sodium borosilicate glasses, J. Phys. Chem. B. 103 (1999) 9841–9845.

[52]   W.-F. Du, K. Kuraoka, T. Akai, T. Yazawa, Study of Al_2O_3 effect on structural change and phase separation in Na_2O-B_2O_3-SiO_2 glass by NMR, J. Mater. Sci. 35 (2000) 4865–4871.

[53]   T. Takamori, M. Tomozawa, HCl leaching rate and microstructure of phase

separated borosilicate glasses, J. Am. Ceram. Soc. 61 (1978) 509–512.

[54] M. Shimbo, Leach-Out process of phase separated sodium borosilicate glass, Yogyo-Kyokai-Shi. 80 (1972) 277–284.

[55] A. Ledieu, F. Devreux, P. Barboux, L. Sicard, O. Spalla, Leaching of borosilicate glasses. I. Experiments, J. Non. Cryst. Solids. 343 (2004) 3–12.

[56] T.A. Tsyganova, T. V. Antropova, O. V. Rakhimova, T.G. Kostyreva, Specific features of the formation of a porous structure in products of leaching of two-phase sodium borosilicate glasses in acid-salt solutions, Glas. Phys. Chem. 33 (2007) 122–129.

[57] T. V. Antropova, Kinetics of corrosion of the alkali borosilicate glasses in acid solutions, J. Non. Cryst. Solids. 345–346 (2004) 270–275.

[58] V.A. Kreisberg, T. V Antropova, Changing the relation between micro-and mesoporosity in porous glasses: The effect of different factors, Microporous Mesoporous Mater. 190 (2014) 128–138.

[59] H. Tanaka, T. Yazawa, K. Eguchi, H. Nagasawa, N. Matsuda, T. Einishi, Precipitation of colloidal silica and pore size distribution in high silica porous glass, J. Non. Cryst. Solids. 65 (1984) 301–309.

[60] H. Kawamura, N. Takusagawa, S. Taruta, K. Kitajima, Occurrence of bimodal pore structure and leaching process in the preparation of porous glass from fluorine containing sodium borosilicate glass, J. Ceram. Soc. Japan. 104 (1996) 179–184.

[61] G.W. Scherer, M.G. Drexhage, Stress in leached phase-separated glass, J. Am. Ceram. Soc. 68 (1985) 419–426.

[62] H.P. Hood, M.E. Nordberg, Method of treating borosilicate glasses, U.S. Patent No. 2,286,275, 1942.

[63] S. Morimoto, Porous glass: preparation and properties, Key Eng. Mater. 115 (1995) 147–158.

[64] J.K. Yamamoto, M.T. Lanagan, A.S. Bhalla, R.E. Newnham, L.E. Cross,

Dielectric properties of microporous glass in the microwave region, J. Am. Ceram. Soc. 72 (1989) 916–921.

[65] B. Reinhardt, D. Enke, G. Bienhaus, Hierarchically structured silica via combination of salt sintering process and phase separation, Opt. Appl. 42 (2012) 265–270.

[66] B. Reinhardt, J. Herwig, S. Rannabauer, M. Scheffler, D. Enke, Hierarchically structured glass monoliths based on polyurethane foams as template, J. Eur. Ceram. Soc. 34 (2014) 1465–1470.

[67] J. Kim, S. Lee, D. Shin, Preparation of a hybrid solid glass electrolyte using a nano-porous sodium borosilicate glass membrane for lithium batteries, J. Ceram. Process. Res. 8 (2007) 208.

[68] U. Schadeck, K. Kyrgyzbaev, T. Gerdes, M. Willert-Porada, R. Moos, Porous and non-porous micrometer-sized glass platelets as separators for lithium-ion batteries, J. Memb. Sci. 550 (2018) 518–525.

[69] A.S. Kuznetsova, A. V Volkova, L.E. Ermakova, T. V Antropova, Iron (III) ion adsorption on macroporous glass, Glas. Phys. Chem. 44 (2018) 41–46.

[70] C. Mazilu, E. Rotiu, L. Ionescu, D. Radu, A. Dinischiotu, Nanoporous glass in Na_2O-B_2O_3-SiO_2 oxidic system, for potential biomedical applications, J. Optoelectron. Adv. Mater. 9 (2007) 2036–2040.

[71] T. Tanaka, A. Guilleux, T. Ohyama, Y.Y. Maruo, T. Hayashi, A ppb-level NO_2 gas sensor using coloration reactions in porous glass, Sensors Actuators B Chem. 56 (1999) 247–253.

[72] T. Tanaka, T. Ohyama, Y.Y. Maruo, T. Hayashi, Coloration reactions between NO_2 and organic compounds in porous glass for cumulative gas sensor, Sensors Actuators B Chem. 47 (1998) 65–69.

[73] Y.Y. Maruo, Measurement of ambient ozone using newly developed porous glass sensor, Sensors Actuators B Chem. 126 (2007) 485–491.

[74] P.T. Sotomayor, I.M. Raimundo Jr, A.J.G. Zarbin, J.J.R. Rohwedder, G.O.

Neto, O.L. Alves, Construction and evaluation of an optical pH sensor based on polyaniline–porous Vycor glass nanocomposite, Sensors Actuators B Chem. 74 (2001) 157–162.

[75] M.P. Xavier, B. Vallejo, M.D. Marazuela, M.C. Moreno-Bondi, F. Baldini, A. Falai, Fiber optic monitoring of carbamate pesticides using porous glass with covalently bound chlorophenol red, Biosens. Bioelectron. 14 (2000) 895–905.

[76] M.J. Dejneka, C. Powell, N. Borrelli, D. Ouzounov, A. Gaeta, Transparent magnetic glass-ceramics, J. Am. Ceram. Soc. 88 (2005) 2435–2441.

[77] S. Lee, T.W. Noh, J.R. Gaines, Y.-H. Ko, E.R. Kreidler, Optical studies of porous glass media containing silver particles, Phys. Rev. B. 37 (1988) 2918.

[78] V.G. Arakcheev, A.N. Bekin, Y. V Vladimirova, N. V Minaev, V.B. Morozov, A.O. Rybaltovskii, Synthesis and characterization of silver nanoparticles in a nanoporous glass, Moscow Univ. Phys. Bull. 69 (2014) 330–335.

[79] I.O. Mazali, A.G.S. Filho, B.C. Viana, J.M. Filho, O.L. Alves, Size-controllable synthesis of nanosized-TiO_2 anatase using porous Vycor glass as template, J. Nanoparticle Res. 8 (2006) 141–148.

[80] M. Anpo, N. Aikawa, Y. Kubokawa, M. Che, C. Louis, E. Giamello, Photoluminescence and photocatalytic activity of highly dispersed titanium oxide anchored onto porous Vycor glass, J. Phys. Chem. 89 (1985) 5017–5021.

[81] T. Yazawa, F. Machida, N. Kubo, T. Jin, Photocatalytic activity of transparent porous glass supported TiO_2, Ceram. Int. 35 (2009) 3321–3325.

[82] ASTM, Standard test method for water absorption, bulk density, apparent porosity and apparent specific gravity of fired whiteware products", C373-88. (2006).

[83] R. López, R. Gómez, Band-gap energy estimation from diffuse reflectance

measurements on sol–gel and commercial TiO_2: a comparative study, J. Sol-Gel Sci. Technol. 61 (2012) 1–7.

[84]   C. Carteret, A. Burneau, Effect of heat treatment on boron impurity in Vycor. Part II. Migration, reactivity with vapour water and dissolution in liquid water, Phys. Chem. Chem. Phys. 2 (2000) 1757–1762.

[85]   T.H. Elmer, I.D. Chapman, M.E. Nordberg, Changes in length and infrared transmittance during thermal dehydration of porous glass at temperatures up to 1200°, J. Phys. Chem. 66 (1962) 1517–1519.

[86]   M.J.D. Low, N. Ramasubramanian, Infrared study of the nature of the hydroxyl groups on the surface of porous glass, J. Phys. Chem. 70 (1966) 2740–2746.

[87]   R. Müller, E.D. Zanotto, V.M. Fokin, Surface crystallization of silicate glasses: nucleation sites and kinetics, J. Non. Cryst. Solids. 274 (2000) 208–231.

[88]   M.M. Lima, R. Monteiro, Characterisation and thermal behaviour of a borosilicate glass, Thermochim. Acta. 373 (2001) 69–74.

[89]   M. Hasanuzzaman, M. Sajjia, A. Rafferty, A.-G. Olabi, Thermal behaviour of zircon/zirconia-added chemically durable borosilicate porous glass, Thermochim. Acta. 555 (2013) 81–88.

[90]   S.H. Lee, K.I. Cho, J.B. Choi, D.W. Shin, Phase separation and electrical conductivity of lithium borosilicate glasses for potential thin film solid electrolytes, J. Power Sources. 162 (2006) 1341–1345.

[91]   M. Thommes, K. Kaneko, A. Neimark, J. Olivier, F. Rodriguez-Reinoso, J. Rouquerol, K.S. V Sing, Physisorption of gases, with special reference to the evaluation of surface area and pore size distribution (IUPAC Technical Report), 2015.

[92]   V.A. Kreisberg, V.P. Rakcheev, T. V Antropova, Microporosity of porous glasses: New investigation techniques, Glas. Phys. Chem. 29 (2003) 541–547.

[93] M. V Lyubavin, T.M. Burkat, V.N. Pak, Fabrication of silica membranes with controlled pore structure, Inorg. Mater. 44 (2008) 203–206.

[94] G.W. Scherer, Dilatation of porous glass, J. Am. Ceram. Soc. 69 (1986) 473–480.

[95] M. Nolan, T.S. Perova, R.A. Moore, C.E. Beitia, J.F. McGilp, H.S. Gamble, Spectroscopic investigations of borosilicate glass and its application as a dopant source for shallow junctions, J. Electrochem. Soc. 147 (2000) 3100–3105.

[96] H. Darwish, M.M. Gomaa, Effect of compositional changes on the structure and properties of alkali-alumino borosilicate glasses, J. Mater. Sci. Mater. Electron. 17 (2006) 35–42.

[97] Z. Hou, S. Wang, Z. Xue, H. Lu, C. Niu, H. Wang, B. Sun, C. Su, Crystallization and microstructural characterization of $B_2O_3 - Al_2O_3 - SiO_2$ glass, J. Non. Cryst. Solids. 356 (2010) 201–207.

[98] K. El-Egili, Infrared studies of $Na_2O - B_2O_3 - SiO_2$ and $Al_2O_3 - Na_2O - B_2O_3 - SiO_2$ glasses, Phys. B Condens. Matter. 325 (2003) 340–348.

[99] M.T. Kim, Deposition behavior of hexamethydisiloxane films based on the FTIR analysis of Si–O–Si and Si–CH$_3$ bonds, Thin Solid Films. 311 (1997) 157–163.

[100] M.A. Mazo, J. Sanguino, A. Tamayo, J. Rubio, Carbon nanofibers grown in-situ on porous glass, J. Nano Res. 50 (2017) 1–17.

[101] M. Parandamaiah, K.N. Kumar, S.V. Reddy, Spectroscopic properties of Eu^{+3} doped lithium sodium bismuth borate glasses for red luminescent optical devices, Int. J. Eng. Sci. 5 (2015) 16–22.

[102] C. Gautam, A.K. Yadav, A.K. Singh, A review on infrared spectroscopy of borate glasses with effects of different additives, ISRN Ceram. (2012) 1–17.

[103] L. Balachander, G. Ramadevudu, M. Shareefuddin, R. Sayanna, Y.C. Venudhar, IR analysis of borate glasses containing three alkali oxides,

ScienceAsia. 39 (2013) 278–283.

[104] X. Zhu, C. Mai, M. Li, Effects of B_2O_3 content variation on the Bi ions in Bi_2O_3 - B_2O_3 - SiO_2 glass structure, J. Non. Cryst. Solids. 388 (2014) 55–61.

[105] T. V Antropova, I.N. Anfimova, The influence of thermal treatment of the porous glass plates on the character of their scattering in visible spectral region, Opt. Appl. 40 (2010) 285–291.

[106] T. V Antropova, I.N. Anfimova, G.F. Golovina, Influence of the composition and temperature of heat treatment of porous glasses on their structure and light transmission in the visible spectral range, Glas. Phys. Chem. 35 (2009) 572–579.

[107] S. Ogawa, $1/\lambda^4$ scattering of light during the drying process in porous Vycor glass with nano-sized pores, JOSA A. 30 (2013) 154–159.

[108] T. V Antropova, I.A. Drozdova, Sintering of optical porous glasses, Opt. Appl. 33 (2003) 13–22.

[109] N.M. Emery, Method of making ultraviolet transmitting high silica glass, U.S. Patent number 2,505,001. 25, 1950.

[110] M.E. Nordberg, Ultraviolet-transmitting glasses for mercury-vapor lamps, J. Am. Ceram. Soc. 30 (1947) 174–179.

[111] M. Bertoldi, V.M. Sglavo, Soda–borosilicate glass: normal or anomalous behavior under Vickers indentation?, J. Non. Cryst. Solids. 344 (2004) 51–59.

[112] W. Lo, A.M. Campbell, J. Luo, R. Stevens, Indentation-induced deformation and microcracking of highly textured superconducting $(Bi,Pb)_2$ $Sr_2Ca_2Cu_3O_x$ ceramic, J. Mater. Res. 10 (1995) 568–577.

[113] K. Imakita, T. Kamada, J. Kamatani, M. Mizuhata, M. Fujii, Room temperature direct imprinting of porous glass prepared from phase-separated glass, Nanotechnology. 26 (2015) 255304.

[114] G.Q.M. Lu, G.Q.M. Lu, Z.M. Xiao, Mechanical properties of porous materials, J. Porous Mater. 6 (1999) 359–368.

[115] Z. Pawlak, W. Urbaniak, T. Kaldonski, A. Oloyede, Importance of bearing porosity in engineering and natural lubrication, in: Biomater. Med. Tribol., Elsevier, 2013: pp. 311–354.

[116] M. Wakuda, Y. Yamauchi, S. Kanzaki, Y. Yasuda, Effect of surface texturing on friction reduction between ceramic and steel materials under lubricated sliding contact, Wear. 254 (2003) 356–363.

[117] K. Hokkirigawa, T. Okabe, K. Saito, Friction properties of new porous carbon materials: woodceramics, J. Porous Mater. 2 (1996) 237–243.

[118] D.P. Mondal, S. Das, N. Jha, Dry sliding wear behaviour of aluminum syntactic foam, Mater. Des. 30 (2009) 2563–2568.

[119] G. Stachowiak, A.W. Batchelor, Engineering tribology, Butterworth-Heinemann, 2013.

[120] H. He, L. Qian, C.G. Pantano, S.H. Kim, Mechanochemical wear of soda lime silica glass in humid environments, J. Am. Ceram. Soc. 97 (2014) 2061–2068.

[121] E.B. Ertus, C. Vakifahmetoglu, A. Ozturk, Production and properties of phase separated porous glass, Ceram. Int. 46 (2020) 4947–4951.

[122] X. Song, B. Yang, M. Zhang, X. He, Study on the grain growth kinetics of TiO_2 nanocrystals synthesized by hydrothermal precipitation, Integr. Ferroelectr. 153 (2014) 140–150.

[123] M.A. Behnajady, H. Eskandarloo, N. Modirshahla, M. Shokri, Sol-gel low-temperature synthesis of stable anatase-type TiO_2 nanoparticles under different conditions and its photocatalytic activity, Photochem. Photobiol. 87 (2011) 1002–1008.

[124] H. Yamashita, M. Honda, M. Harada, Y. Ichihashi, M. Anpo, T. Hirao, N. Itoh, N. Iwamoto, Preparation of titanium oxide photocatalysts anchored on porous silica glass by a metal ion-implantation method and their photocatalytic reactivities for the degradation of 2-propanol diluted in water, J. Phys. Chem. B. 102 (1998) 10707–10711.

[125] H. Kawamura, S. Okuto, S. Taruta, N. Takusagawa, K. Kitajima, Inhomogeneous distribution of TiO_2 in porous glass specimen anchored by impregnation method using aqueous solutions, J. Ceram. Soc. Japan. 104 (1996) 1160–1162.

[126] J.-Y. Zhang, I.W. Boyd, B.J. O'sullivan, P.K. Hurley, P. V Kelly, J.-P. Senateur, Nanocrystalline TiO_2 films studied by optical, XRD and FTIR spectroscopy, J. Non. Cryst. Solids. 303 (2002) 134–138.

[127] A. Mirabedini, S.M. Mirabedini, A.A. Babalou, S. Pazokifard, Synthesis, characterization and enhanced photocatalytic activity of TiO_2/SiO_2 nanocomposite in an aqueous solution and acrylic-based coatings, Prog. Org. Coatings. 72 (2011) 453–460.

[128] S. Rasalingam, R. Peng, R.T. Koodali, Removal of hazardous pollutants from wastewaters: applications of TiO_2-SiO_2 mixed oxide materials, J. Nanomater. 2014 (2014) 1–41.

[129] R. Poliah, S. Sreekantan, Characterization and photocatalytic activity of enhanced copper-silica-loaded titania prepared via hydrothermal method, J. Nanomater. (2011) 1–8.

[130] S.-M. Chiu, Z.-S. Chen, K.-Y. Yang, Y.-L. Hsu, D. Gan, Photocatalytic activity of doped TiO_2 coatings prepared by sputtering deposition, J. Mater. Process. Technol. 192 (2007) 60–67.

[131] J. Yu, X. Zhao, Q. Zhao, G. Wang, Preparation and characterization of super-hydrophilic porous TiO_2 coating films, Mater. Chem. Phys. 68 (2001) 253–259.

[132] P. Praveen, G. Viruthagiri, S. Mugundan, N. Shanmugam, Structural, optical and morphological analyses of pristine titanium di-oxide nanoparticles – Synthesized via sol–gel route, Spectrochim. Acta Part A Mol. Biomol. Spectrosc. 117 (2014) 622–629.

[133] J. Tauc, R. Grigorovici, A. Vancu, Optical properties and electronic structure

of amorphous germanium, Phys. Status Solidi. 15 (1966) 627–637.

[134] T. Guang-Lei, H. Hong-Bo, S. Jian-Da, Effect of microstructure of TiO_2 thin films on optical band gap energy, Chinese Phys. Lett. 22 (2005) 1787–1789.

[135] C. He, Y. Yu, X. Hu, A. Larbot, Influence of silver doping on the photocatalytic activity of titania films, Appl. Surf. Sci. 200 (2002) 239–247.

[136] K. Kočí, L. Obalová, L. Matějová, D. Plachá, Z. Lacný, J. Jirkovský, O. Šolcová, Effect of TiO_2 particle size on the photocatalytic reduction of CO_2, Appl. Catal. B Environ. 89 (2009) 494–502.

[137] Z. Zhang, C.C. Wang, R. Zakaria, J.Y. Ying, Role of particle size in nanocrystalline TiO_2 based photocatalysts, J. Phys. Chem. B. 102 (1998) 10871–10878.

[138] V. Štengl, V. Houšková, S. Bakardjieva, N. Murafa, Photocatalytic activity of boron-modified titania under UV and visible-light illumination, ACS Appl. Mater. Interfaces. 2 (2010) 575–580.

[139] M.R. Hoffmann, S.T. Martin, W. Choi, D.W. Bahnemann, Environmental applications of semiconductor photocatalysis, Chem. Rev. 95 (1995) 69–96.

[140] J. Wang, R.H. Li, Z.H. Zhang, W. Sun, X.F. Wang, Z.Q. Xing, R. Xu, X.D. Zhang, Heat treatment of nanometer anatase powder and its photocatalytic activity for degradation of acid red B dye under visible light irradiation, Inorg. Mater. 44 (2008) 608–614.

[141] B. Choudhury, A. Choudhury, Oxygen defect dependent variation of band gap, Urbach energy and luminescence property of anatase, anatase–rutile mixed phase and of rutile phases of TiO_2 nanoparticles, Phys. E Low-Dimensional Syst. Nanostructures. 56 (2014) 364–371.

[142] J. Nowotny, T. Bak, M. Nowotny, L. Sheppard, Titanium dioxide for solar-hydrogen II. Defect chemistry, Int. J. Hydrogen Energy. 32 (2007) 2630–2643.

[143] D.A.H. Hanaor, C.C. Sorrell, Review of the anatase to rutile phase

transformation, J. Mater. Sci. 46 (2011) 855–874.

[144] L. Agartan, D. Kapusuz, J. Park, A. Ozturk, Effect of initial water content and calcination temperature on photocatalytic properties of TiO_2 nanopowders synthesized by the sol–gel process, Ceram. Int. 41 (2015) 12788–12797.

[145] C. Shen, Y.J. Wang, J.H. Xu, G.S. Luo, Facile synthesis and photocatalytic properties of TiO_2 nanoparticles supported on porous glass beads, Chem. Eng. J. 209 (2012) 478–485.

[146] C. Jiang, K.Y. Lee, C.M.A. Parlett, M.K. Bayazit, C.C. Lau, Q. Ruan, S.J.A. Moniz, A.F. Lee, J. Tang, Size-controlled TiO_2 nanoparticles on porous hosts for enhanced photocatalytic hydrogen production, Appl. Catal. A Gen. 521 (2016) 133–139.

[147] T. Mizutani, A. Mizutani, Adsorption of cationic biological materials on controlled pore glass, Anal. Biochem. 83 (1977) 216–221.

[148] J. Kárger, J. Lenzner, H. Pfeifer, H. Schwabe, W. Heyer, F. Janowski, F. Wolf, S.P. Ždanov, NMR study of adsorbate self-diffusion in porous glasses, J. Am. Ceram. Soc. 66 (1983) 69–72.

[149] W.D. Dozier, J.M. Drake, J. Klafter, Self-diffusion of a molecule in porous Vycor glass, Phys. Rev. Lett. 56 (1986) 197–202.

[150] F. Elwinger, P. Pourmand, I. Furó, Diffusive transport in pores: tortuosity and molecular interaction with the pore wall, J. Phys. Chem. C. 121 (2017) 13757–13764.

[151] L. Li, L. Chen, H. Shi, X. Chen, W. Lin, Evaluation of mesoporous bioactive glass (MBG) as adsorbent for removal of methylene blue (MB) from aqueous solution, J. Environ. Chem. Eng. 4 (2016) 1451–1459.

[152] N. Yuan, H. Cai, T. Liu, Q. Huang, X. Zhang, Adsorptive removal of methylene blue from aqueous solution using coal fly ash-derived mesoporous silica material, Adsorpt. Sci. Technol. 37 (2019) 333–348.

[153] S. Lei, J. Miyamoto, H. Kanoh, Y. Nakahigashi, K. Kaneko, Enhancement of

the methylene blue adsorption rate for ultramicroporous carbon fiber by addition of mesopores, Carbon N. Y. 44 (2006) 1884–1890.

[154] F. Tan, M. Liu, K. Li, Y. Wang, J. Wang, X. Guo, G. Zhang, C. Song, Facile synthesis of size-controlled MIL-100(Fe) with excellent adsorption capacity for methylene blue, Chem. Eng. J. 281 (2015) 360–367.

[155] M.J.D. Low, N. Ramasubramanian, The role of surface boron as adsorption center for the sorption of water by porous glass, J. Phys. Chem. 71 (1967) 3077–3081.

[156] M.L. Hair, W. Hertl, Reactivity of boria-silica surface hydroxyl groups, J. Phys. Chem. 77 (1973) 1965–1969.

[157] J. Aguado, R. Vangrieken, M. Lopezmunoz, J. Marugan, A comprehensive study of the synthesis, characterization and activity of TiO_2 and mixed TiO_2/SiO_2 photocatalysts, Appl. Catal. A Gen. 312 (2006) 202–212.

[158] X. Wang, F. Li, Y. Hao, S. Liu, M. Yang, TiO_2/SBA-15 composites prepared using H_2TiO_3 by hydrothermal method and its photocatalytic activity, Mater. Lett. 99 (2013) 38–41.

[159] T. Kamegawa, D. Yamahana, H. Yamashita, Graphene coating of TiO_2 nanoparticles loaded on mesoporous silica for enhancement of photocatalytic activity, J. Phys. Chem. C. 114 (2010) 15049–15053.

[160] Y.J. Acosta-Silva, R. Nava, V. Hernández-Morales, S.A. Macías-Sánchez, M.L. Gómez-Herrera, B. Pawelec, Methylene blue photodegradation over titania-decorated SBA-15, Appl. Catal. B Environ. 110 (2011) 108–117.

[161] N.B. Jackson, Attachment of TiO_2 powders to hollow glass microbeads: activity of the TiO_2 coated beads in the photoassisted oxidation of ethanol to acetaldehyde, J. Electrochem. Soc. 138 (1991) 3660–3664.

[162] G.S. Pozan, A. Kambur, Effect of operating parameters and titanium source on photodegradation of phenol, Indian J. Chem. Technol. 21 (2014) 272–279.

CURRICULUM VITAE

PERSONAL INFORMATION

Surname, Name: Ertuş, Emre Burak
Nationality: Turkish (TC)
Date and Place of Birth: 26 July 1988, Ankara
Marital Status: Married
Phone: +90 506 626 29 51
email: burak.ertus@metu.edu.tr

EDUCATION

Degree	Institution	Year of Graduation
MS	Dokuz Eylül Univ. Met. and Mat. Eng.	2014
BS	Dokuz Eylül Univ. Met. and Mat. Eng.	2012
High School	Karatay S.D.M.P. Anadolu Lisesi	2006

WORK EXPERIENCE

Year	Place	Enrollment
2013-Present	KTO Karatay Univ. Faculty of Eng., Materials Sci. and Nanotech. Eng. Konya.	Research Assistant
2012-2013	D.E.U Electronic Materials Production & Application Centre, İzmir	Project Assistant
07.2011	ROKETSAN, Ankara	Intern Eng. Student
07.2010	Koçak Metallurgy, Konya	Intern Eng. Student

LANGUAGES

Turkish, English

PUBLICATIONS

E.B. Ertus, C. Vakifahmetoglu, A. Ozturk, "Production and properties of phase separated porous glass." Ceramics International 46, 2020, 4947–4951.

E.B. Ertus, S.Yildirim, E. Celik, "Effect of La^{3+} and Ti^{4+} ions on the magnetic properties of barium hexaferrite powders synthesized using sol-gel method", Journal of Magnetics 21(4), 2016, 496-502.

Conferences

E.B. Ertus, C. Vakifahmetoglu, A. Ozturk, "Tribological properties of a porous sodium borosilicate glass" 19th International Metallurgy & Materials Congress (IMMC 2018), October, İstanbul/Turkey (Full Paper & Oral Presentation).

E.B. Ertus, C. Vakifahmetoglu, A. Ozturk, "Production of nanoporous glass fiber by selective leaching method" 18th International Metallurgy & Materials Congress (IMMC 2016), September, İstanbul/Turkey (Full Paper & Oral Presentation).

E.B. Ertus, S.Yildirim, E. Celik, "Sol-gel synthesis and magnetic properties of barium hexaferrite nanopowders" International Porous and Powder Materials (PPM 2013) Symposium & Exhibition, September, İzmir/Turkey (Oral Presentation & Abstract).

E.B. Ertus, E. Celik, "Sol-gel synthesis and characterization of $Sr_4Al_{12}O_{25}:Eu^{2+}Dy^{3+}$ Powders for Afterglow Painting Applications" International Porous and Powder Materials (PPM 2013) Symposium & Exhibition, September, İzmir/Turkey (Abstract).